Improved Battery State Estimation Using Novel Sensing Techniques

by

Nassim Abdul Samad

A dissertation submitted in partial fulfillment
of the requirements for the degree of
Doctor of Philosophy
(Mechanical Engineering)
in the University of Michigan
2016

Doctoral Committee:

Professor Anna G. Stefanopoulou, Chair
Professor Bogdan Epureanu
Assistant Research Scientist Jason B. Siegel
Professor Jing Sun

2016

To my loving family for their unconditional love and support

ACKNOWLEDGMENTS

First and foremost, I would like to thank my advisor Professor Anna G. Stefanopoulou for all the support and guidance throughout my graduate studies. It would have been an extremely arduous and exhausting journey had it not been for her motivation and patience. I would also like to thank her for believing in me and entrusting me in this demanding project. Immense gratitude and appreciation goes to Dr. Siegel for always being there to guide me through the most complex of problems. Dr. Siegel's critique polished my research skills and he was always ready to help whenever I needed guidance. His knowledge in the domain of battery behavior and controls is vast. I would like to thank my committee members, Prof. Bogdan Epureanu and Prof. Jing Sun for their critical feedback and insightful comments.

My work on this project has been a collaboration between the University of Michigan, Ford Motor Company and GE Global Research. I would thus like to extend my gratitude and thanks to Mr. Dyche Anderson from Ford Motor Company and Dr. Aaron Knobloch from GE Global Research. Their critical feedback and expert technical advice guided me through my research and helped me explore areas of research I had not tackled before. Also, as part of the collaboration on the Michigan team, I would like to acknowledge the contribution of Prof. Krishna Garikipati and Prof. Charles W. Monroe, and especially Dr. Ki-Yong Oh, for his collaborative work in the experimental and modeling field. My thanks also goes to the Advanced Research Projects Agency-Energy (ARPA-E) for providing me with the financial and technical support for this project.

It has been a pleasure working with all of my present and past colleagues in the Powertrain Controls Lab. Special thanks goes to Dr. Youngki Kim, Shankar Mohan, Dr. Boyun Wang and Dr. Xinfan Lin. We spent countless sleepless nights working on deadlines and tickling each others brains and exploring different ideas.

Thank you to all my friends in Ann Arbor for making this such a wonderful and fulfilling journey. I shall forever remember our time together here exploring what is to be offered away from the stress of graduate life.

Last but not least, I would like to dedicate this thesis to my loving family and especially my mom for her endless love, support and sacrifice. I couldn't imagine going through this journey without you.

TABLE OF CONTENTS

LIST OF FIGURES

LIST OF TABLES

LIST OF APPENDICES

ABSTRACT

Improved Battery State Estimation Using Novel Sensing Techniques

by

Nassim Abdul Samad

Chair: Anna G. Stefanopoulou

Lithium-ion batteries have been considered a great complement or substitute for gasoline engines due to their high energy and power density capabilities among other advantages. However, these types of energy storage devices are still yet not widespread, mainly because of their relatively high cost and safety issues, especially at elevated temperatures.

This thesis extends existing methods of estimating critical battery states using model-based techniques augmented by real-time measurements from novel temperature and force sensors. Typically, temperature sensors are located near the edge of the battery, and away from the hottest core cell regions, which leads to slower response times and increased errors in the prediction of core temperatures. New sensor technology allows for flexible sensor placement at the cell surface between cells in a pack. This raises questions about the optimal locations of these sensors for best observability and temperature estimation. Using a validated model, which is developed and verified using experiments in laboratory fixtures that replicate vehicle pack conditions, it is shown that optimal sensor placement can lead to better and faster temperature estimation.

Another equally important state is the state of health or the capacity fading of the cell. This thesis introduces a novel method of using force measurements for capacity fade estimation. Monitoring capacity is important for defining the range of electric vehicles (EVs) and plug-in hybrid electric vehicles (PHEVs). Current capacity estimation techniques re-

quire a full discharge to monitor capacity. The proposed method can complement or replace current methods because it only requires a shallow discharge, which is especially useful in EVs and PHEVs.

Using the accurate state estimation accomplished earlier, a method for downsizing a battery pack is shown to effectively reduce the number of cells in a pack without compromising safety. The influence on the battery performance (e.g. temperature, utilization, capacity fade, and cost) while downsizing and shifting the nominal operating SOC is demonstrated via simulations.

The contributions in this thesis aim to make EVs, HEVs and PHEVs less costly while maintaining safety and reliability as more people are transitioning towards more environmentally friendly means of transportation.

CHAPTER 1

Introduction

1.1 Background

1.1.1 Energy and the automotive industry

Fossil fuels have been the major source of energy in recent years. Although there is an increased consumption in renewables as shown in Fig. 1.1, coal, natural gas, and oil still constituted around 85% of the total world consumption in million tones oil equivalent in 2014 [1]. Despite the fact that burning fossil fuels for energy has been around for around two centuries, the energy debate nowadays ponders on whether this continuous fossil fuel burning should continue or whether we should be switching to more renewable energy sources.

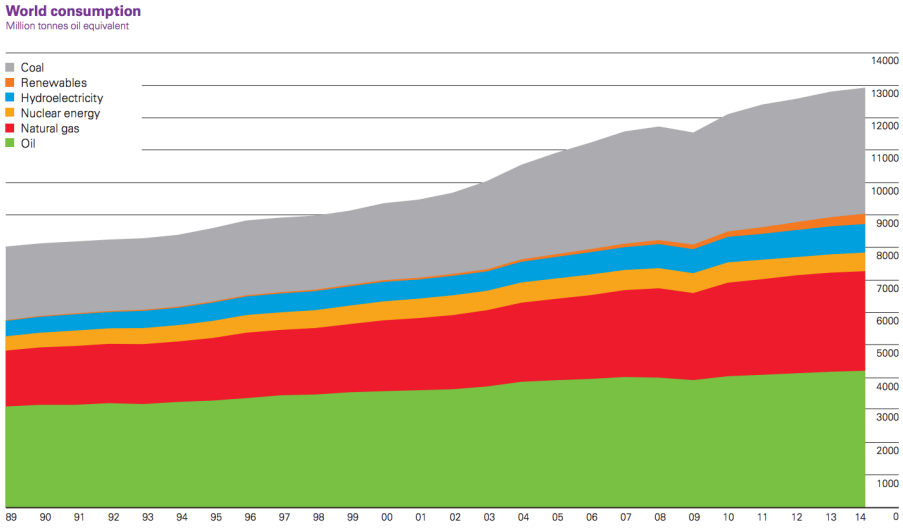

Figure 1.1: World primary energy consumption per different resources from year 1989 to 2014.

To begin with, coal, which is considered as the cheapest method for producing elec-

tricity, can result in the highest amount of CO_2 emissions as compared to oil and natural gas [2]. In 2012, China was by far the main consumer of coal at 47% of the total world consumption, with the United States coming in at second place with 11% of total world consumption [3]. On the other hand, the United States was the largest consumer of oil at 21% of the world consumption in 2013. Of that 21%, 45% is used for making motor gasoline [4]. The last of the fuels is natural gas, which is considered to be the cleanest of the three, is mainly used in heating applications.

The issue of burning fossil fuels then arises for two main reasons. First, burning fossil fuels leads to climate change and global warming. The global temperature variation since 400,000 years ago seems to correlate withe the levels of carbon dioxide in the atmosphere [5]. Figure 1.2 shows the a similar trend between the temperature and the CO_2 levels. Given the current dependance on fossil fuel burning, several labs have published projections on the average world temperature rise for the next 100 years. The projections show global temperature increase between 1.5 to 5.5°C [6]. Figure 1.3 shows what the earth looked like 18,000 years ago when the average temperatures were 5° lower than they are today [7], showing how impactful only 5° can be on global climate. This motivates the efforts to reduce the CO_2 emissions in the atmosphere by transitioning to more electric vehicles charged by renewable energy.

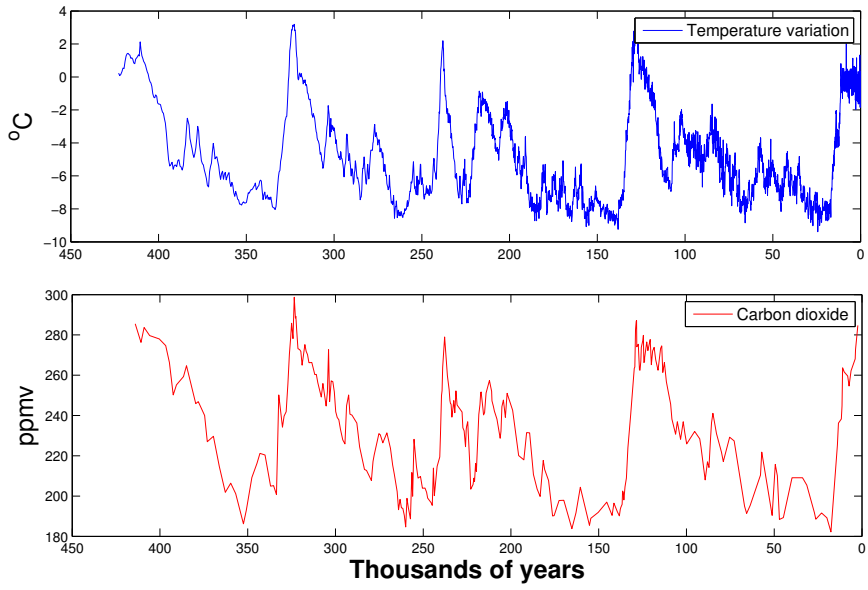

Figure 1.2: Global temperature variation with varying CO_2 levels from 400,000 years ago till the present day [5].

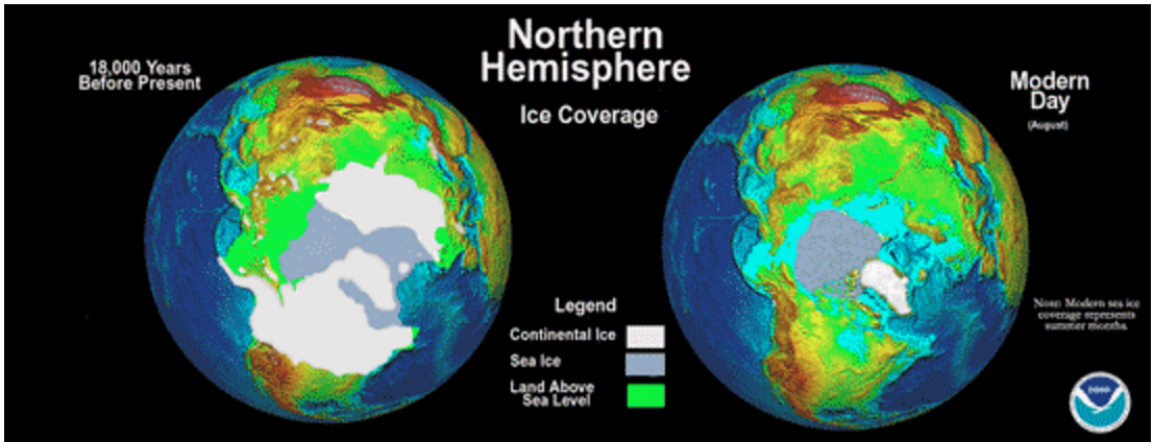

Figure 1.3: Northern hemisphere comparison 18,000 years ago versus today when global temperatures were 5° lower [7].

The other issue with fossil fuels is the fact that they are limited and that they will someday run out. The consensus seems to be that according to the current production rate, the world will run out of oil in the next 50 years [1]. As such, the search for more renewable sources of energy is needed to satisfy the energy demand of the world, especially in the field of transportation. In fact, in the U.S, transportation is one of the largest energy sectors [8] and it is almost all powered through petroleum as shown in Fig. 1.4. For this reason, significant effort and research has poured recently into the electrification of vehicles as manufacturers and researchers try to introduce more renewable or less polluting means of transportation.

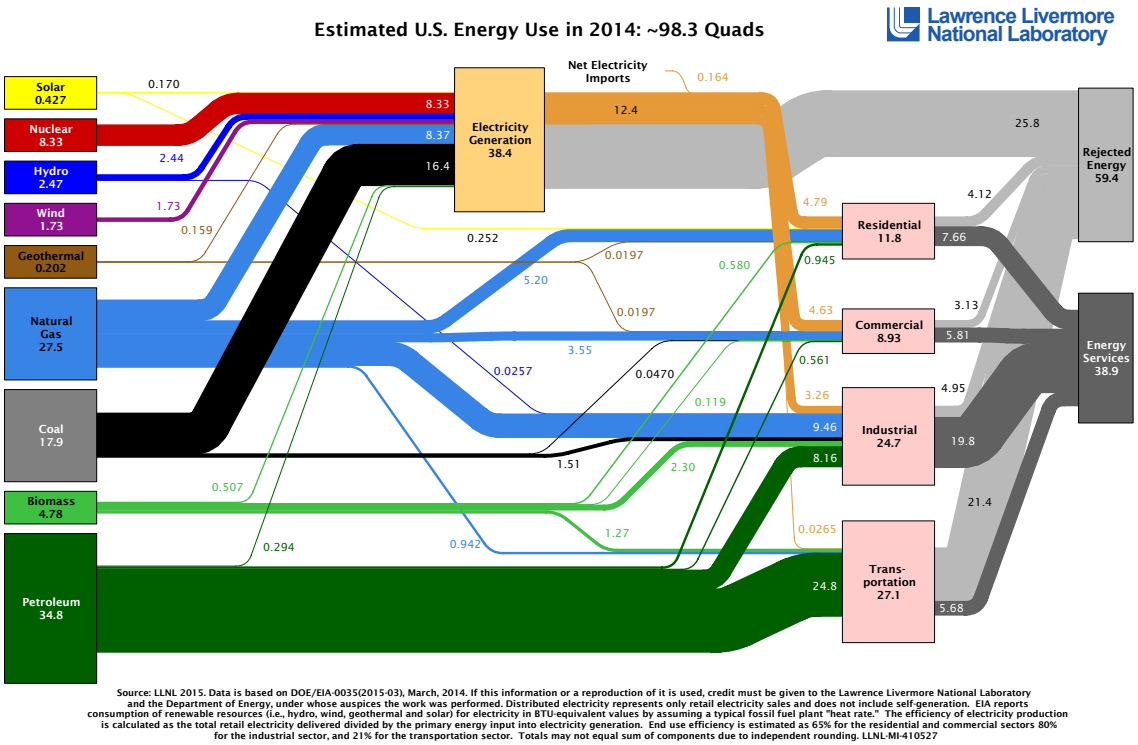

Figure 1.4: Estimated U.S. energy use in 2014 [8].

1.1.2 Electrification of vehicles

There are a couple of different types of electric vehicles in the market today. They are electric vehicles (EVs), plug-in hybrid electric vehicles (PHEVs), hydrogen vehicles and hybrid electric vehicles (HEVs). HEVs have a combustion engine and an electric motor that work together. As such, instead of relying entirely on the gas, and HEV can help reduce emissions and increase mileage by also using power from the battery, mainly during acceleration. This battery is charged either using the engine or using a process called regenerative breaking to recover the energy that is typically wasted in friction brakes. It cannot be charged externally. PHEVs, like the chevy volt, are better than HEVs in the sense that they use the battery until it depletes before the engine kicks in. This means, on a day to day basis with short trips, these types of vehicles rarely use the engine. Such cars are charged by plugging externally into a charging station. Fuel cell hydrogen and electric vehicles are totally electric and produce no CO_2 emissions.

Figure 1.5 shows the increase in the number of electric vehicles in the world in recent years. From 2015 to 2016 year alone, the increase was 73% [9]. With this increase, several different concerns arise for electric vehicle consumers, like performance, cost, range, safety

and cleanliness.

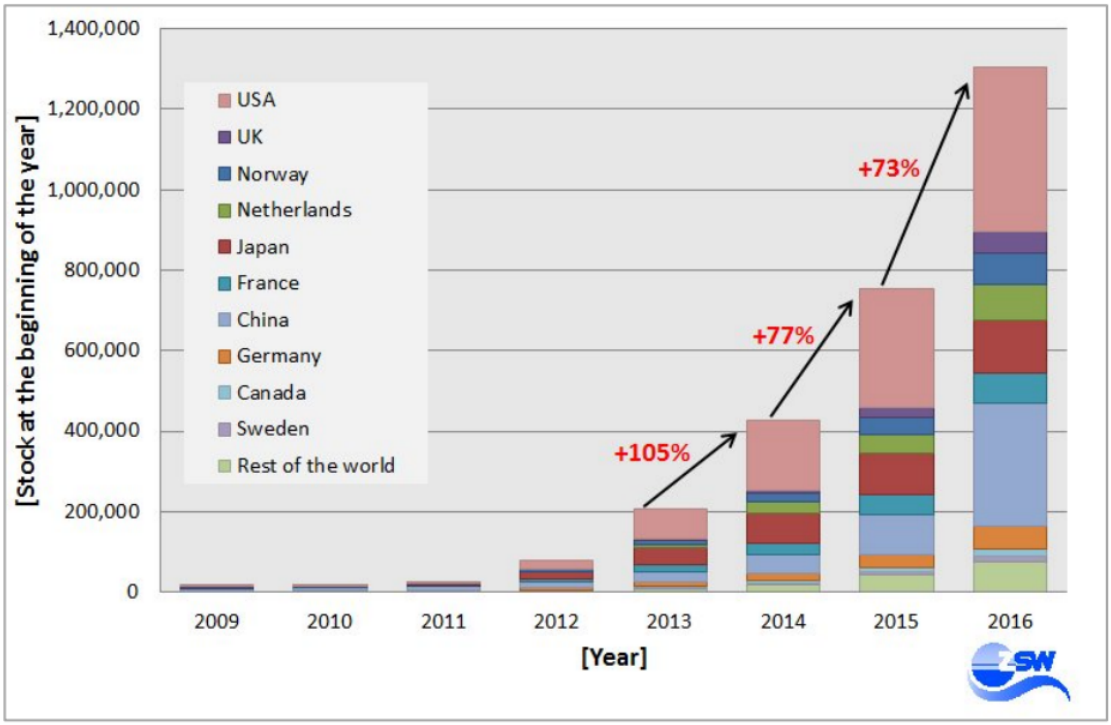

Figure 1.5: Stock of electric car vehicles across the world from 2009 to 2016 [9].

From an environmental stand point, electric vehicles charged at charging stations produce, on average, less emissions equivalent to gasoline cars [10]. Figure 1.6 shows that nearly half of all americans live in areas where charging an electric vehicle produces emissions equivalent to gasoline cars with miles per gallon rating of more than 50 mpg. Even in the worse case, charing an EV produces emissions equivalent to a gasoline vehicle with a 31-40 mpg rating.

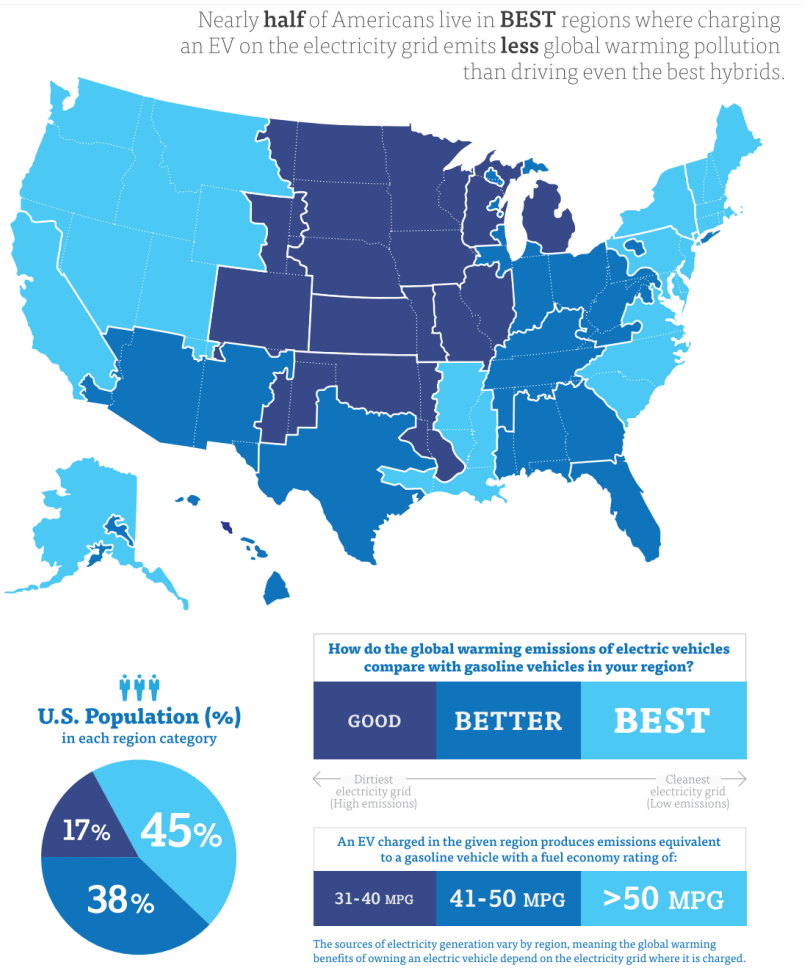

Figure 1.6: U.S. global emissions ratings for electric vehicles [10].

From a safety perspective, electric vehicles usually achieve higher safety ratings than gasoline engine cars. The Tesla Model S achieved the best safety rating given to any car ever [11]. However, there are still concerns about the safety and reliability of battery packs in an electric vehicle especially at elevated temperatures. When looking at cost, electric vehicles cost more than gasoline cars mainly because of the cost of the batteries. Although the projected price of Li-ion batteries is projected to decrease as shown in Fig. 1.7, more research is required in the field of Li-ion batteries to be able to reach the Department of Energy required target of $125 by year 2022.

Figure 1.7: Projected battery cost per KWh.

1.1.3 Lithium ion batteries

Lithium-ion batteries have been one of the most popular choices for powering electric vehicles (EVs) and hybrid electric vehicles (HEVs). Compared to other battery chemistries, lithium-ion batteries outperform their competitors because of their high energy and power densities, their ability to achieve long driving ranges and because they have no memory effects.

Lithium-ion batteries have three main components: a positive electrode (mainly made of a chemical compound like lithium iron phosphate ($LiFePO_4$)), a negative electrode (generally made from carbon) and an electrolyte. When the cell is being charged, the lithium ions move from the positive to the negative electrode through the electrolyte medium. As a result, the electrons flow in an external circuit since they cannot flow through the electrolyte as it is an insulating barrier [12]. Likewise, when the cell is being discharged, the ions and consequently the electrons flow in opposite directions. Figure 1.8 shows a schematic of the discharging process of a lithium-ion battery.

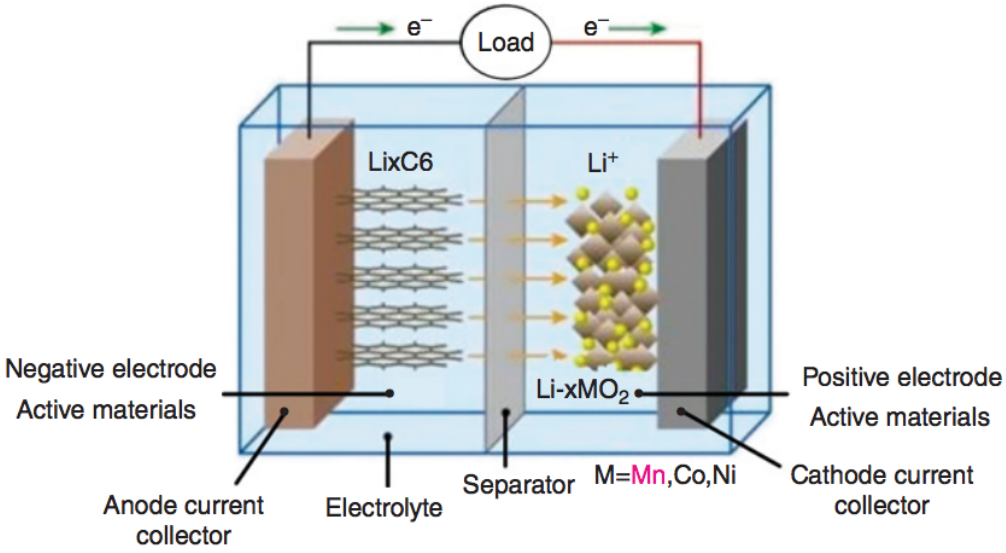

Figure 1.8: Schematic of the discharging process of a lithium-ion battery [13].

Since electric vehicles are powered by Li-ion cells, it is empirical that researchers exploit all possible means for improving the performance of Li-ion batteries while maintaining safety and decreasing costs.

1.2 Motivation

The proposed thesis is intended to look at possible methods to make electric battery packs more affordable. Specifically, this is done by investigating state estimation of temperature, state of charge (SOC) and state of health (SOH) in lithium-ion batteries. The accurate knowledge of these states can result in better power management strategies that allow for better and efficient utilization of the batteries. Also, this would present opportunities to scale down the size of batteries or packs and thus reducing cost. This is achieved because better state estimation results in more confidence in the operating limits of cells and the ability to push the cells to their limits.

Battery temperatures must be managed during high power operation due to internal heating of the cell. If the cell temperature rises above the breakdown temperature of the electrolyte or solid electrolyte interface, thermal runway could occur [14]. Better temperature state estimation is thus necessary. This could be achieved by using accurate mathematical models that are validated against a wide range of operating conditions and by

optimally placing sensors on the cell to give a faster and more accurate estimates of the core temperatures of a cell, which are usually the highest.

Also, although lithium-ion batteries have been one of the most popular choices for use a power sources in electric vehicles (EVs) and hybrid electric vehicles (HEVs), their performance still suffers from aging and degradation mechanisms [15, 16, 17] that hinders their efficient performance. In a vehicle, the battery management system (BMS) is responsible for many functions, mainly state estimation. Of the many important states that are affected by battery aging is the state of health (SOH). The SOH of a battery is usually quantified using either resistance growth [18, 19] or capacity fading [20, 21, 22]. Capacity fade estimation is important since it dictates the range of driving of EVs and PHEVs. Many methods are present that can predict and estimate capacity fade [23, 24]. However, much improvement could still be achieved by implementing techniques that allow for more frequent estimation of the capacity and the replacement or complementing of the current methods.

Finally, this improved state estimation can be implemented in current power management strategies to explore opportunities to downsize battery packs and thus reduce costs. Considering that most automotive companies employ lithium-ion batteries in their electric vehicles, and that lithium ion batteries are being widely used in energy storage devices [25] and consumer electronics [26], it is important that opportunities to downsize batteries or battery packs be seized such that they become affordable to all consumers.

1.3 Dissertation Organization

In Chapter 2, a distributed thermo-electric model is described. A validated model is necessary to accurately estimate and predict the core temperatures of the cells. The model couples a 3-D thermal network with a 2-D spatially distributed equivalent circuit electrical model. A method for parameterizing the model by coupling the parameterization with a high fidelity finite element model is introduced. A fixture is devised to replicate the same conditions experienced by the batteries in a vehicle pack. The model is then validated against spatially distributed measured temperature data using thin film sensors that allow for temperature validation on the surface of the cells. The validation is also performed against a wide range of operating conditions.

In Chapter 3, a method for finding the optimal sensor location for the estimation of the core temperatures of the battery cell is shown. The method looks at the eigenmode projections onto the observability subspace [27]. Results show the improved estimation of core temperature by placing the sensors on the optimally identified locations on the surface

of the cell versus placing the sensor near the tab of the cell where it is conventionally placed.

The distributed thermo-electric model identified in Chapter 2 is reduced to a two state model and expanded onto a pack level in Chapter 4. The optimal locations of a finite number of sensors in the pack is studied by analyzing the observability and observability gramian matrices. A power management strategy that takes into account the electrical and thermal constraints of the battery is applied at the pack level. The results are used to identify opportunities of scaling down the pack size and shifting the nominal operating SOC window without sacrificing capacity loss.

In Chapter 5, a novel method of using force in the incremental capacity analysis for estimating capacity fade is introduced. The method relies on using force measurements during battery operation to create the incremental capacity curves. The identified peaks in those curves can be utilized to estimate and predict battery capacity loss.

Finally, the thesis is concluded with ideas on future work. This includes using the force in an electro-thermal mechanical model that can be utilized to improve state of charge estimation [28, 29], and better estimate capacity loss [30].

1.4 Contributions

This work will present the following contributions:

- A method for coupling the parameterization of an electro-thermal model with a high fidelity finite element model [31, 32]. In a battery pack where complex geometries affect airflow, it is very hard to parameterize the flow parameters of an electro-thermal model. However, by coupling the parameterization with a finite element model, a method could be established to allow for an accurate parameterization of the electro-thermal model.

- Validation of an electro-thermal model against a wide range of operating conditions. With the emergence of new temperature sensor technologies, it is now possible to measure the surface temperature of cells while operating. This allows for temperature validation of distributed thermal models over the surface of the cell. For this purpose, a fixture is fabricated to replicate the same conditions experienced by the cells in a hybrid electric vehicle pack. Model validation is performed against different nominal SOCs, ambient temperatures, current amplitudes and pulse widths.

- A method for choosing the optimal sensor location on the surface of a cell [33]. Conventional temperature sensors are placed near the tabs of the cells in a battery pack

given the physical constraints. However, with the use of new thin film temperature sensors, the temperature at various surface locations can be measured. Thus a variation of the eigenmode projection method presented by Lim et al. [27] is presented to allow for the best thermal estimation of the core nodes of a jelly roll inside the battery. Results show that placing a sensor on the surface of the cell outperforms placing one near the tab (as is done conventionally). Also the best sensor location for estimating the core temperatures of the cell is shown to be at the hot spot on the surface of the cell, and is independent of the current magnitude.

- A power management strategy that takes into account the electrical and thermal constraints of a battery is applied at a pack level. The application of the methodology on a particular pack shows that pack size can be decreased by more than 15% while shifting the operating SOC window [34, 35]. This would result in minimal increase in capacity fade (less than 1%) over a simulated travel distance of 95000 miles.

- A novel method of using force measurements for estimating capacity fade is shown [30]. This method relies on the incremental capacity analysis. The method plots the differential of charge or discharge capacity over the differential of voltage (dQ/dV) with respect to voltage. The resulting plot shows a peak which will shift as the cell degrades. Instead of using voltage, the new method relies on the force measurements during the operation of a battery. For an NMC cell, the capacity fade estimation using the incremental capacity analysis using voltage occurs around the 40% of state of charge, while that using force measurements occurs around the 70% of state of charge. Consequently, the force-based estimation can be used more often in an electric vehicle (EV) or plug-in hybrid electric vehicle (PHEV). Also, this method can result in individual cell capacity estimates with an absolute mean and standard deviation on the error of 0.42% and 1.14% respectively between the measured and estimated capacities. The method is shown to be insensitive to the applied C-rate for small C-rates (less than C/3). Additional work is needed to establish the applicability of the method during charging.

CHAPTER 2

Dynamic electro-thermal model

2.1 Introduction

In a Li-ion battery cell, it is crucial to monitor and predict voltage, temperature and other important states, like the state of charge (SOC). Accurate prediction of those states is critical for developing battery management systems (BMS) that can utilize the full potential of a battery. Researchers have utilized different approaches to modeling the thermal and electrical behavior of Li-ion battery cells. Physics based models [36, 37, 38], which solve the governing equations of lithium-ion transport in the cell, can predict microscopic level behavior and performance, but require large computational power to solve the associated partial differential equations. Other models, which are more adequate for control oriented purposes, such as the battery management system (BMS) of a vehicle, employ electrical circuit elements [39, 40] to model the physical responses of the battery. These equivalent circuit models (ECMs) are relatively easy to parameterize and can yield sufficiently accurate results that justify their use in a BMS.

ECMs have been applied to cylindrical and prismatic cells. In cylindrical cells, ECM models that predict internal cell temperatures can be used to limit power [41] and control battery states such as SOC and regulate temperature by controlling the cooling system. Gao at al. [42] formulated a single RC equivalent circuit model with temperature and state of discharge (SOD) dependent open circuit voltage (OCV), coupled with a ”bulk” thermal model that characterizes the whole battery as one uniform temperature. In [39] and [43], Perez et al. and Lin et al. respectively worked on parameterizing a two state thermal model (surface and core) coupled with a double RC equivalent circuit model with temperature and state of charge dependent parameters. Smith et al. [44] used finite volume methods to model the temperature distributions along with a representative equivalent circuit model.

Prismatic cells can be physically packaged more efficiently than cylindrical cells. However, their electro-thermal-mechanical response is influenced by their packaging (hard-encased or pouch) and their dimensions. Many techniques were proposed in literature

for modeling the thermal behavior of prismatic cells [45, 46, 47]. Wang at al. [48] considered different thermal models and studied the computational efficiency and accuracy of these models. Inui et al. [49] considered the effect of the cross-sectional area of a prismatic battery on the temperature distributions within that battery. Gualous et al. [50] developed a new thermal parameter estimation tool using a first order Cauer thermal model, and investigated the behavior of a battery under abuse conditions. Other more recent models have presented coupled electro-thermal models that can predict temperature distributions in a prismatic cell [40, 45, 51]. In particular, coupled electro-thermal models with distributed equivalent circuits [40, 45] have been able to simulate the local dynamics of prismatic cells and observe the local variations in temperature.

The following chapter will present a coupled electro-thermal model capable of predicting the spatial temperature variation on the surface of the cell. The model is validated in a fixture with a novel set of sensors over a wide range of temperatures, SOCs and C-rates. The fixture is meant to replicate the pack conditions in a hybrid electric vehicle battery pack. The results show good agreement with experimental data.

2.2 Coupled electro-thermal model

The model presented here couples a $((m+3) \times (n+4) \times 5)$ state 3-D thermal model with an $(m \times n)$ 2D distributed equivalent circuit electrical model. Variables m and n can be modified and changed to increase the complexity and accuracy of the model. The thermal model has a 5 layered mesh, as shown in Fig. 2.1. For $k = 1$ or 5, each layer has airflow nodes. For $k = 2$ or 4, each layer has surface nodes that represent the aluminum casing of the cell. The middle layer ($k = 3$) has jelly roll nodes that lump the average properties of the roll, air gap nodes, and aluminum casing nodes (edge nodes). The 2D electrical model only represents the core nodes of the jelly roll. All $(m \times n)$ jelly roll core nodes are thus electrically and thermally connected. The electrical model generates output of terminal voltage, SOC and heat generation. The heat generation feeds into the thermal model to determine the temperature distributions which then feed back into the electrical model to determine the electrical properties which are functions of temperature.

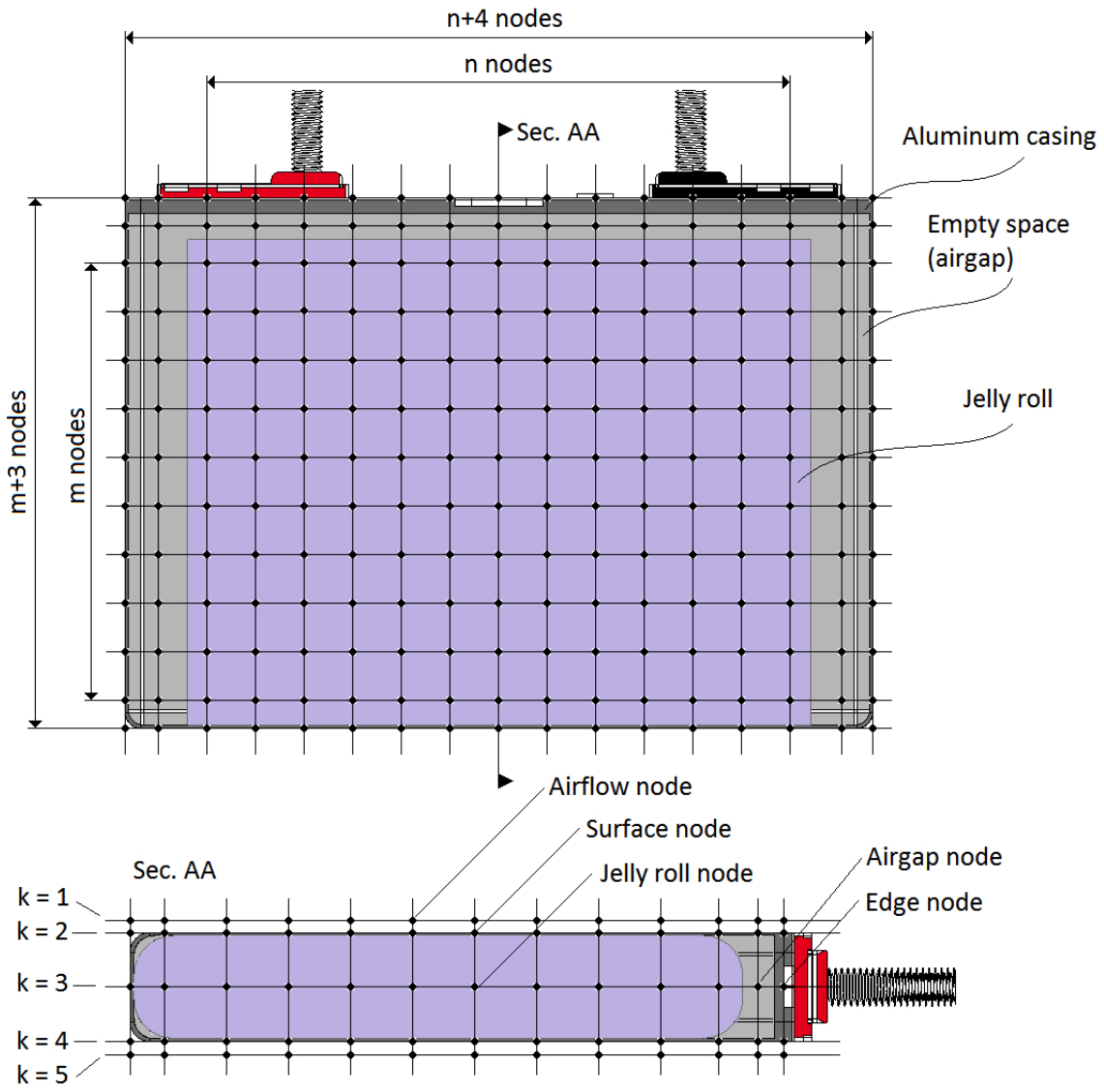

Figure 2.1: 5 layered mesh for thermal model

2.2.1 Experimental conditions

A fixture is designed to replicated battery pack conditions in a vehicle as shown in Fig. 2.2. The fixture consists of 3 Lithium Nickel-Manganese-Cobalt (NMC) Oxide battery cells clamped together between two Garolite end plates. Each battery cell is $120 \times 85 \times 12.7$ mm and has a nominal $Q_{nominal} = 5\ Ah$ capacity. A spacer is sandwiched between the batteries. The spacer has dimples which allow for airflow between the cells and maintains compression of the fixture (refer Fig. 2.2). The middle battery is instrumented with an array of RTD (resistance temperature detector) sensors on both sides. There are 36 RTDs

on each side of the battery. These thin film RTD sensors are mounted on the dimples of the spacer and measure the spatial surface temperature of the middle cell. The fixture is placed in an environmental chamber for ambient temperature control. The fixture has a fan connection to allow for flow control. This setup was designed to replicate the conditions in an actual vehicle, where the cells are stacked in an array. The novel thin RTD sensors allow for spatial surface temperature measurements while the cell is operating under flow and load conditions similar to that in the vehicle.

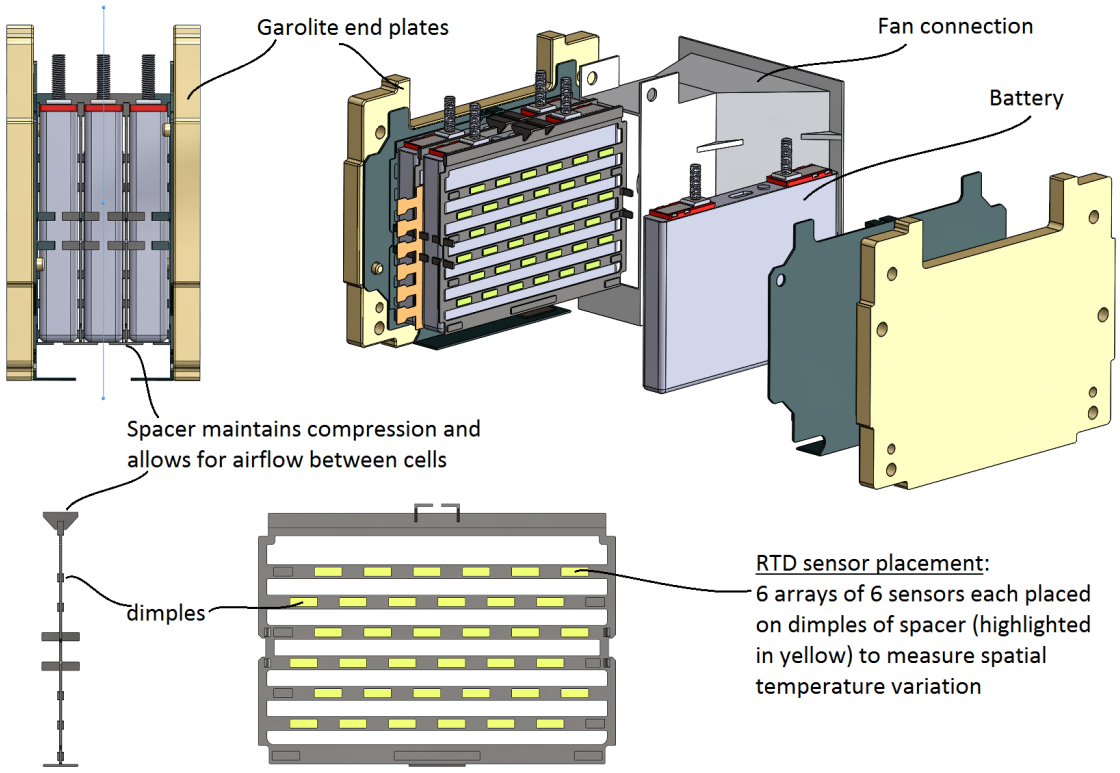

Figure 2.2: 3-cell fixture used in experiments showing placement of RTD sensors on spacer

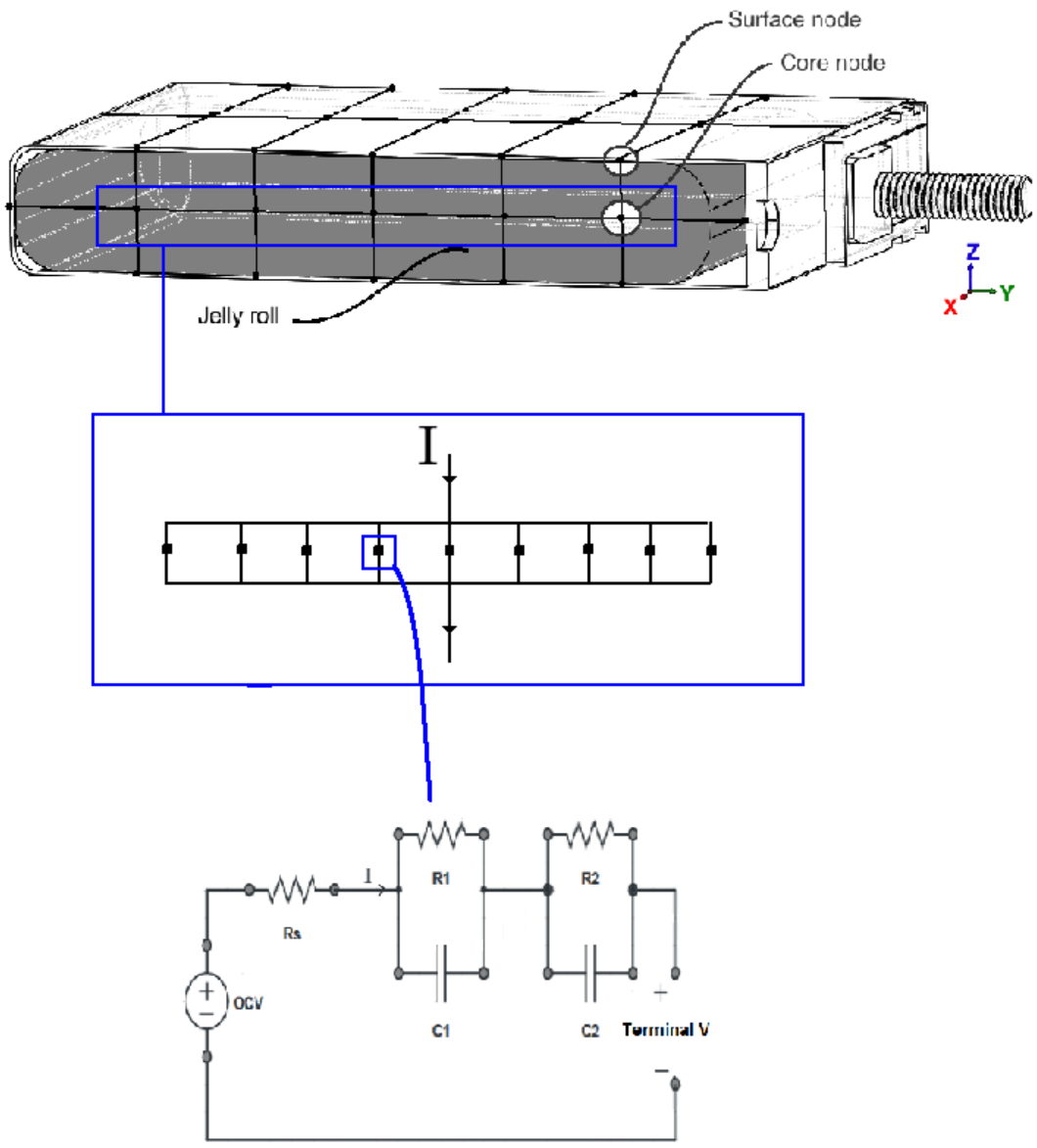

Figure 2.3: Double RC model representing an electrical node

2.2.2 Electrical model

In order to simulate the SOC and current variation at different spatial locations of the battery, a double RC model is implemented at each electrical node. Figure 2.3 shows a schematic of the equivalent circuit model at electrical node (i, j), where $2 \leq i \leq m + 1$ and $3 \leq j \leq n + 2$, and n and m is the number of discretizations along the length and width of the jelly roll. The series resistance $R_{s,ij}$ represents the internal resistance of the electrical node, which accounts for ohmic losses. The pairs $(R_{1,ij}, C_{1,ij})$ and $(R_{2,ij}, C_{2,ij})$

represent the resistances and capacitances that account for lithium diffusion in the solid and electrolyte. The OCV, which represents the open circuit voltage of the cell with no applied current, is a function of state of charge. Since the model assumes that the current collectors are infinitely conductive, this means that all electrical nodes are connected in parallel. The model at this stage does not account for tabbing. At each $(m \times n)$ 2-D spatial electrical node, a double RC equivalent circuit model is used to determine the local through-plane current density.

$$\sum_{\substack{2\leq i\leq m+1 \\ 3\leq j\leq n+2}} I_{ij} = I \tag{2.1}$$

where I is the total current into the battery. At each electrical node, Kirchhoff's voltage law applies so that at node (i, j), we have:

$$OCV_{ij} - I_{ij}R_{s,ij} - V_{1,ij} - V_{2,ij} = V_t \tag{2.2}$$

So for an input I, since $V_{1,ij}, V_{2,ij}$, and OCV_{ij} are states in this model, we can solve the following equation to get the local distributions of I_{ij}:

$$\begin{bmatrix} 1 & 1 & ... & 1 & 0 \\ R_{s,11} & 0 & ... & 0 & 1 \\ 0 & R_{s,21} & ... & 0 & 1 \\ \vdots & \vdots & \vdots & \vdots & \vdots \\ 0 & 0 & ... & R_{s,mn} & 1 \end{bmatrix} \begin{bmatrix} I_{11} \\ I_{21} \\ I_{31} \\ \vdots \\ V_t \end{bmatrix} = \begin{bmatrix} I \\ OCV_{11} - V_{1,11} - V_{2,11} \\ OCV_{21} - V_{1,21} - V_{2,21} \\ \vdots \\ OCV_{mn} - V_{1,mn} - V_{2,mn} \end{bmatrix} \tag{2.3}$$

The state equations representing an electrical node (i, j) are:

$$\begin{bmatrix} \dot{V}_{1,ij} \\ \dot{V}_{2,ij} \\ \dot{z}_{ij} \end{bmatrix} = \begin{bmatrix} -\frac{1}{R_{1,ij}C_{1,ij}} & 0 & 0 \\ 0 & -\frac{1}{R_{2,ij}C_{2,ij}} & 0 \\ 0 & 0 & 0 \end{bmatrix} \begin{bmatrix} V_{1,ij} \\ V_{2,ij} \\ z_{ij} \end{bmatrix} + \begin{bmatrix} \frac{1}{C_{1,ij}} \\ \frac{1}{C_{2,ij}} \\ -\frac{1}{Q_{ij}} \end{bmatrix} \begin{bmatrix} I_{ij} \end{bmatrix} \tag{2.4}$$

where $Q_{ij} = \frac{Q}{m \times n}$ is the nominal capacity of the cell node and z_{ij} is the state of charge of the cell node.

2.2.3 Thermal model

A 3-D thermal model is also implemented where a 5 layered-user defined mesh is introduced as shown in Fig. 2.1. The middle layer represents the thermal core nodes. The 2nd and 4th layers has surface nodes that represent the aluminum casing. The outer most

layers represent the airflow nodes. The thermal properties of aluminum are used for the surface nodes corresponding to the battery casing. The casing has a measured thickness of 0.6 mm. Air gaps exist between the jelly roll and the aluminum casing. These gaps are modeled using air thermal properties. This simplified model, where the a 2D mesh is used to lump the average properties of the jelly roll, is shown to be sufficiently accurate but much faster than a detailed model [48]. Heat generation occurs at the jelly roll core nodes, and surface convection occurs at the surface nodes. Conduction in the jelly roll is assumed to be anisotropic as the thermal conductivities across the x-y plane and z-axis are an order of magnitude different as reported in [47, 52]. Moreover, since the aluminum shell is relatively thin compared to the jell roll, the heat conduction from the core nodes to the surface nodes is dictated only by the thermal conductivity of the jelly roll in the z-axis.

The 3-dimensional heat transfer in each thermal node (i, j, k) in the cell is governed by the general heat equation (Eq. 2.5)

$$\rho c V \frac{dT_{ijk}}{dt} = \dot{Q}_{gn,ijk} + \Delta Q_{ijk}, \tag{2.5}$$

where $k = 1, ..., 5$, $i = 1, ..., m + 3$ and $j = 1, ..., n + 4$ are the coordinates of the thermal node according to the thermal mesh layout in Fig. 2.1. ρ is the density of the node volume, c is the specific heat capacity, and V the volume of that node. $\dot{Q}_{gn,ijk}$ represents the heat generation in the unit volume. Note that the heat generation only occurs in the electrical core nodes (for which $k = 3$). Accordingly, the heat generation $\dot{Q}_{gn,ijk}$ is:

$$\dot{Q}_{gn,ijk} = \begin{cases} I_{ij}^2 R_{s,ij} + \frac{V_{1,ij}^2}{R_{1,ij}} + \frac{V_{2,ij}^2}{R_{2,ij}} + I_{ij} T_{ij} \frac{dU}{dT}\Big|_{ij} & k = 3\ ,\ 2 \le i \le m+1\ ,\ 3 \le j \le n+2 \\ 0 & \text{otherwise} \end{cases} \tag{2.6}$$

where the first 3 terms of Eqn. 2.6 represents the ohmic heat generation, and the last term represents the entropic heat generation. ΔQ_{ijk} in Eq. 2.5 represents the net heat conduction and/or surface convection into the node volume, depending on the location of that thermal node. For a thermal core node (jelly roll, air gap or aluminum casing) where $k = 3$, the net heat flow is:

$$\Delta Q_{ijk} = \frac{K_x A_x}{L_x}(T_{(i-1)jk} + T_{(i+1)jk} - 2T_{ijk}) + \frac{K_y A_y}{L_y}(T_{i(j-1)k} + T_{i(j+1)k} - 2T_{ijk}) + \frac{K_z A_z}{L_z}(T_{ij(k-1)} + T_{ij(k+1)} - 2T_{ijk}). \tag{2.7}$$

In the jelly roll, thermal conductivity is anisotropic. It is the same in the $xy - plane$, so $K_x = K_y = K_{xy}$, and K_z is the thermal conductivity across the electrode planes. For the air gap nodes, thermal conductivity is the same ($K_x = K_y = K_z = K_{air}$). For an aluminum casing node, the net heat flow is that of Eq. 2.7 where one of the conduction terms is replaced by $h_{side}A_{side}(T_{air} - T_{ijk})$ depending on the location of the node.
For a surface node (i, j, k) where $k = 2$ or $k = 4$, the net heat flow is:

$$\Delta Q_{ijk} = \frac{K_x A_x}{L_x}(T_{(i-1)jk} + T_{(i+1)jk} - 2T_{ijk}) + \frac{K_y A_y}{L_y}(T_{i(j-1)k} + T_{i(j+1)k} - 2T_{ijk}) + \frac{K_z A_z}{L_z}(T_{ij(k+1)} - T_{ijk}) + h_{surf}A_{surf}(T_{ij(k-1)} - T_{ijk}). \quad (2.8)$$

Note that Eq. 2.8 above is for the case where $k = 2$. For $k = 4$, $k + 1$ and $k - 1$ are simply reversed due to the layout of the mesh. Finally the net heat transfer for an airflow node (i, j, k), where $k = 1$ or $k = 5$, is defined as:

$$\begin{aligned}\Delta Q_{ijk} &= h_{surf}A_{surf}(T_{ij(k+1)} - T_{ijk}) + \dot{m}_{in}h_{in} - \dot{m}_{out}h_{out} \\ &= h_{surf}A_{surf}(T_{ij(k+1)} - T_{ijk}) + (\rho c)_{air}A_{gap}v(T_{i(j-1)k} - T_{ijk}).\end{aligned} \quad (2.9)$$

Again, Eq. 2.9 above is for the case where $k = 1$. For $k = 5$, $k + 1$ and $k - 1$ are reversed. In Eqs. 2.7, 2.8, and 2.9, A_x, A_y and A_z are the corresponding areas between neighboring nodes in the x, y and z directions and they depend on the number of discretizations in the cell. Note that A_{surf}, A_{side} and A_{gap} are special cases of A_x, A_y or A_z for the cases where the node is on the surface, side or air respectively. L_x, L_y and L_z are the corresponding lengths between neighboring nodes in the x, y and z directions. T_{ijk} is the temperature of node (i, j, k), h_{surf} and h_{side} are the heat transfer coefficients along the surface and the sides of the cell respectively, and v is the mean velocity of air over the surface of the cell, which is not measured in the experiments. This velocity will be parameterized by coupling the cell electrothermal model with a finite element flow model which will be explained in Section 2.2.5.2. Note that radiative heat transfer could contribute up to 63% of the overall heat transfer out of the cell [48], but in this experiment, the cells are enclosed in a fixture as shown in Fig. 2.2, which limits the radiative heat transfer considerably. Thus h_{surf} would be representative of the heat transfer coefficient over the surface of the battery. Finally for those nodes that are on the sides (not the surface), another heat transfer coefficient h_{side} is considered since the conditions on the surface and the sides of the battery are different. Note that h_{surf} and h_{side} are a function of flow conditions, and are constant for a given flow condition. The thermal parameters to be identified for the thermal model would be:

- jelly roll parameters: K_{xy}, K_z and ρc
- airflow parameters: h_{surf}, h_{side} and v

2.2.4 Electrical model parameterization

The distributed model requires that electrical parameters be identified at each node of the jelly roll. To achieve this, one double RC model was assumed to represent the entire jelly roll. Electrical parameterization was done under controlled conditions at different temperatures and SOCs to characterize the resistances (R_s, R_1, R_2) and capacitances (C_1, C_2) of the double RC model. This model is then expanded into a distributed model by distributing the electrical resistances (R_s, R_1, R_2) in parallel (i.e. $\sum_{\substack{2\leq i\leq m+1\\3\leq j\leq n+2}} \frac{1}{R_{s,ij}} = \frac{1}{R_s}$) among the electrical core nodes. Accordingly, to maintain the time constant, the capacitances (C_1, C_2) are distributed in series (i.e. $\sum_{\substack{2\leq i\leq m+1\\3\leq j\leq n+2}} C_{1,ij} = C_1$). This agrees with the assumption in Section 2.2.2 that terminal voltage across all core nodes is the same and that the distributed double RC circuits are assumed to be in parallel. Also the capacity of each node is assumed to scale with the corresponding number of electrical nodes (i.e. $Q_{ij} = \frac{Q_{nominal}}{m\times n}$). The surface nodes are only represented by thermal nodes and are thus not accounted for in the distributed double RC model.

Figure 2.4 shows the current profile used for parameterization at each SOC step. The battery was charged to 100% SOC and allowed to relax, and then a series of pulses were performed at different SOCs. The pulses consisted of a (5A, -5A, 15A, -15A) pulses of 10 sec duration with 200 sec rest after the (5A, -5A) pulses and 300 sec rest after the (15A, -15A) pulses. This parameterization was done for $T \in \{45, 35, 25, 15, 5, -5\}$°C. A fine parameterization was done at higher and lower SOCs (SOC $\in \{0, 2.5, 5, 7.5, 10, 15, 20, 30, ..., 80, 85, 90, 92.5, 95, 97.5, 100\}$) since a bigger change in the electrical parameters is expected at those SOCs.

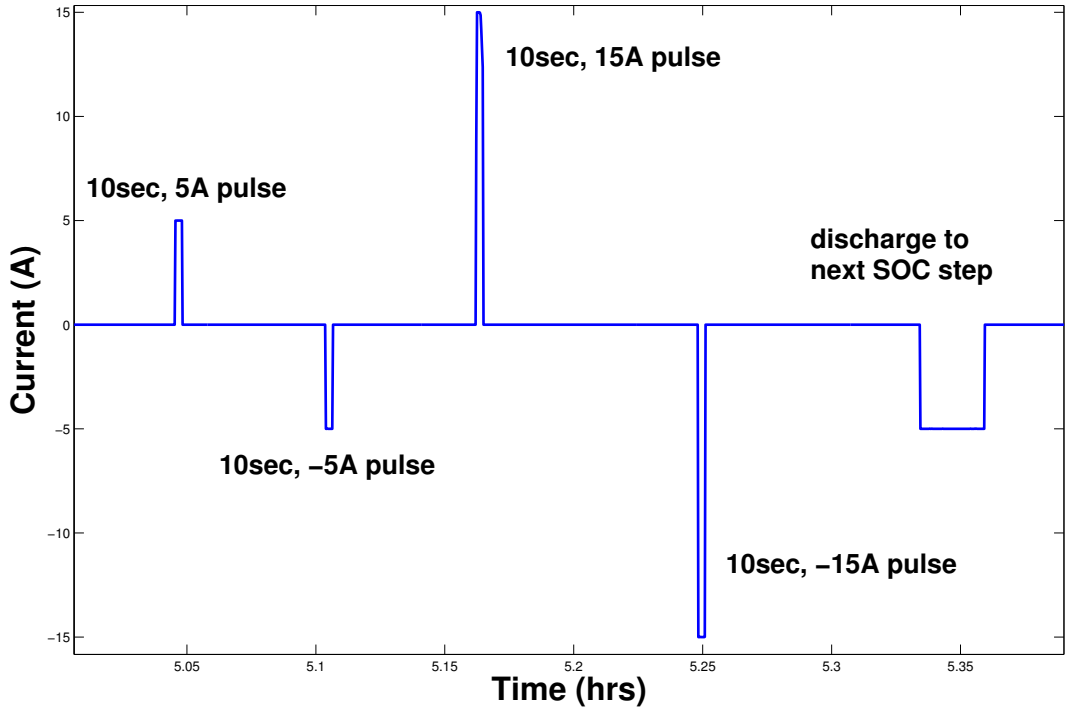

Figure 2.4: Current profile used for electrical parameterization

Figure 2.5 shows the voltage fit on the relaxation data after the 15A, 10 sec CC (constant current) discharge pulse, and the error on the fit for 3 models: single, double and triple RC models, at 3 different SOC (30%, 50%, and 70%). The double and triple RC models provide a better fit to the data than the single RC model. Although less accurate than a triple RC model, the parameters identified using a double RC model can easily span the wide ranges of SOC and temperature and yield small errors and root mean square errors (RMSE) on voltage estimation [43, 53]. The resulting electrical parameters are plotted in Fig. 2.6. As expected the electrical resistances decrease with increasing temperature and increase at lower SOCs. The behavior of R_s as a function of temperature seems to follow an Arrhenius relationship, where the resistance increases exponentially as a function of decreasing temperature.

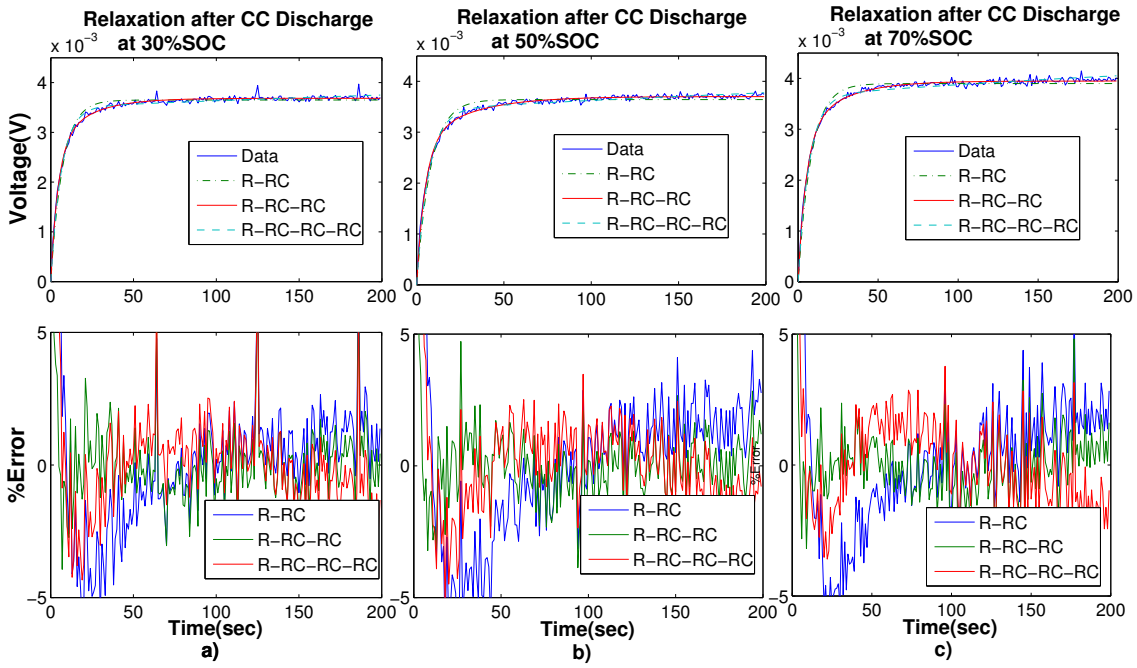

Figure 2.5: Voltage fit and error for single, double and triple RC models at a) 30% SOC b) 50% SOC c) 70% SOC at 25°C and using $15A$ current pulse

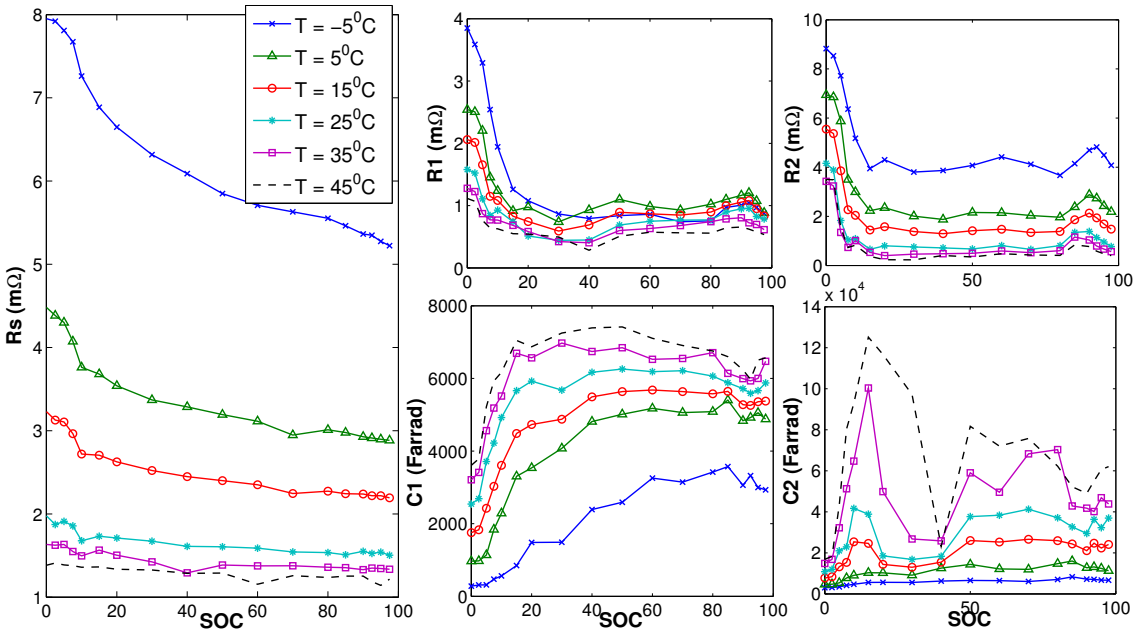

Figure 2.6: Electrical parameters R_s, R_1, C_1, R_2, and C_2 as a function of SOC and temperature

Figure 2.7 shows the time constants for the double RC pairs (R_1, C_1) and (R_2, C_2) at different temperatures. The electrical response of the battery has 2 time constants that are an order of magnitude different. The larger time constant also shows that the battery relaxes slower at lower and higher SOCs.

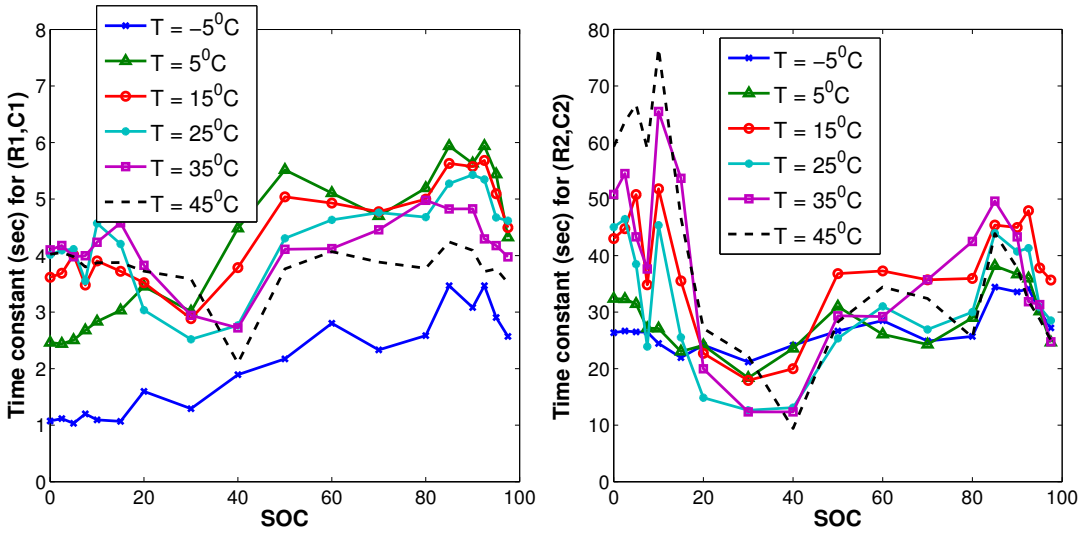

Figure 2.7: Time constant for both RC pairs at different temperatures

Finally, the entropic heat generation of the battery $\frac{dU}{dT}$ in Eq. 2.6 has to be parameterized. A voltage relaxation method was used [54]. The method consists of charging or discharging the battery to a certain SOC, letting it relax and then changing the temperature to measure the OCV change. The value of $\frac{dU}{dT}$ is the slope of the OCV as a function of temperature at that SOC, defined as:

$$\frac{dU}{dT} = \frac{U(T_2) - U(T_1)}{T_2 - T_1}, \tag{2.10}$$

where T is the temperature of the battery cell, and $U(T)$ is the value of the OCV at that temperature. Figure 2.8 shows the slope $\frac{dU}{dT}$ at different SOCs. In a lithium cobalt oxide cell, $\frac{dU}{dT}$ is a strong function of SOC and not temperature [49], so in this chapter, entropy change is also assumed to be a function of SOC only. Thus, this experiment was performed at 25^oC and the results are considered representative of the range of temperatures in our experiments. Depending on the sign of current and $\frac{dU}{dT}$, the value of $IT\frac{dU}{dT}$ could be positive or negative implying an exothermic or endothermic reaction respectively. This effect would be observable at low charge or discharge rates where the ohmic heat generation is small compared to the entropic heat generation. At values of SOC between 45% SOC and 80%

SOC, the entropy coefficient is positive, but it is negative beyond these points.

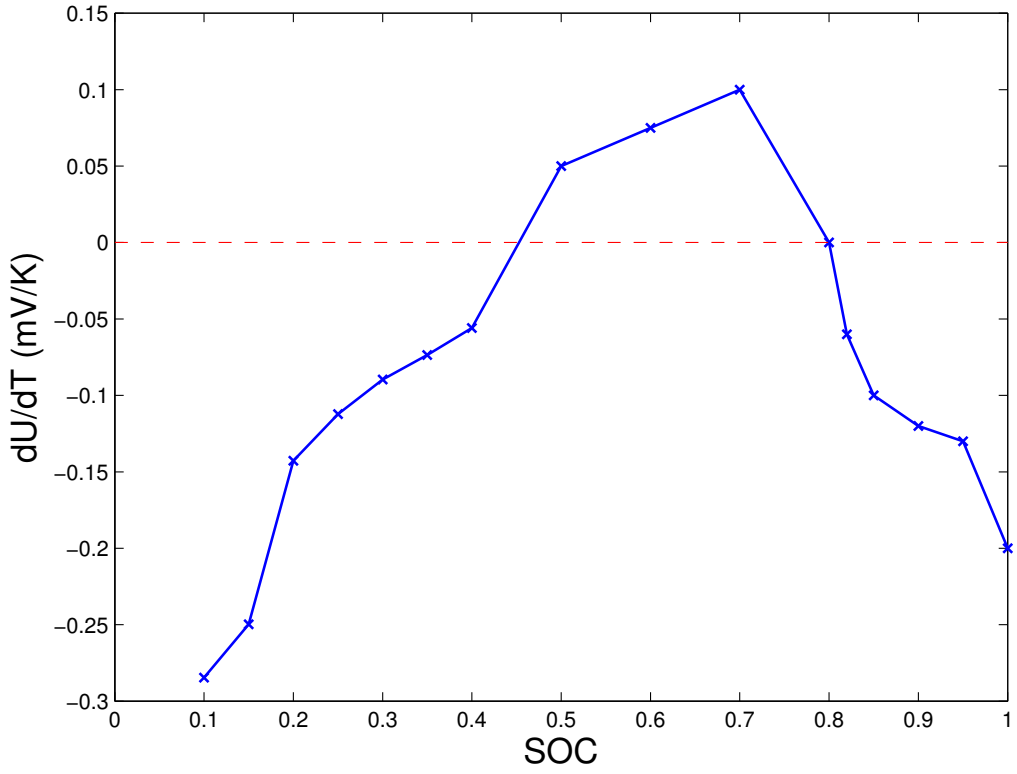

Figure 2.8: Entropy slope $\frac{dU}{dT}$ as a function of SOC as measured during discharge at 25^oC

The electrical parameters are applied at every jelly roll node in the cell. These parameters are a function of SOC and temperature. Since each node operates at a slightly different temperature, then each node will electrically operate at a slightly different SOC state.

2.2.5 Thermal model parameterization

As noted earlier in section 2.2.3, the thermal jelly roll and airflow parameters of the battery are unknown. Many papers have cited values for the thermal parameters [47, 45, 52], but in this case, since each core node in the jelly roll is considered a lumped node, the published values cannot be used and parameterization was done to quantify the values of these lumped parameters.

The thermal parameterization was performed in two steps:

- Step 1: An optimization fitting algorithm was applied to identify the unknown parameters under a simple natural convection scheme with no airflow. Since it is a natural

convection scheme, the velocity term, v, was dropped in Eq. 2.9. This allowed for the identification of parameters K_{xy}, K_z, h_{surf}, h_{side} and ρc. Note that parameters K_{xy}, K_z, h_{side} and ρc would remain the same regardless of the convection scheme since they are independent of the air flow. Only h_{surf} and the flow velocity, v, over the surface of the cell would change as the convection conditions change.

- Step 2: The objective of this step is to identify the mean air flow velocity, v, over the surface of the cell. A forced convection scheme was considered, where moving air was present to cool the battery. Air flow was produced by a cooling fan that was attached to the 3-cell fixture air outlet (refer Fig. 2.2). Parameters K_{xy}, K_z, h_{side} and ρc were assumed unchanged and were fed to a finite element model (FEM). The airflow parameter, v, was parameterized by using a training data set (39A pulsing under forced natural convection). This identified value of v was also validated using the FEM against 2 other experiments (20A and 50A under the same forced convection scheme). The resulting velocity, v, was then fed back into the equivalent circuit model, where the heat transfer coefficient, h_{surf}, was retuned under the same forced convection scheme used in the FEM (i.e. using the same velocity and pulsing profiles). The flow chart shown in Fig. 2.9 shows the process of cascading the parameterization between the FEM and the equivalent circuit model.

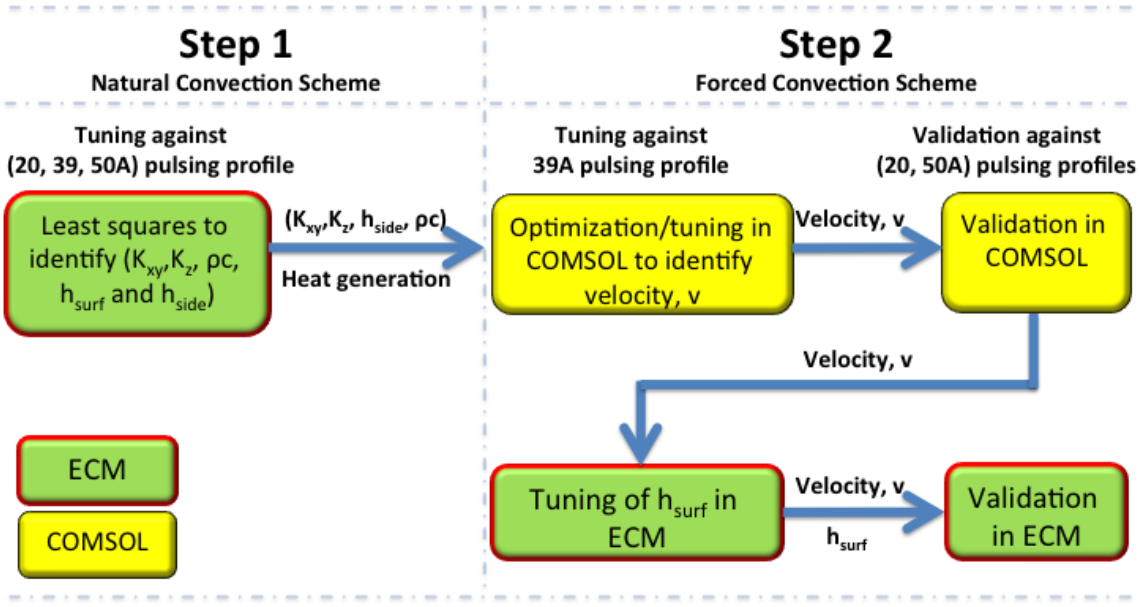

Figure 2.9: Flow chart showing the process of cascading parameterization in COMSOL

2.2.5.1 Step 1: Parameter fitting

Parameterization was done using least squares method [43]. Thermal equations 2.5 through 2.9 were solved using ODE solver in MATLAB, and the resulting simulated surface temperature distributions were interpolated into the 36 RTD sensor locations shown in Fig. 2.2. A least squares was performed on all $n = 1, ..., 36$ RTD sensors for the duration of the simulation, $t \in [0\ 120,000]$ sec, to find the best fit for the parameters. The objective function J to minimize is:

$$J = \sum_{n=1}^{36} \sqrt{\sum_{t=0}^{t_{end}} (\bar{T}_n(t) - T_n(t))^2} \tag{2.11}$$

where $\bar{T}_n(t)$ and $T_n(t)$ are the measured and simulated temperatures respectively at the sensor locations at time t.

Figure 2.10 shows the current profile used for parameterization and the corresponding measured temperatures on the surface of the battery. The experiment is performed under natural convection schemes where the fixture fan is turned off, and chamber fan is turned on to maintain ambient temperature. This meant that there was no airflow over the surface and the only parameters to parameterize were the thermal conductivities (K_{xy}, K_z), heat transfer coefficients (h_{surf} and h_{side}) and ρc. Parameters K_{xy}, K_z, ρc and h_{side} are constant regardless of the convection scheme. Parameter h_{surf} would have to be re-parameterized in step 2 along with the airflow velocity since it depends on the convection scheme. To allow for sufficient excitation, a 20A, 39A and 50A current amplitudes were used with a pulse width of 20 sec each at 50%SOC. Each excitation was 4 hours long to allow for thermal equilibrium.

The values of the parameters that resulted from the thermal parameterization under a natural convection scheme are shown in Table 2.1 (in bold) along with the thermal parameters of aluminum and air.

Note that $h_{surf} = 6\ W/mK$ and $h_{side} = 18\ W/mK$ are the convection coefficients from the aluminum casing to the ambient when the fan is turned off (natural convection). The sides of the battery are exposed to the chamber fan which circulates air and maintains the ambient at some specified temperature resulting in higher h_{side} than h_{surf}, while the surfaces are sandwiched in the fixture and have less exposure to circulating air.

In a forced convection scheme, the airflow velocity v is not measured. Both v and h_{surf} would have to be parameterized since different airflow velocities result in different heat transfer coefficients. Parameters K_{xy}, K_z, ρc, and h_{side} would remain unchanged since they are independent of the flow conditions. One could deduce the heat transfer coefficient h_{surf}

from the airflow velocity given the heat transfer relations provided in literature for flow over flat plates [55]. However, in this case, the complex geometry of the flow area between the cells due to the spacer would result in a heat transfer coefficient that is different from what could be deduced from literature relations. As such, to parameterize v and h_{surf}, the authors reverted to coupling the parameterization with a finite element model and characterize the heat transfer coefficient as a function of different flow rates. At this stage, though, only one flow rate condition was used and validated against.

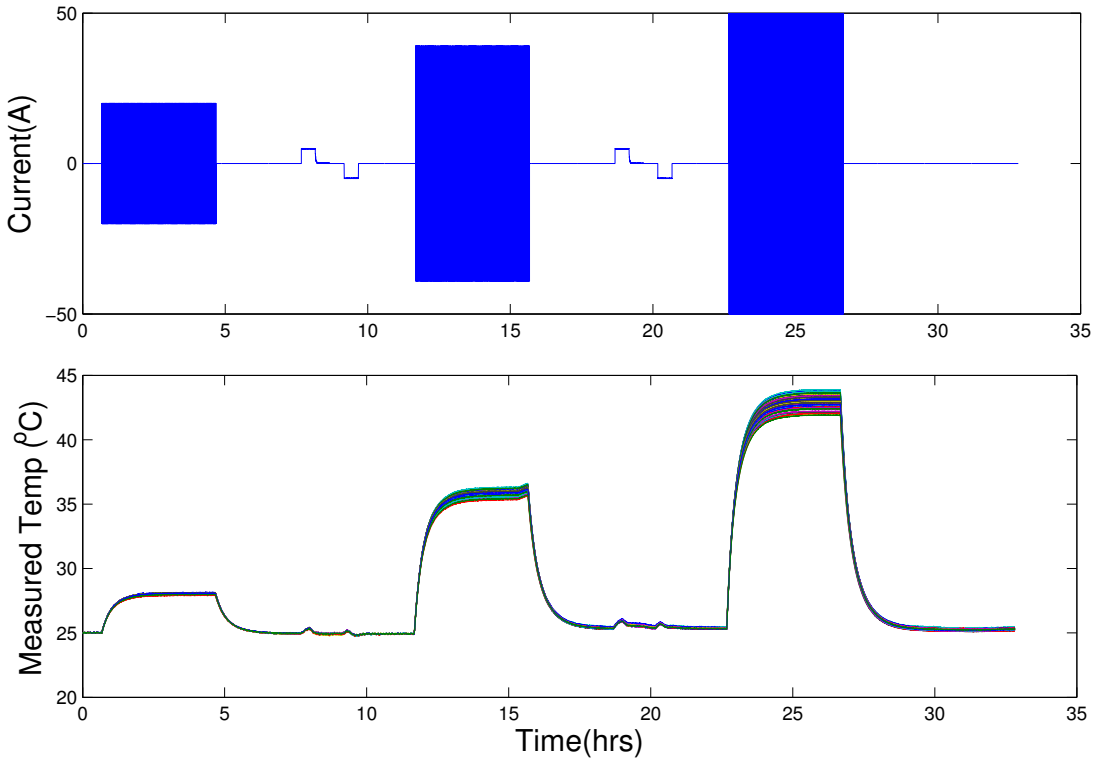

Figure 2.10: Current profile used for thermal parameterization at 25^oC and the corresponding measured surface temperatures

Table 2.1: Identified thermal parameters under a natural convection scheme

$Parameter$	Jelly roll	Aluminum casing	Air gaps
$K_{xy}[\ W/m^2K]$	**22**	237	0.024
$K_z[\ W/m^2K]$	**1.7**	237	0.024
$h_{surf}[\ W/mK]$	—	**6**	—
$h_{side}[\ W/mK]$	—	**18**	—
$(\rho c)[\ J/m^3K]$	**2.75e6**	$2.42e6$	1200

2.2.5.2 Step 2: Finite Element Model (FEM) coupling

In this step, a finite element model was implemented to identify the air flow velocity, v, produced by the cooling fan. The K_{xy}, K_z, h_{side} and ρc identified in step 1 were assumed unchanged and were assigned to the finite element model. The 20A, 39A, and 50A excitation currents shown in Fig. 2.4 were applied under a forced convection scheme with constant fan speed. The mean air flow velocity, v, was identified first using the 39A pulsing experiment as the training date set. Then the 20A and 50A pulsing experiments were used for validation. The identified v was then fed into Eq. 2.9 for the parameter identification of the corresponding h_{surf} in the electro-thermal model.

The finite element model setup[1] is illustrated in Fig. 2.11. The battery cell is composed of the jelly roll and the outside aluminum casing. The 0.6 mm thick aluminum casing was modeled using a thin conductive layer, which is a boundary coupling feature in COMSOL software environment. Therefore, the aluminum casing is not physically drawn in Fig. 2.11. The jelly roll touches the aluminum casing on the side and bottom, leaving an internal empty space in the cell. This empty space is filled with air and small amounts of electrolyte. The electrolyte was neglected in the finite element analysis for simplicity. The entire fixture has three cells and four spacers, forming a symmetric geometry with the symmetric plane splitting the middle cell as shown in Fig. 2.11. Therefore, only half of the geometry is necessary for finite element analysis. The symmetric plane is marked by the yellow dotted line. The spacers create air path over the cell side surfaces for cooling. The cells and the spacers were clamped together using two Garolite blocks, which were not physically modeled in 3D but were mathematically modeled as thermal insulation boundary condition due to its low thermal conductivity. The top surfaces of the cells were mostly covered

[1]This work has been done by Boyun Wang, PhD in mechanical engineering, University of Michigan, Ann Arbor

by plastic terminal blocks and were also modeled as thermal insulation. The cooling fan was modeled by uniform normal air flow velocity on the outlet boundary. Air at ambient temperature enters the fixture through the air inlet and exits the fixture through the outlet at a higher temperature. In addition, the fixture setup allows a portion of the cooling air to go through a bypass channel under the cells and then enter the space between the cells from the bottom.

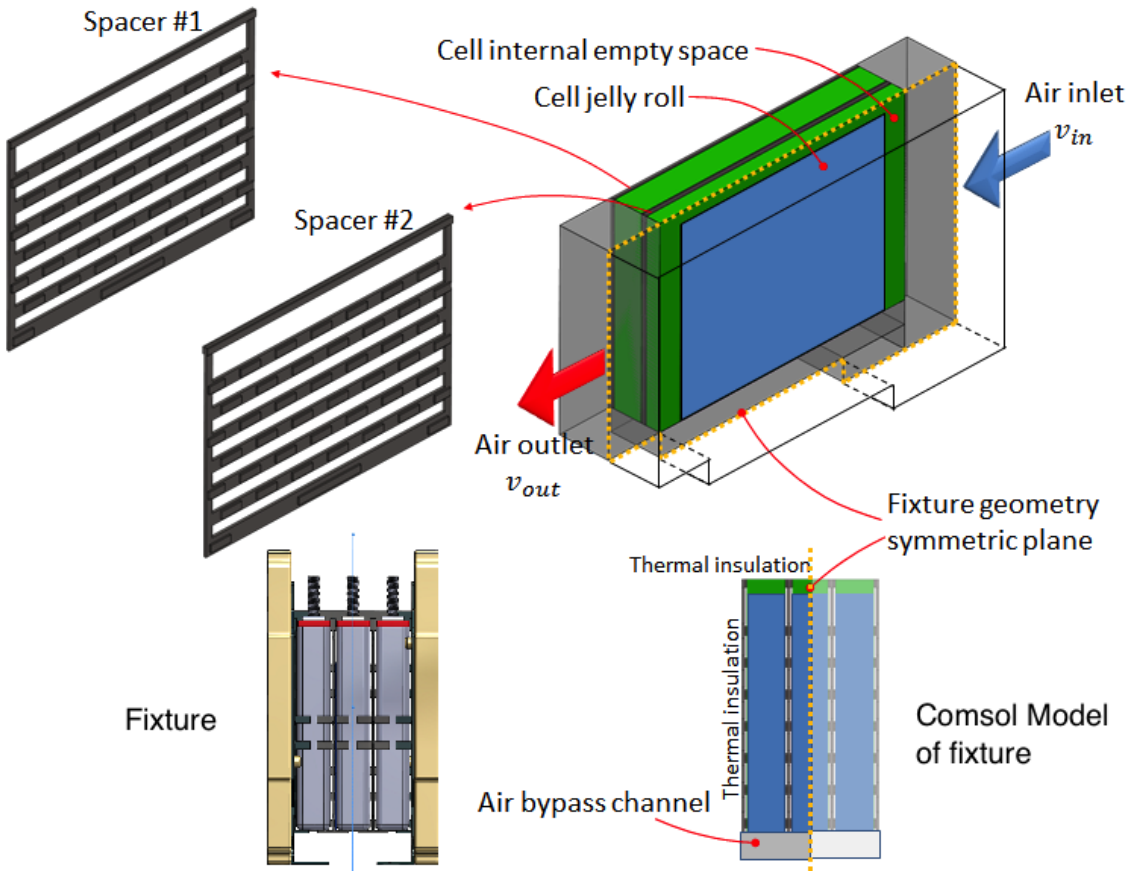

Figure 2.11: 3D finite element model of the 3-cell fixture

The whole geometry was meshed with free tetrahedral structure at element sizes between 1 and 4.5 mm. This is sufficient to maintain good element quality for the 2.4 mm spacer between cells. Conjugated heat transfer solver module was used to compute the air dynamics together with heat convection and conduction. Navier-Stokes equations for compressible fluid were used to model the air flow.

Since the finite element model results in air flow velocity over the surface of the cell that is non-uniform due to the complex geometry of the dimples of the spacer, the outlet velocity, v_{out}, at the air outlet (refer Fig. 2.11) was used in the tuning process. The mean air flow

velocity, v, which will be used in the electro-thermal model, could then be approximated using Eq. 2.12,

$$\frac{v_{out}}{v} = \frac{A_{out}}{A_{cells}}, \tag{2.12}$$

where A_{out} is the air outlet surface area, and A_{cells} is the area of airflow between the cells. In this approximation, air is assumed incompressible.

The iterative process of tuning v_{out} consisted of minimizing the error, E, between the cell surface temperature measurements and COMSOL simulation results at the surface sensor locations, which are marked in Fig. 2.12. Also shown in Fig. 2.12 are the streamlines of airflow over the surface of the cell.

Due to the fact that surface temperature decreases as flow rate v_{out} increases, the optimization logic was defined by Eq. 2.13,

$$v_{out}(\zeta + 1) = v_{out}(\zeta) + dE(\zeta), \tag{2.13}$$

where $v_{out}(\zeta)$ is the outlet air flow velocity at the ζ^{th} iteration, and d is the parameter tuning gain. The iteration error at the ζ^{th} iteration, $E(\zeta)$, is defined by Eq. 2.14,

$$E(\zeta) = \frac{1}{36}\sum_{n=1}^{36}(\bar{T}_n - T_n(\zeta)), \tag{2.14}$$

where n is the sensor location index on the cell surface. $\bar{T}_n$ and T_n are the experimental and simulated steady state surface temperatures respectively at the locations of the sensors ($n = 1, ..., 36$). The optimization tuning gain, d, is adjusted for proper convergence. In this particular study, $d = \frac{1}{10}$ was used.

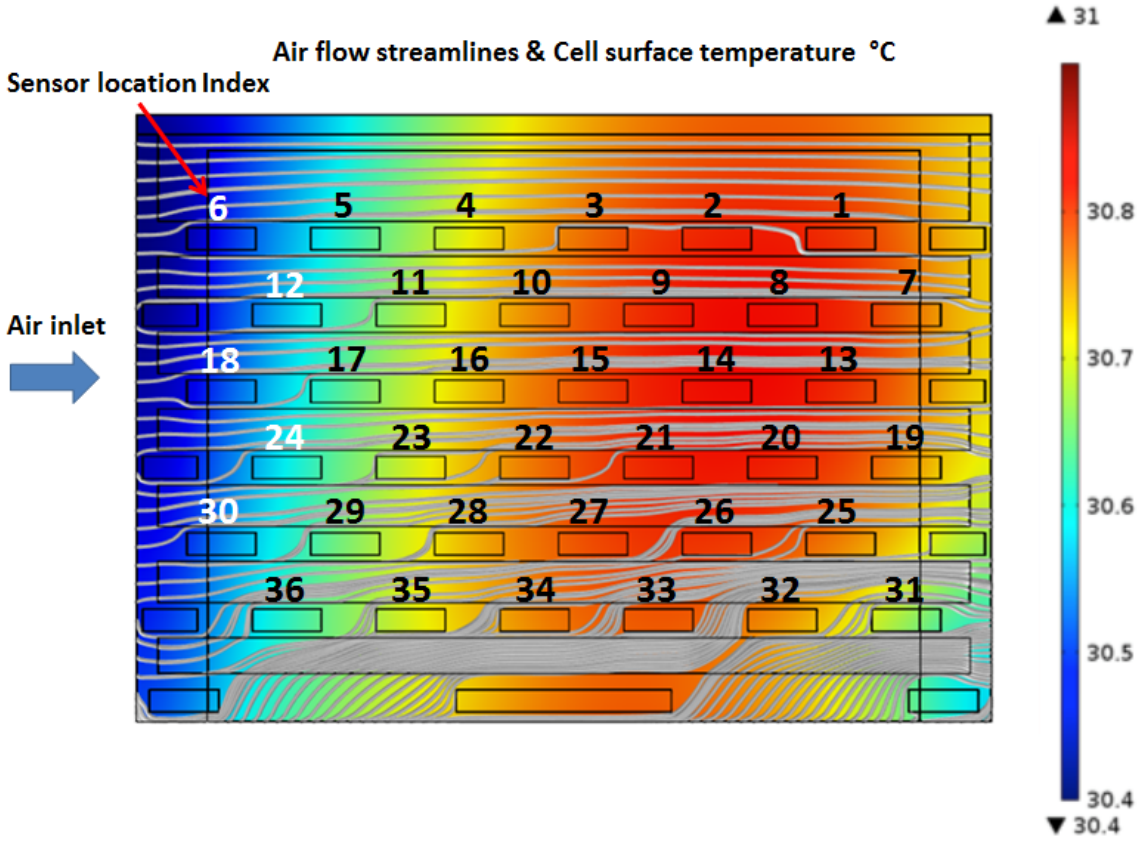

Figure 2.12: Location of the sensors on the surface of the cell and the cell surface temperature distribution for 39A cycling case.

The initial guess of the air outlet flow velocity $v_{out,0}$ was approximated using Eq. 2.15,

$$\begin{aligned} v_0 &= \frac{3Q_{gn}}{(\rho c)_{air}\Delta T_0 A_{outlet}} \\ &= \frac{3 \times 2.546[watt]}{1.15[kg/m^3] \times 1000[J/kg.K] \times 4[K] \times 3986.5[mm^2]} \\ &= 0.416[m/s] \end{aligned} \tag{2.15}$$

where Q_{gn} is the heating power of one cell at steady state when the current excitation is 39A. Q_{gn} is multiplied by a factor of 3 for 3 cells in the fixture. The density and heat capacity of air are ρ_{air} and c_{air} respectively. ΔT_0 is an initial estimate of the temperature increase of the air across the fixture, which is defined as the average air temperature on the outlet minus the air inlet temperature. A_{outlet} is the fixture outlet area.

For the case considered, the fitting process and results are plotted in Fig. 2.13. The air temperature rise across the fixture, ΔT, is plotted in the top graph. Decreasing ΔT

indicates the initial guess of v_{out} is lower than the true value. The outlet air flow velocity v_{out} is shown in the middle plot. In the bottom figure, the value of the optimization iteration error $E(\zeta)$ defined in Eq. 2.14 is compared with the least squares error $F(\zeta)$, which is defined in Eq. 2.16,

$$F(\zeta) = \frac{1}{36}\sqrt{\sum_{n=1}^{36}(\bar{T}_n - T_n(\zeta))^2}. \tag{2.16}$$

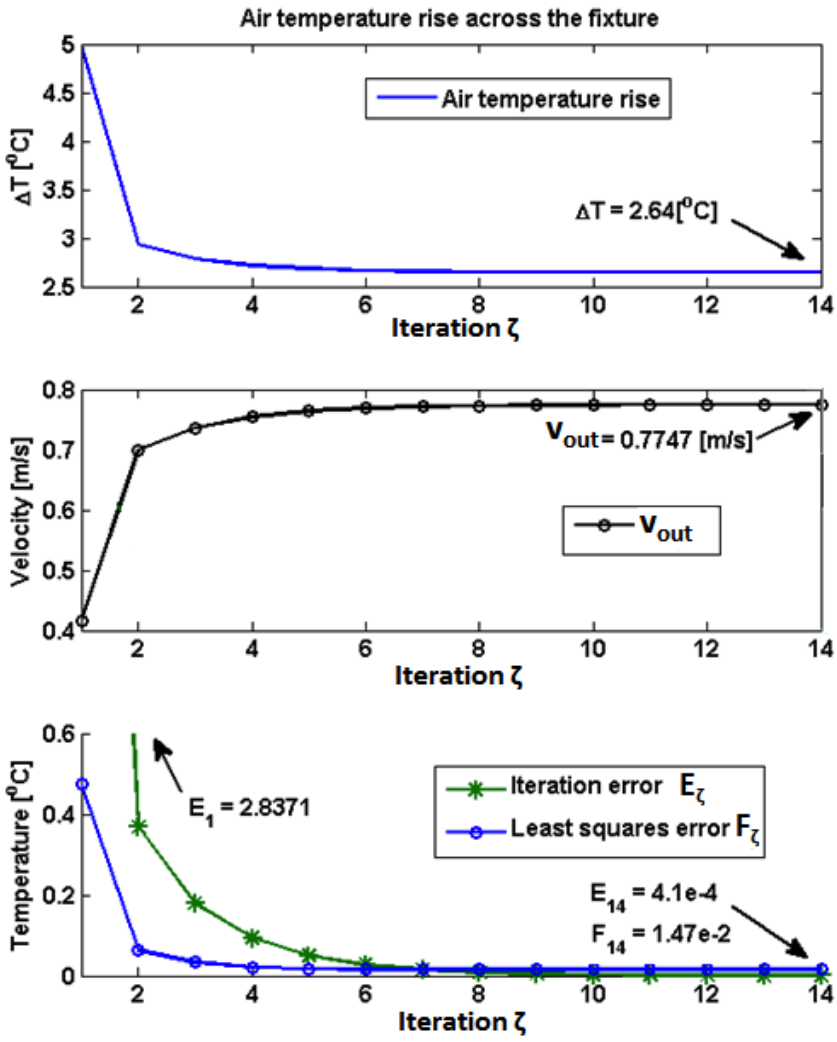

Figure 2.13: Numerical model parameterization process using the optimization logic defined in Eq. 2.13.

The final outlet air flow velocity was $v_{out} = 0.8m/s$, and was validated using the

other 2 forced convection experimental data sets (20A and 50A current excitation). The mean flow velocity between the cells, v is then calculated using Eq. 2.12 and fed back into the electro-thermal model. Given that parameters K_{xy}, K_z, h_{side}, ρc and v are now known, the surface heat convection coefficient, h_{surf}, is tuned against the 39A excitation data with forced convection. The identified h_{surf} was then validated against the other 2 data sets (20A and 50A) under a forced convection scheme. Temperature results from all 3 experiments using COMSOL and the electro-thermal model along with the experimental data are illustrated in Fig. 2.14 at the 36 sensor locations.

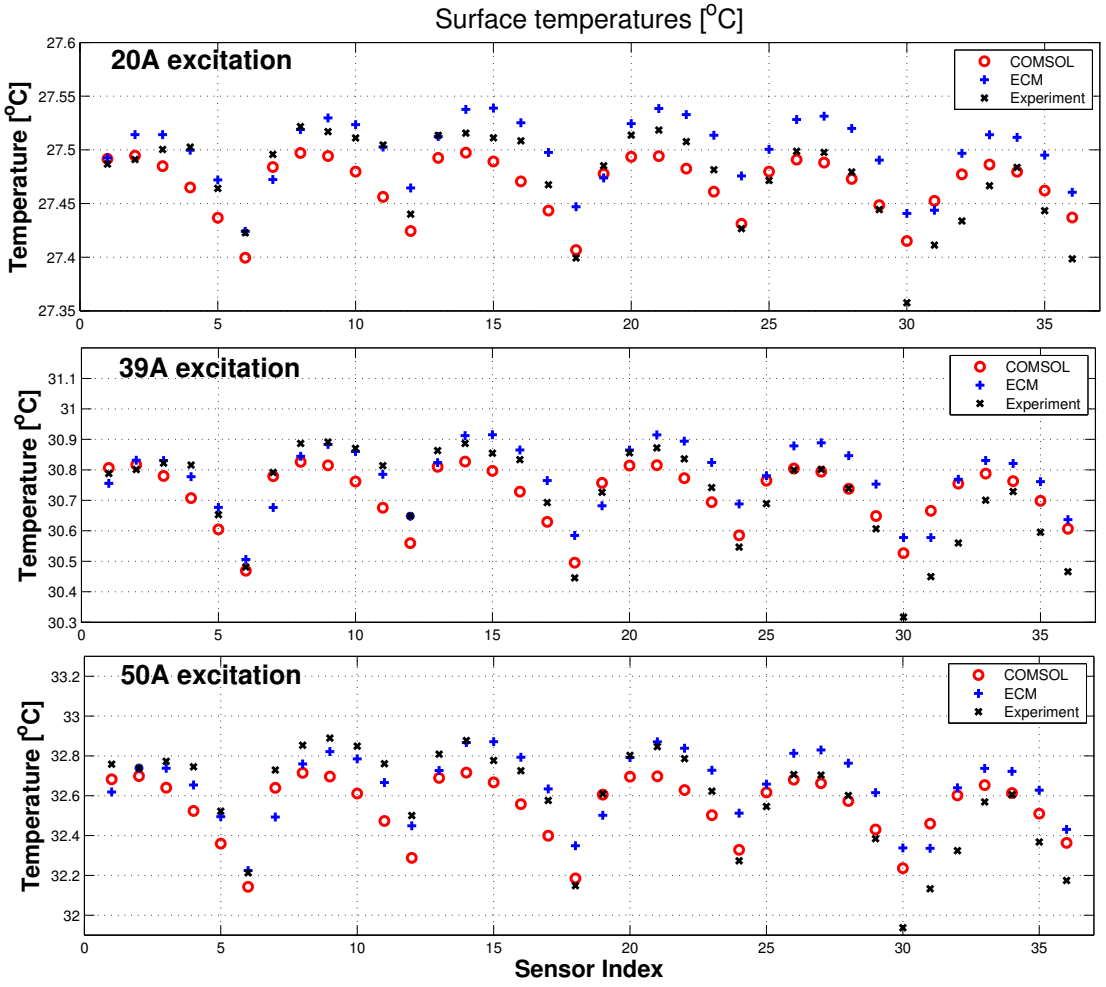

Figure 2.14: Temperature rise at steady state at the 36 sensor locations using COMSOL, ETM and experimental data using a 20A, 39A and 50A excitation profiles

Table 2.2: Experiments used for validation of coupled ETM

Experiment	Temperature (^oC)	Current Amplitude (A)	SOC (%)	Pulse profile	$V_{RMSE}(mV)$	$T_{max,RMSE}(^oC)$	$T_{min,RMSE}(^oC)$	$T_{avg,RMSE}(^oC)$
Pulse	25	25	50	50/5 sec	5.5	0.1	0.2	0.1
Pulse	25	50	50	50/5 sec	7.9	0.3	0.4	0.3
Pulse	25	25	25	50/5 sec	8.6	0.1	0.2	0.1
Pulse	25	25	75	50/5 sec	2.8	0.2	0.2	0.2
Pulse	10	50	50	50/5 sec	8.5	0.4	0.6	0.4
Pulse	-5	50	50	50/5 sec	8.8	1.3	1.8	1.3
US06	25	—	—	—	15.5	0.3	0.4	0.2
Cold FTP	-5	—	—	—	14.7	0.8	2.3	1.2
Urban Assault	25	—	—	—	12.9	0.2	0.3	0.2

2.3 Validation results

In this section, the proposed equivalent circuit model is validated against several experiments that considered different duty cycles and pulse experiments at different temperatures, states of charge, current amplitude and pulse width. The model is validated and shows agreement with all experiments both electrically (terminal voltage) and thermally (surface temperature) within the RTD sensor accuracy of 0.5^oC. Table 2.2 summarizes the list of experiments used for validation and the corresponding root mean square errors (RMSE) on voltage and surface temperature in each case.

The first column in Table 2.2 indicates the type of experiment. The second, third and fourth columns indicate the temperature, SOC and current amplitude at which the experiment was performed. Column 5, which is the pulse profile, has 2 entries which indicate that the first set of pulses have a width of 50 sec, and the second set have 5 sec.

2.3.1 Pulse excitation experiments

In this section, the coupled ETM is validated against pulsing experiments for varying temperatures, SOCs, current amplitudes and pulse widths. Figure 2.15 shows the current profile, corresponding SOC, voltage and thermal response, and a spatial temperature distribution profile for both the measured and simulated ETM data at a specified time t for a given pulsing experiment. Plots of temperature vs. time show the minimum, maximum and average (simulated and measured) surface temperature evolution. The average interior temperature is also plotted and it shows that the difference between the average interior and average surface temperature is less than 1^oC. Notice from the surface temperature plots that there is a small shift in the location of the hot spot towards the exit side of the airflow. The results of pulsing experiments with different conditions (ambient temperature, nominal SOC, pulse amplitude and width) are tabulated in Table 2.2. The results in Table 2.2 indicate that for higher current rates, the RMSE values are slightly higher than those for lower current rates. This suggests that electrical parameters could be a function of C-rate

and could be parameterized accordingly. Moreover, the pulse experiment at -5^oC shows that the RMSE on voltage is 8.8mV which is in good agreement with the results at other pulsing experiments, but the RMSE for the minimum and maximum temperatures exceeds 1^oC. This could suggest that, at lower temperatures, the parameterized thermal properties could be different.

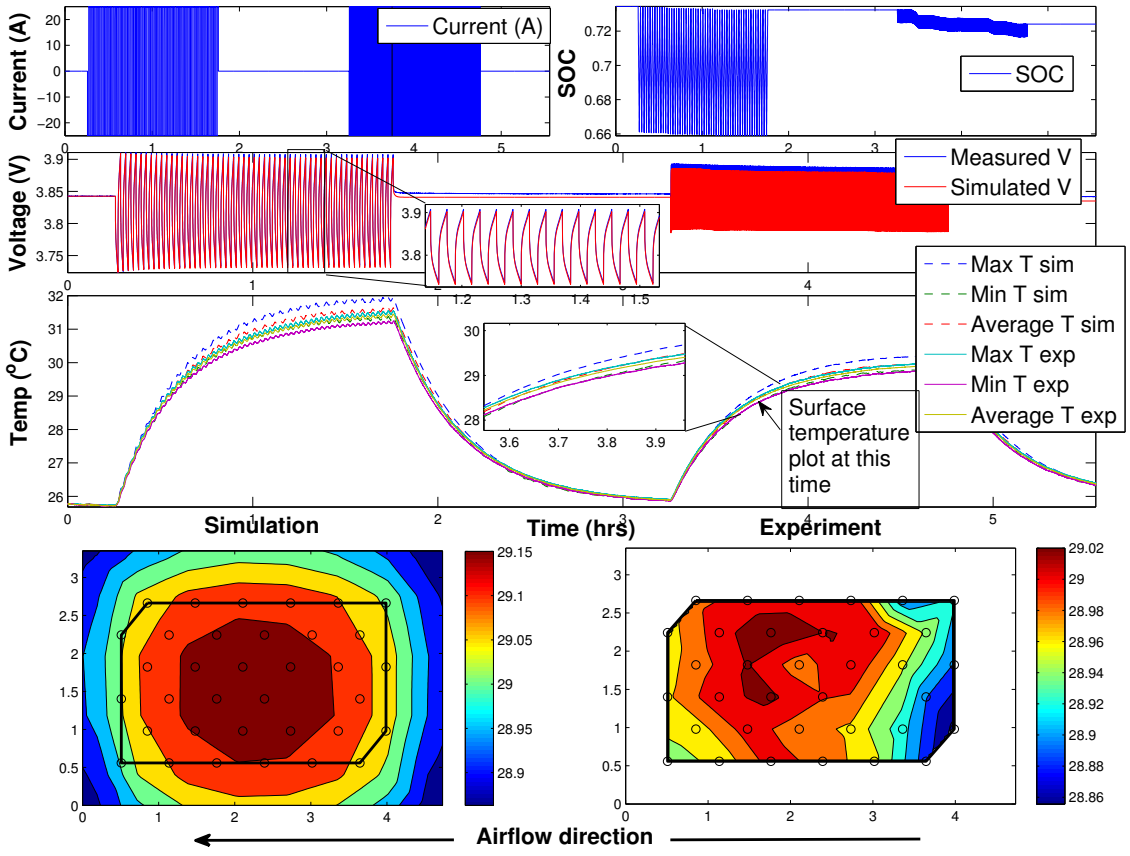

Figure 2.15: Pulse validation experiment at 25^oC, 75% SOC, and 25A (5C rate) current amplitude

2.3.2 Duty cycle validation

Three duty cycles have been used for validation in this section. The US06 duty cycle was scaled down to match the power capabilities of our battery. The ETM also showed good agreement between the measured and simulated voltages and temperatures for the US06 duty cycle and the urban assault cycle shown in Fig. 2.16 and 2.17. The model does a good job of capturing the surface temperature distribution given the fact that the sensor accuracy is around 0.5°C. However, for the Cold FTP cycle the RMSE on the estimated

voltage is comparable to that of the US06 cycle, but the RMSE on temperatures is higher as shown in Table. 2.2. This agrees with what was shown earlier in section 2.3.1 that at lower temperatures, the RMSE on temperatures is large. These observations need to be examined further to understand the effect of temperature (especially lower temperatures) on spatial temperature distributions in a prismatic lithium-ion cell.

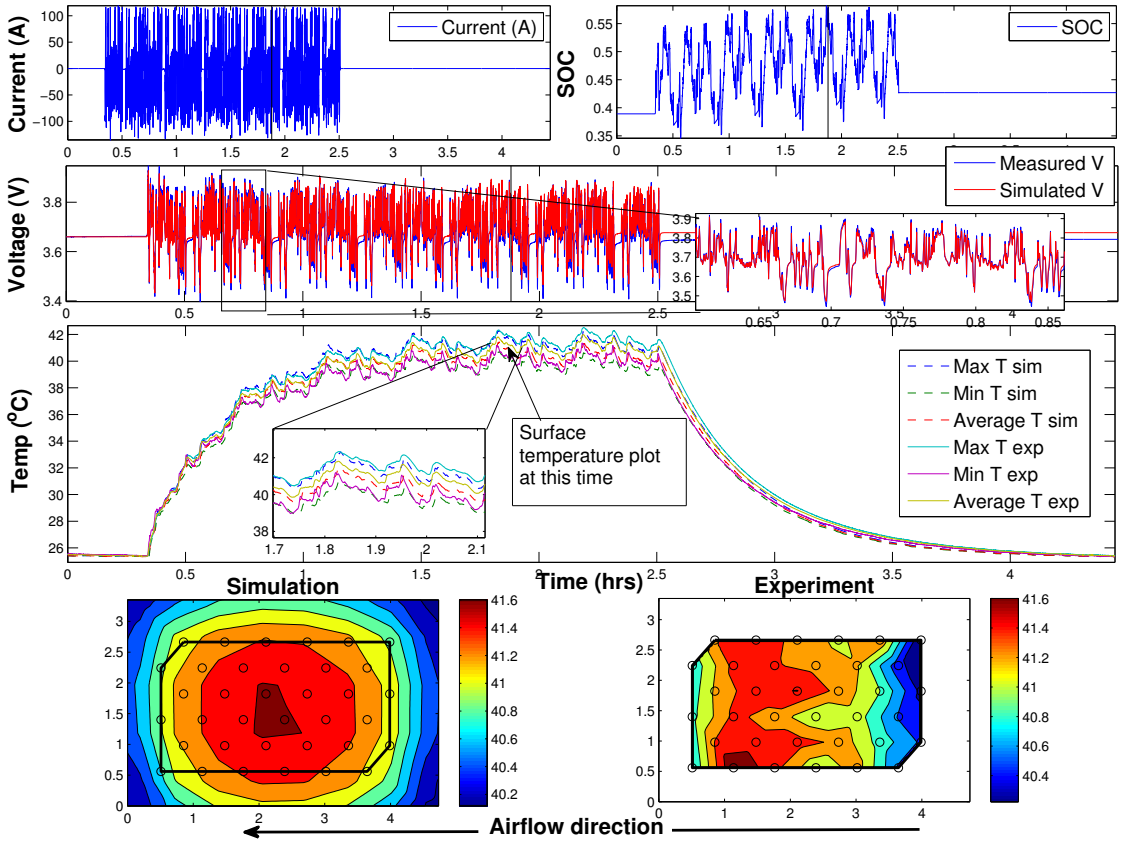

Figure 2.16: US06 duty cycle validation at 25°C

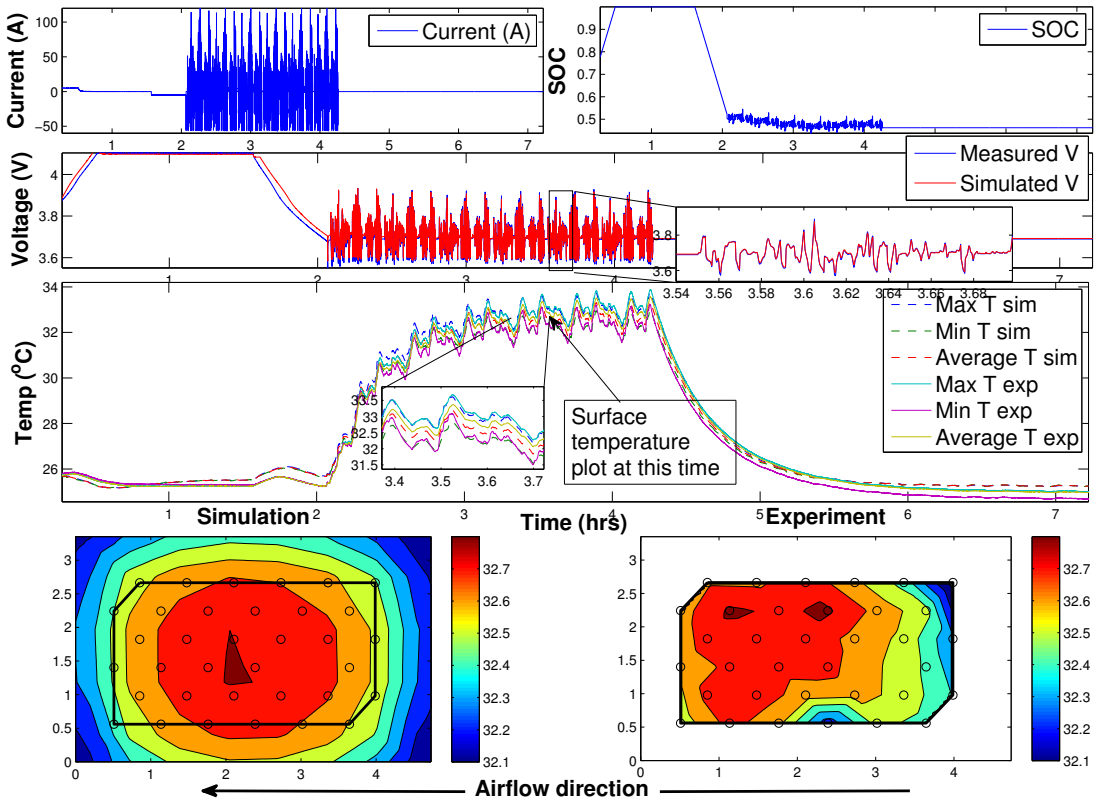

Figure 2.17: Urban assault duty cycle validation at 25°C

2.4 Conclusions

A methodology for coupling the parameterization of an ECM with a FEM has been presented, which allows for the parameterization of the ECM in replicated pack conditions. Also, the ECM developed in this study was validated against a wide range of experimental conditions that span a wide range of experimental conditions. The model couples a 2D distributed double RC model network with a 3D thermal model for a lithium ion prismatic cell. The analysis was done on a prismatic NMC lithium ion battery. The presented ECM showed good agreement with experimental data under different experimental conditions. Validation was done using different pulsing profiles ($T_{amb} \in [-5, 10, 25]^oC$, $I \in [25, 50]A$, $SOC \in [25, 50, 75]$, and pulse width $\in [5, 50]sec$) and different duty cycles ($T_{amb} \in [-5, 25]^oC$). The coupling between the electrical and thermal model was established through local heat generation and temperature. The different layers of the jelly roll inside the aluminum case of the battery were simplified by assuming an average heat capacity and density, and by introducing anisotropic thermal conductivities (K_{xy} and K_z).

Based on the electrical parameterization, the electrical parameters are a function of state of charge and temperature. Thermal parameterization under a natural convection scheme resulted in thermal conductivities that are an order of magnitude different. Parameterization of the airflow parameters was done under a forced convection scheme by coupling the ECM with a high fidelity finite element model, and using the thermal parameters identified using the natural convection scheme. The distributed nodal mesh allowed for validation with thin film RTD sensors mounted across the surface of the cell. This lumped parameter model has shown sufficient to capture the electro-thermal dynamics of an encased cell since it is hard to observe any significant distributed temperature behavior. Chapter 3 will investigate the optimal sensor placement on the surface of the battery. An optimal sensor placement means faster and more accurate temperature prediction of the unknown interior temperature of the cell.

CHAPTER 3

Optimal temperature sensor placement

3.1 Introduction

In many engineering applications, it is important to determine the state of a system or sub-system using only partial measurements of that system states. Of particular interest in hybrid electric vehicle applications is the measurement of the cell temperature in a battery pack. Monitoring temperature allows for control algorithms that can prevent excessive temperature rise and ultimately prevent thermal runways [14]. Although higher temperatures enhance the lithium transport kinetics, it is well established that excessive temperatures can also result in degradation in battery cells [56, 57, 58], and must be monitored.

Complex and expensive packaging and engineering schemes are required to position temperature sensors close to the regions of interest. Insertion of thermistors between battery cells is infeasible because the thickness of the sensors ($>$1mm) will cause failure or rupture of the cells due to compression on the thick sensors. However, new sensor technologies are emerging that enable the placement of temperature sensors anywhere on the cell surface at lower cost and without causing risk of battery failure. These sensors are thin film RTD (resistance temperature detector) sensors that are supplied by General Electric Global Research. The RTDs have a low profile, flexible structure that allows placement between cells without obstructing airflow for cooling or possibly damaging the cells. The RTDs are fabricated on a flexible Kapton substrate and the elements are composed of Platinum (Pt) with a nominal 100 ohm resistance. The total thickness of the sensor is less than 100 microns which is 10x thinner than the current state of the art temperature sensors used on electric vehicles. The sensors can be placed anywhere on the surface of the battery as shown in Fig. 3.1. This motivates an observability analysis to determine the optimal location for a sensor on the surface of the cell. Since the core temperatures of the cell are of interest, maximizing observability, in this chapter, is defined as identifying optimal sensor locations for the best estimation of the core temperatures.

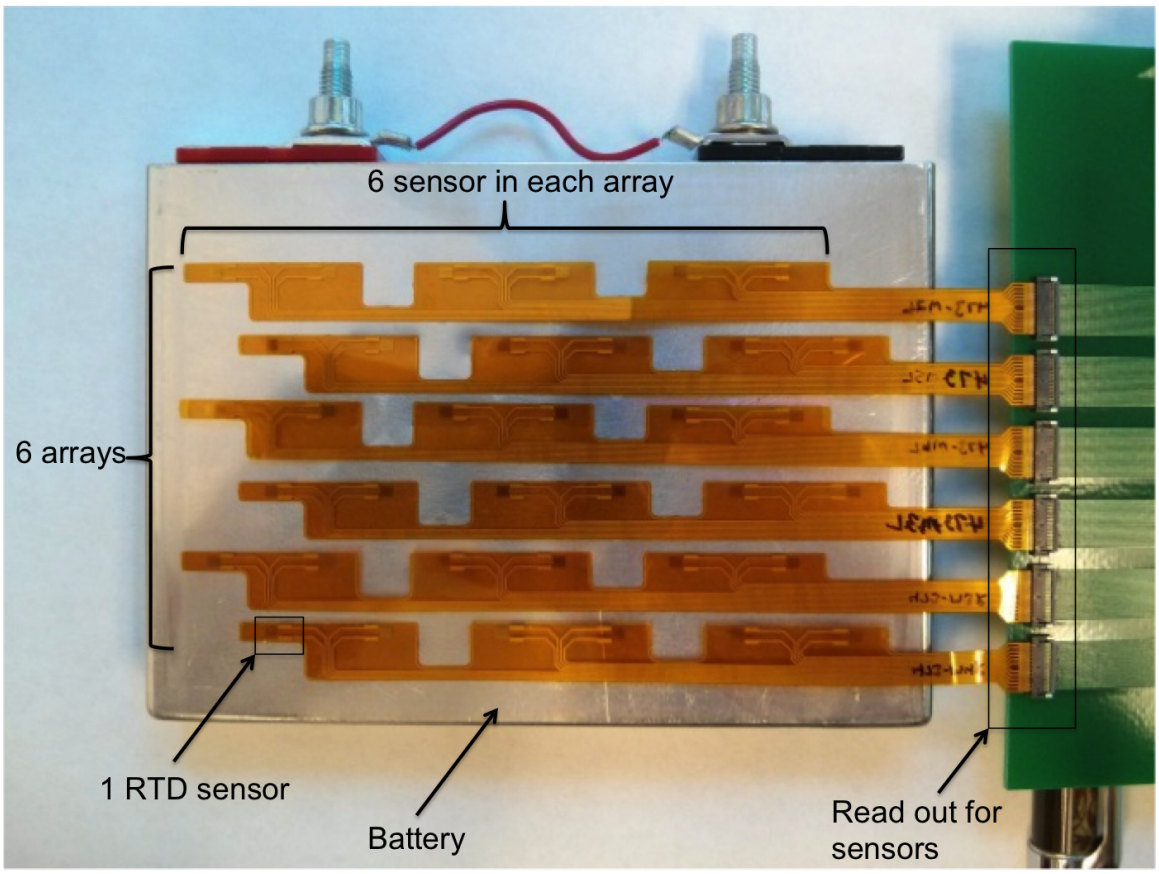

Figure 3.1: RTD sensor placement on the surface of a battery.

Optimal sensor and actuator placement has been the focus of significant research in the controls community. The optimal locations for sensors and actuators for parabolic PDEs, which include the heat equation, have been widely investigated [59, 60]. In [61], Georges looked at the optimal sensor and actuator locations in both discrete and continuous time domains based on the observability and controllability gramians. This concept of looking at observability for defining optimal sensor placements is of major importance because it allows for the best estimation of unknown system states using the sensor data. Several papers have looked at aspects of observability for PDEs [62, 63]. In [64], Wolf et al. studied the optimal sensor placement in battery packs by performing eigen decomposition of the heat equation PDEs that govern the entire battery pack and looking at the magnitude of their corresponding eigenmodes. However, little work has been done on optimal temperature sensor placements on a single battery cell.

Two methods are presented here for studying the observability and optimal temperature sensor placement on a battery cell with air flow (convection) over its surface to simulate battery pack conditions. The first is an extension to the method presented by Lim where

observability is defined in terms of the projections of the eigenvectors on the observability subspace [27], while the second looks at the trace of the gramian matrix [65]. The advantage of using the first method is that it is possible to maximize observability of certain nodes of interest, such as core nodes of a battery cell. The second method looks at maximizing observability for the system as a whole and is a more traditional method of looking at observability.

3.2 State space Representation

The model presented in Chapter 2 is nonlinear. The nonlinearity is present in the form of temperature dependent resistances (R_s, R_1 and R_2), and entropic heat generation $IT\frac{dU}{dT}$.

For any given profile or excitation input, the steady state value is found using the nonlinear model, and linearization is done around that steady state value for both the temperature dependent resistances (R_s, R_1 and R_2), and the entropic heat generation $IT\frac{dU}{dT}$, where for the resistance:

$$R(T) = R(T_{eq}) + \left.\frac{\partial R}{\partial T}\right|_{T_{eq}} (T - T_{eq}). \tag{3.1}$$

and for the entropic heat generation $f(I^2, T) = IT\frac{dU}{dT}$:

$$f(I^2, T) = f(I^2_{eq}, T_{eq}) + \frac{\partial f}{\partial I^2}(I^2 - I^2_{eq}) + \frac{\partial f}{\partial T}(T - T_{eq}). \tag{3.2}$$

where $\frac{\partial f}{\partial I^2}$ is calculated as:

$$\frac{\partial f}{\partial I^2} = \frac{1}{2I_{eq}}(T_{eq}\frac{dU}{dT}). \tag{3.3}$$

Note that linearization is done with respect to I^2 and T since I^2 is an input to the system, and T is a state variable. Accordingly, the system can thus be written in state space representation as:

$$\begin{aligned} \dot{\mathbf{T}} &= A\mathbf{T} + B\mathbf{u}. \\ \mathbf{y} &= C\mathbf{T}. \end{aligned} \tag{3.4}$$

Where $\mathbf{T} = [T_1, T_2, ..., T_n]^T$ is the matrix of state variables of temperatures at each node and $\mathbf{u} = [I^2, T_{amb}]^T$ is the input to the system. A and B are the system matrices that correspond to linearizing Eqs. 2.2 and 2.9 and C is a matrix defining the locations of sensors

on the system, and thus the observable output $\mathbf{y}$, where:

$$C = \begin{bmatrix} 0 & 1 & \dots & 0 \end{bmatrix}. \tag{3.5}$$

indicates that, for example, only one sensor at node 2 is placed.

3.3 Sensor placement and observability

Several methods have been proposed for studying the observability of ODEs and addressing the issue of optimal sensor placement. The most common metric is the condition number or minimum singular values of the observability gramian matrix W^o. However, for studying the observability of the heat equation, it has been shown that increasing the number of modes of a system will rapidly decrease the value of the smallest eigenvalue, σ^N_{min}, of the observability gramian matrix implying weak observability [66]. After N=8 modes, the smallest eigenvalue, σ^N_{min}, is almost zero. For heat transfer problems, one would be interested in looking at the observability of certain modes or eigenvalues instead of all the eigenvalues of the system. Hence, a different approach for looking at observability has to be established.

Two methods for quantifying sensor placement are analyzed and compared. The first method is based on analyzing the trace of the observability gramian matrix similar to the work done by Fang et al. [65]. This method leverages the fact that a larger trace of the observability gramian matrix W^o tends to result in a higher rank for the matrix [67]. The other method is based upon the work by Lim [27], where optimal sensor placement is found using the orthogonal projections of the eigenmodes onto the observable subspace. This method is expanded upon by studying the projections of certain eigenmodes that are of interest to the application. Thus maximizing the observability of certain nodes instead of the system as a whole.

3.3.1 Trace analysis

For the system defined in Section 3.2, and for a chosen sensor location as defined by matrix C_i, the observability gramian matrix W^o_i is defined as:

$$W^o_i = \int_0^\infty e^{A^T\tau} C_i^T C_i e^{A\tau} d\tau. \tag{3.6}$$

The trace of the matrix W_i^o is defined as:

$$tr(W_i^o) = \sum_{j=1}^{n} \lambda_{ij}(W_i^o). \tag{3.7}$$

where $\lambda_{ij}(W_i^o)$ are the eigenvalues of W_i^o, with corresponding eigenvectors $\phi_{ij}(W_i^o)$.

3.3.2 Eigenmode projections

The method presented applies [27] to achieve maximum observability for certain critical nodes of interest. Those critical nodes are the hottest nodes that correspond to the jelly roll node which cannot be measured. Given the system presented in Section 3.2, a given matrix C_i for the locations of sensors and the resulting observability gramian matrix W_i^o presented in section 3.3.1, one can decompose W_i^o into its eigen decomposition, which would be written as:

$$W_i^o = [U_i \quad U_i^{\perp}] \begin{bmatrix} \sum_i^o & 0 \\ 0 & 0 \end{bmatrix} \begin{bmatrix} U_i^T \\ U_i^{\perp T} \end{bmatrix}. \tag{3.8}$$

where U_i is a matrix with column vectors that form an orthogonal basis for matrix W_i^0, and $\sum_i^o = diag(\lambda_{i,1}, \lambda_{i,2}, ..., \lambda_{i,q})$ is a diagonal matrix of the eigenvalues of W_i^o (where $\lambda_{i,1} \geq \lambda_{i,2} \geq ... \geq \lambda_{i,q}$), and q is the rank of the gramian matrix W_i^o or the dimension of matrix U_i (the threshold for defining the rank is set by default at 9.2×10^{-13} using MATLAB). As outlined in [27], the projection of the eigenvectors, ϕ_{ij}, corresponding to eigenvalues λ_{ij} onto the subspace U_i is:

$$\phi_{ij}^{proj} = U_i(U_i^T U_i)^{-1} U_i^T \phi_{ij}. \tag{3.9}$$

A scalar, α_{ij}, is defined to reflect the relative significance of the corresponding eigenvector ϕ_{ij}, where:

$$\alpha_{ij} = \phi_{ij}^{proj^T} W_i^o \phi_{ij}^{proj}. \tag{3.10}$$

Equation 3.10 implies that α_{ij} takes a larger value when the projected eigenvector, ϕ_{ij}^{proj}, is in the direction of maximum observability. However, since the nodes corresponding to the jelly roll inside the cell are of interest, and observing those nodes is critical, the method presented in [27] is expanded to look at the observability of those critical nodes by analyzing the contribution of the corresponding eigenmodes of those nodes. This expansion of Lim's method is shown in the eigenvalue plot of system matrix A in Fig. 3.2. The plot in Fig. 3.2 corresponds to the eigenvalues when only the chamber fan is turned on to maintain

ambient temperature (resulting in a flow rate of $v = 0.65m/s$ over the surface of the cell). This analysis however could be performed for different ambient and flow conditions.

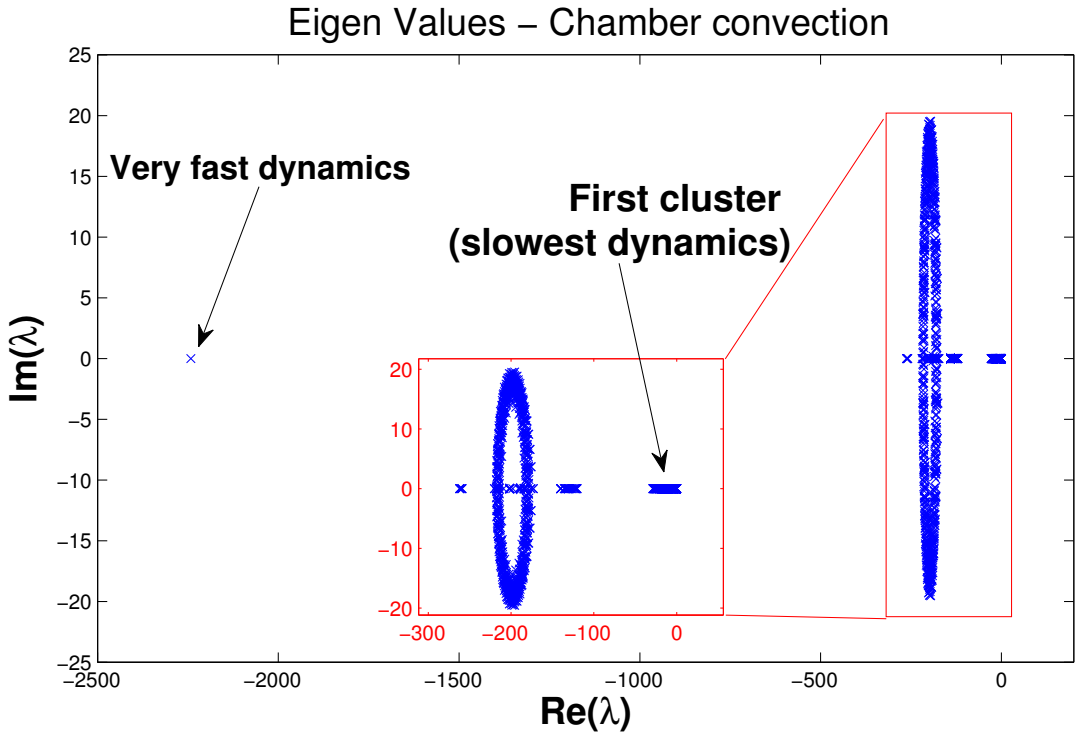

Figure 3.2: Eigenvalue plot of system matrix A

Since each eigenvector corresponding to each eigenvalue in the system represents the contribution of the different states to that eigenvalue, a criteria is established to identify the states that contribute most to the eigenvalues of interest. It is also required that at least the states corresponding or contributing to the slowest dynamics in the system are observed. A procedure for doing such an analysis is outlined below:

Step 1: Choose eigenvalues of interest

---

1. Perform eigen decomposition on system matrix A.
2. For any given eigenvalue, quantify the contribution (β_{ij}^k) of each state to that specific eigenvalue according to:

$$\beta_{ij}^k(\%) = \frac{\left|\phi_{ij}(k)\right|}{\sum_{k=1}^{n_s}\left|\phi_{ij}(k)\right|} \times 100. \tag{3.11}$$

Equation 3.11 above implies that for a given sensor placement represented by matrix C_i, and for a given eigenvalue λ_{ij} with corresponding eigenvector ϕ_{ij}, β_{ij}^k (for k= 1 , ... , n_s = number of states) will represent the contribution of state k to eigenvalue λ_{ij}.

3. Choose the eigenvalues for which the states of interest (such as the core nodes) have the highest mean β_{ij}^k. The eigenvectors, ϕ_{ij}, corresponding to those eigenvalues, λ_{ij}, will be projected onto subspace U_i for observability analysis. This tailors the solution towards maximizing the observability of those states instead of the system as a whole.

Step 2: Perform observability

---

1. Find parameter α_{ij} for each eigenvector of the eigenvalues chosen in ***Step 1*** above using Eq. 3.10.

2. Define a final metric, γ_{ij}, for quantifying the degree of observability of the chosen eigenmodes using a given sensor placement represented by matrix C_i, using the $\mathcal{L}_2$ norm of α_{ij}:

$$\gamma_i = \left\| \alpha_{ij} \right\| . \tag{3.12}$$

where j = 1, 2, ..., n_e sweeps the number of eigenvalues of interest, and i = 1, 2, ..., n_c sweeps the number of possible sensor placements.

3.4 Results

In this section, the results of the trace and eigenmode projection methods are summarized for a given flow rate condition over the surface of the cell (chamber fan convection only). For easier analysis of sensor placement, 23 $\times$18 nodes were chosen such that they coincide with sensor locations (or dimple locations) as shown in Fig. 3.3. In total, there are 23$\times$18$\times$5 = 2070 nodes. Figure 3.3 shows that there are 36 possible sensor locations on the surface of the battery.

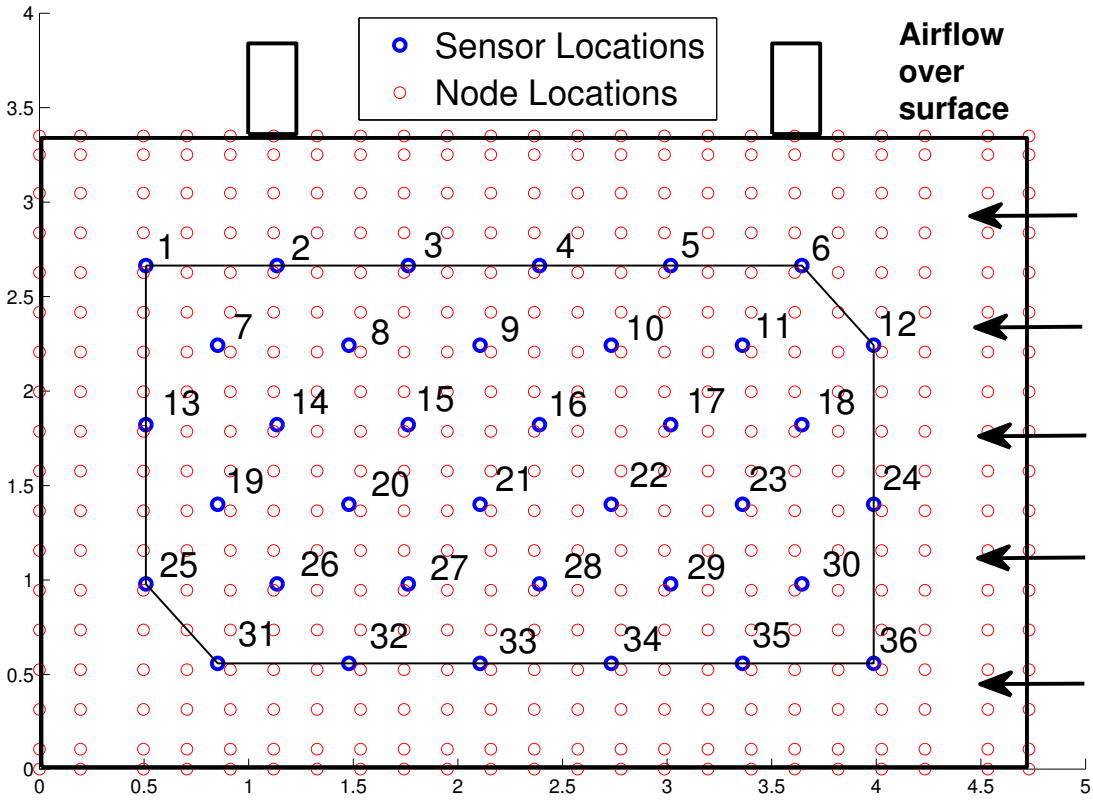

Figure 3.3: Locations of sensors and nodes on the surface of the battery

Analysis is divided into two parts: one sensor analysis, and a strip of 3 sensor analysis. The first analysis highlights the advantage of using sensors placed on the surface as opposed to a thermistor placed closer to the tab (like the Ford C-max placement). The second analysis identifies an optimal location for placing a strip of 3 sensors. However, for the eigenmode projections method, certain eigenvalues of interest have to be chosen first. As shown in Fig. 3.2, a threshold or cutoff is set to chose the eigenvalues with slow dynamics and those for which the jelly roll states contribute the most. A plot of parameter β_{ij}^{k} as a function of the first x number of eiegnvalues is shown in Fig. 3.4. The plot shows that choosing the first 303 slowest eigenvalues and their corresponding eigenmodes captures the slowest dynamics of the battery and constitutes the highest contribution from the jelly roll states. Accordingly, only the first 303 slowest eigenvalues are chosen for the eigenmode projections method that is summarized in sections 3.4.1 and 3.4.2.

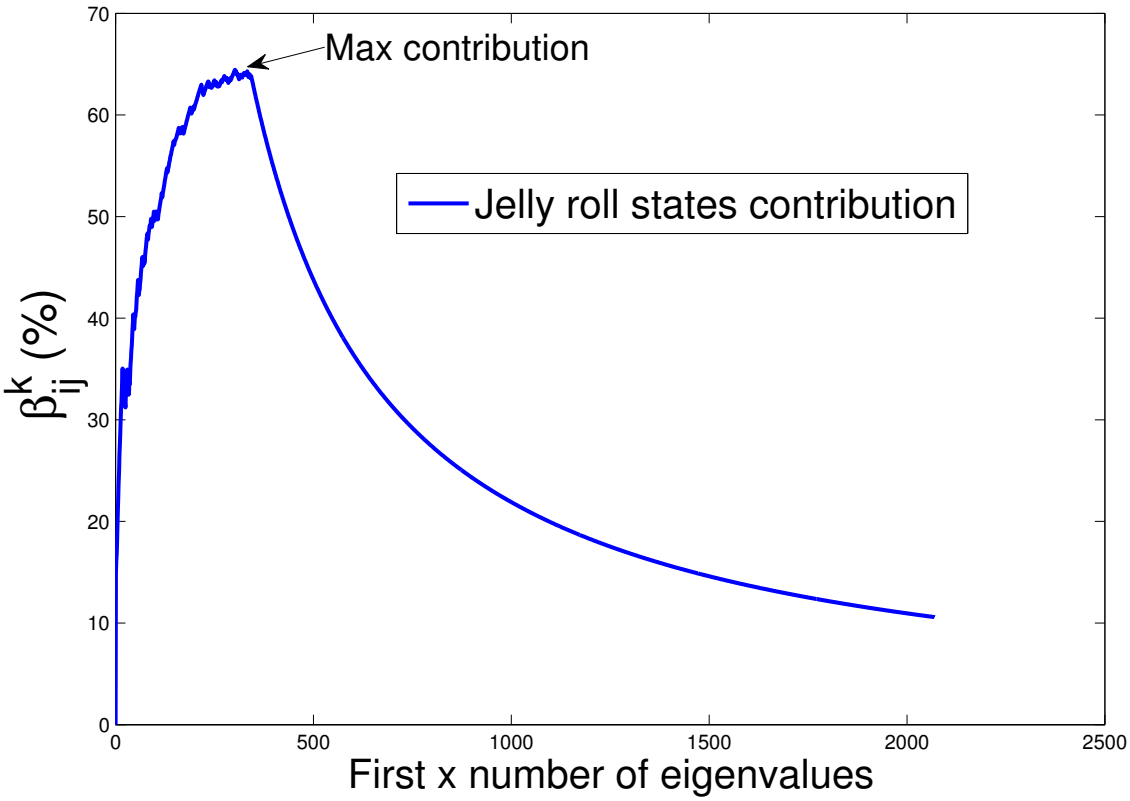

Figure 3.4: Jelly roll states contribution to first x slowest eigenvalues

3.4.1 One sensor analysis

Figure 3.5 shows the trace and γ values for a sensor permuted across all dimple locations (36 dimple locations). This shows that the trace and eigenmode projections method exhibit the same trends but differ slightly in the location of best observability. This could be due to the fact that the trace takes into account all the eigenvalues of the system, while the eigenmode projection method only takes into account some eigenvalues of interest. Moreover, comparing the best location of one sensor on the surface to a conventional sensor placed near the tabs shows that observability is higher for a sensor on the surface than it is for one near the tabs as shown in Table 3.1. This could be explained by the fact that there is an air gap between the jelly roll and the tabs which makes it harder for the heat to flow from the jelly roll to the tabs, but the jelly roll is touching the surface aluminum casing.

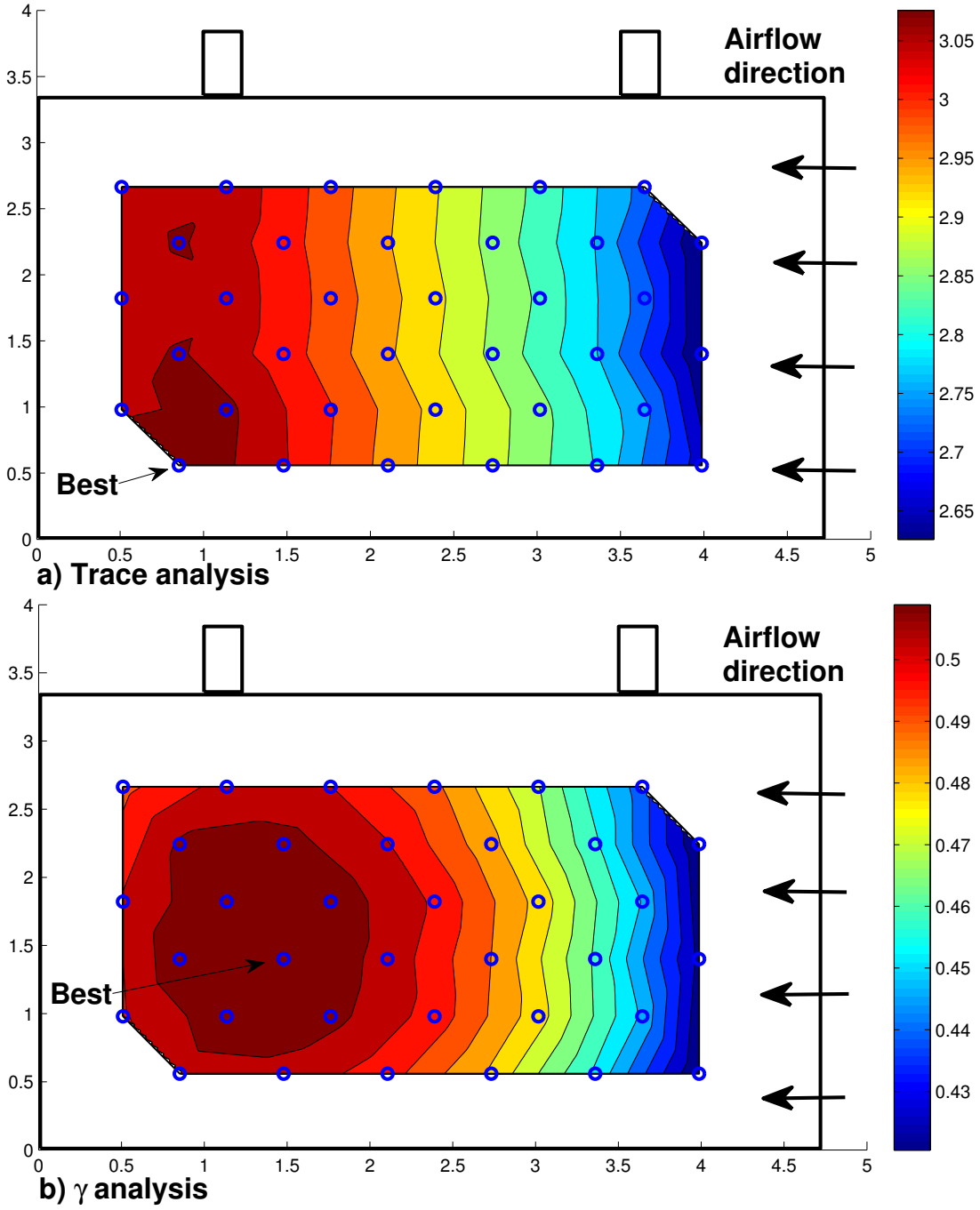

Figure 3.5: Trace and γ based on a single sensor approach

Table 3.1: One sensor summary

Method	Surface	Near tab	%Improvement
Trace	3.109	2.685	15.79
Eigenmode projection	0.515	0.436	18.12

3.4.2 Three sensor analysis

Sensors provided by GE are inline on a kapton strip such that they span dimples in the same row. Given this constraint, the results of the three sensor permutation is summarized in Fig. 3.6. Similar to to the results from section 3.4.1, it can be seen that the best locations for sensors using the trace and eigenmode projection methods are closer to the airflow outlet side, with the worst positions towards the airflow inlet side. Moreover, Table 3.2 shows the percent improvement in observability if 3 sensors are used on the surface as compared to a traditional sensor placed near the tabs. There is a substantial improvement for using 3 sensor on the surface instead of 1 sensor near the tabs (240% improvement). Up to 13% improvement could be achieved when placing sensors closer to the outlet as opposed to the inlet side of the airflow. This is also true for the one sensor analysis where the best locations are at positions 31 (using trace analysis in Fig. 6a) and 20 (using eigenmode projection method in Fig. 6b). This is an obvious observability result since the highest observability measures collocate with the highest measured surface temperatures as shown in Fig. 3.7. This phenomena is explored further in Section 3.4.3, where the inlet flow velocity and current amplitudes are varied and the resulting observability results are analyzed.

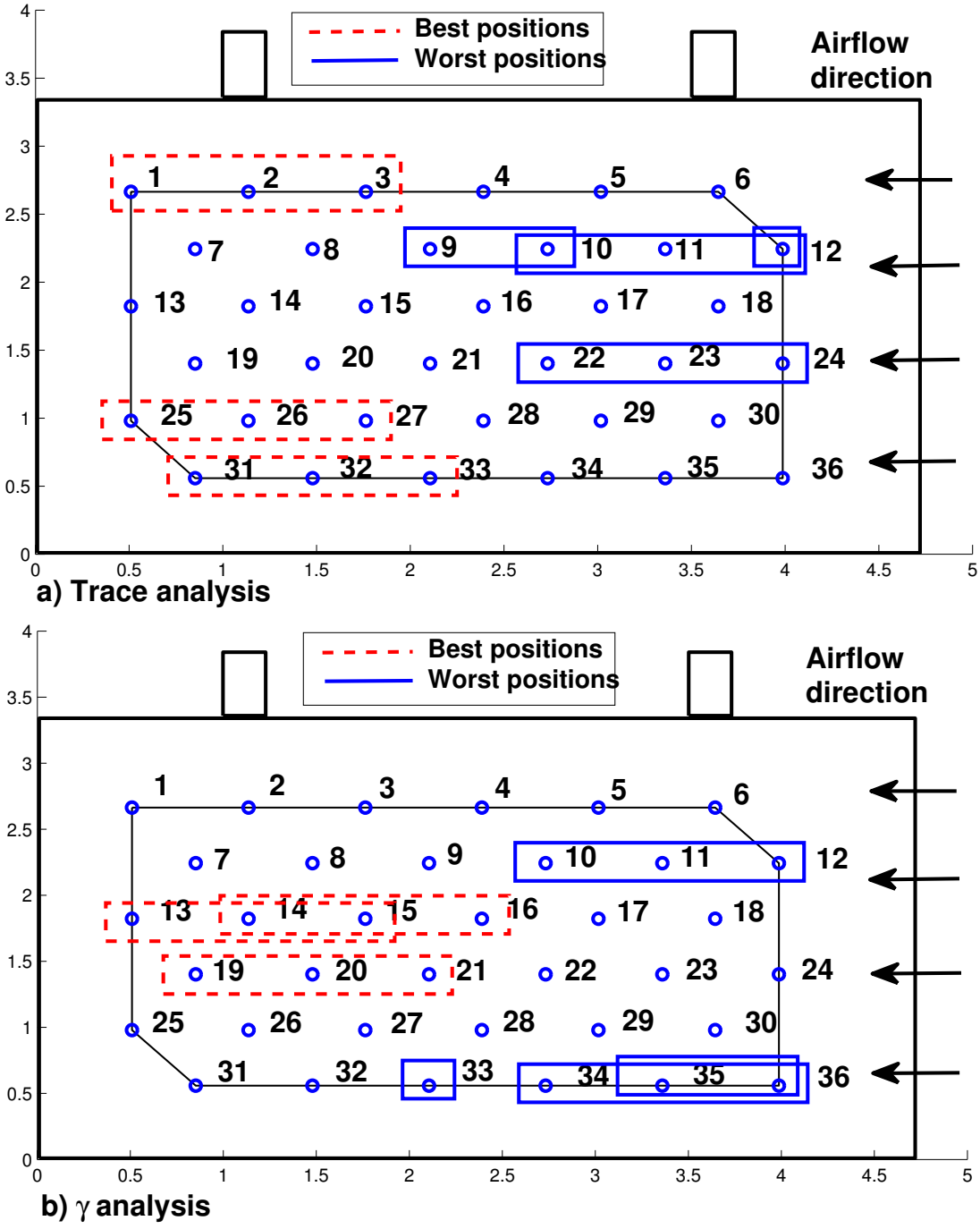

Figure 3.6: Best and worst positions for three sensors using trace and γ analysis

Table 3.2: Three sensor summary

Method	γ (surface)	γ (near tab)	%Improvement
Trace	9.168	2.685	241
Eigenmode projection	1.535	0.436	252

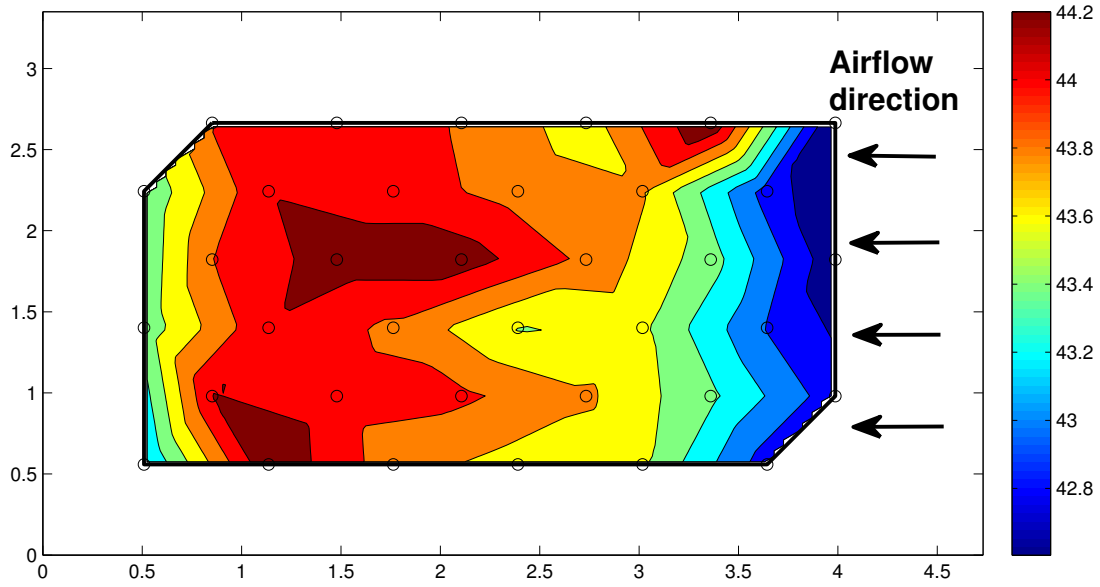

Figure 3.7: Experimental surface temperature (°C) profiles for a 50A charge sustaining pulsing experiment

3.4.3 Varying airflow and current amplitude

The results shown in Section 3.4.1 and 3.4.2 are for an inlet flow velocity of $v = 0.65$ m/s with a 50 A charge sustaining current. In this section, two other different velocities are used to test whether the best observability spot collocates with the hot spot on the surface of the cell. Also the effect of current amplitude on observability is also investigated.

3.4.3.1 Varying airflow

Two different velocities of magnitudes $v = 1.3$ m/s and $v = 0$ m/s are used to investigate the sensor location that provides best observability of the core nodes of the cell. The eigenmode projections method is used for analyzing the results. Figures 3.8 and 3.9 show

the simulated surface temperature distributions (°C) and the resulting observability results using airflow velocities of $v = 1.3$ m/s and $v = 0$ m/s respectively. Notice that the location of the hottest cell surface temperature coincides with the location where a sensor should be placed for estimating the cell core temperature.

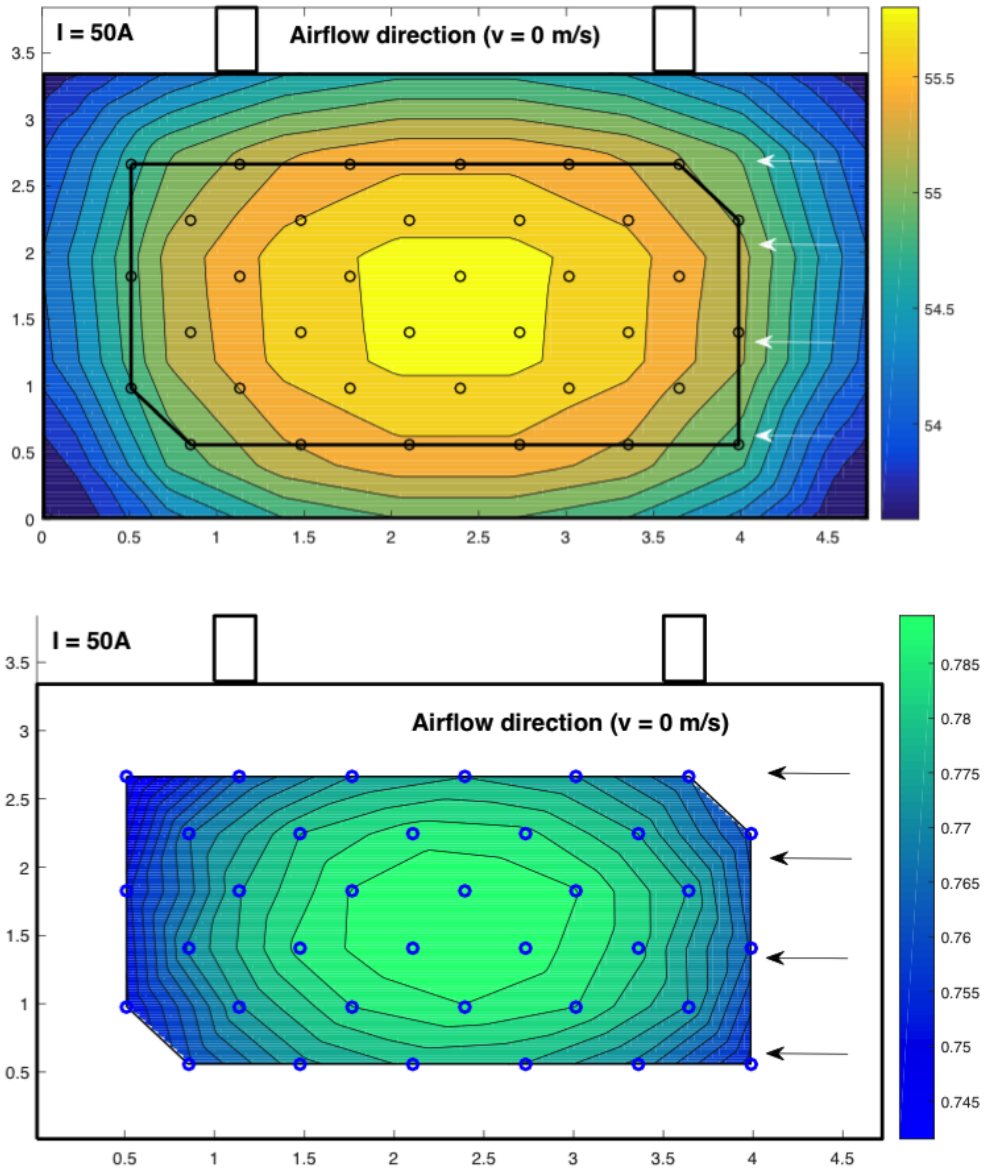

Figure 3.8: Simulated surface temperature distribution (°C) and the resulting observability metric γ for an airflow velocity of $v = 0$ m/s and charge sustaining current amplitude of 50 A.

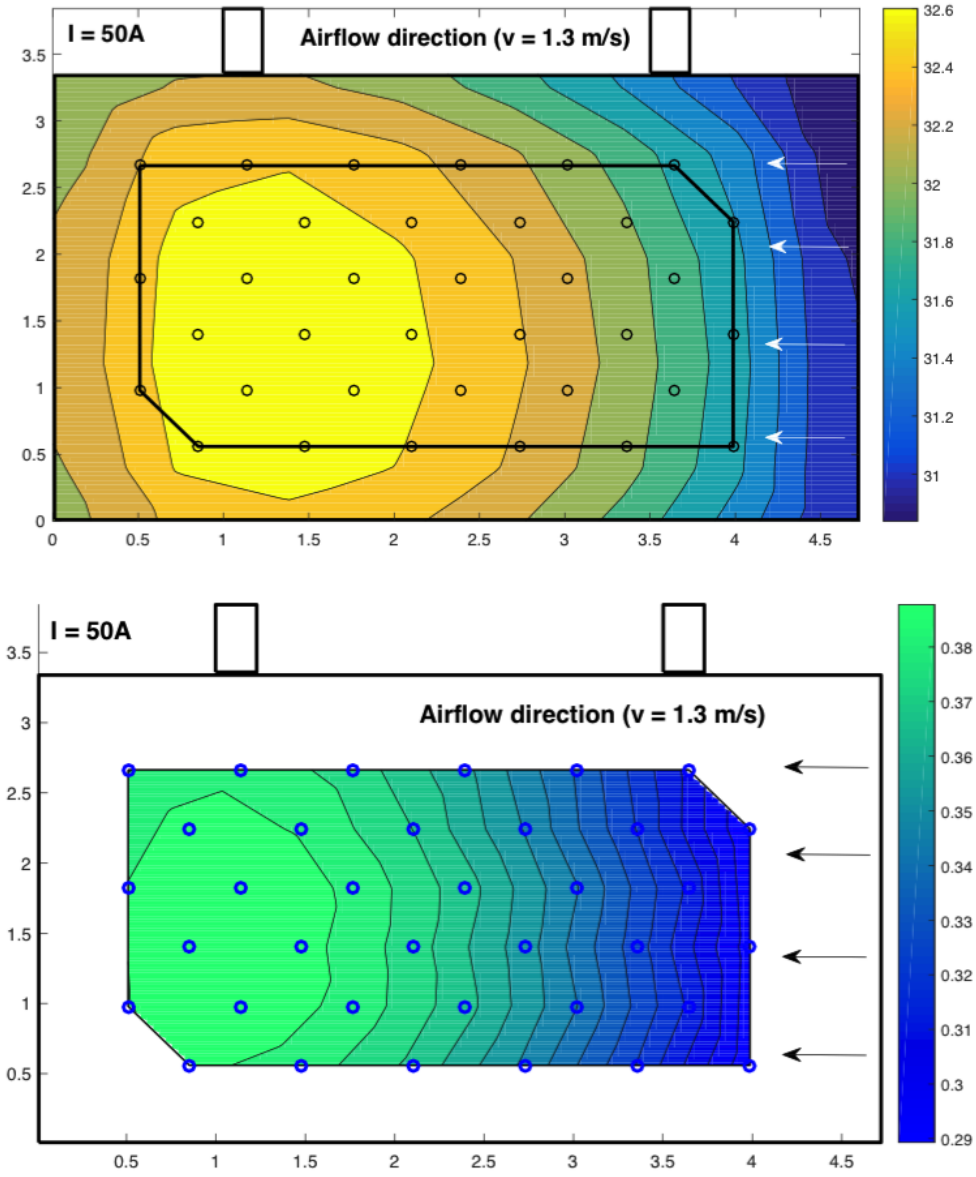

Figure 3.9: Simulated surface temperature distribution (°C) and the resulting observability metric γ for an airflow velocity of $v = 1.3$ m/s and charge sustaining current amplitude of 50 A.

3.4.3.2 Varying current amplitude

It has been shown in Section 3.4.3.1 that the sensor location for best observability coincides with the location of the hottest spot on the surface of the cell. This section investigates whether the collocation of the hot spot and the location of the sensor for best observabil-

ity is affected by the current amplitude. Three different current amplitudes of 50, 39, and 20 A are used in a charge sustaining pulsing profile to analyze the observability with a constant inlet airflow velocity of $v = 0.65$ m/s. The observability metric γ is quantified using the eigenmode projections method presented in Section 3.3. The results in Figures 3.10 through 3.12 show that regardless of the current amplitude, the observability results remain unchanged. Thus the best observability spot is only affected by the location of the hot spot on the surface of cell and not by the magnitude of the temperature of this hot spot.

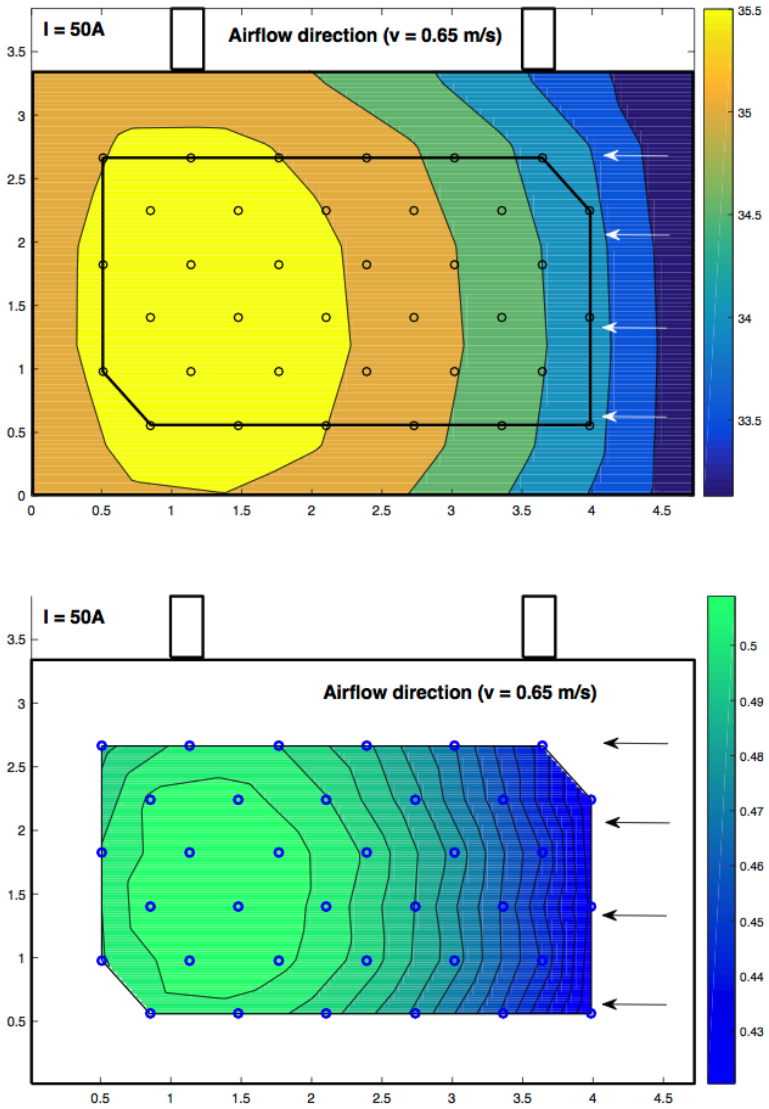

Figure 3.10: Surface temperature profiles and observability result using a 50 A charge sustaining profile and an inlet flow velocity of $v = 0.65$ m/s.

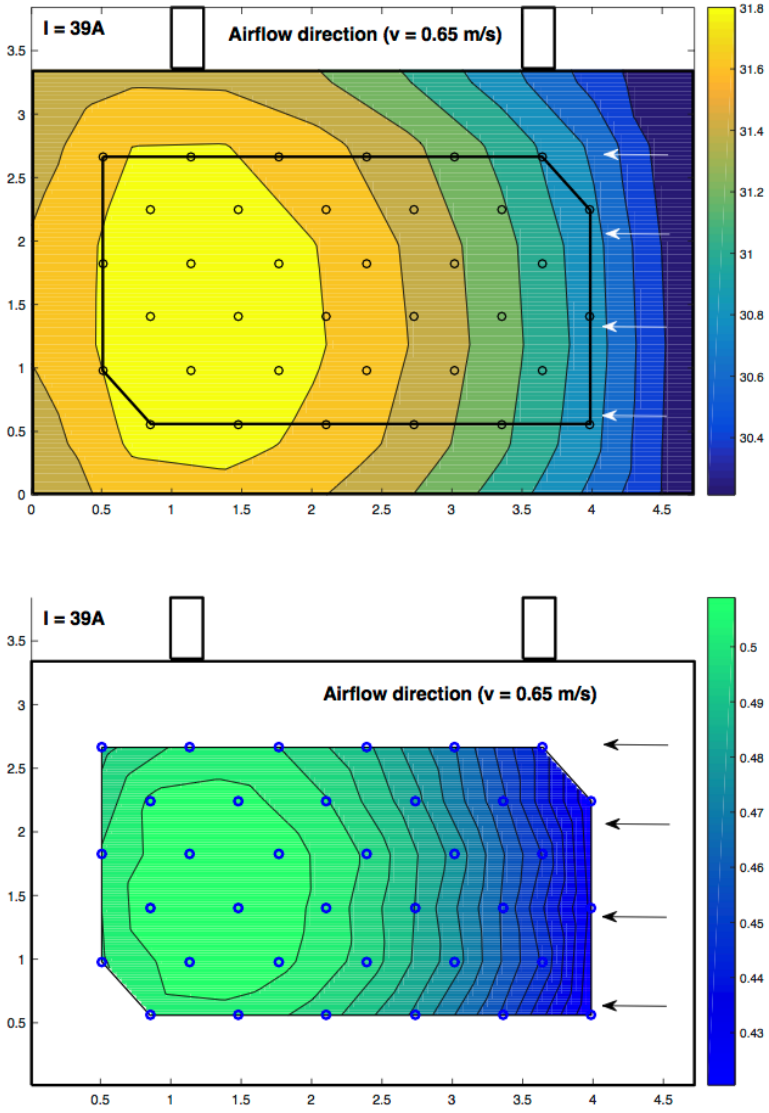

Figure 3.11: Surface temperature profiles and observability result using a 39 A charge sustaining profile and an inlet flow velocity of $v = 0.65$ m/s.

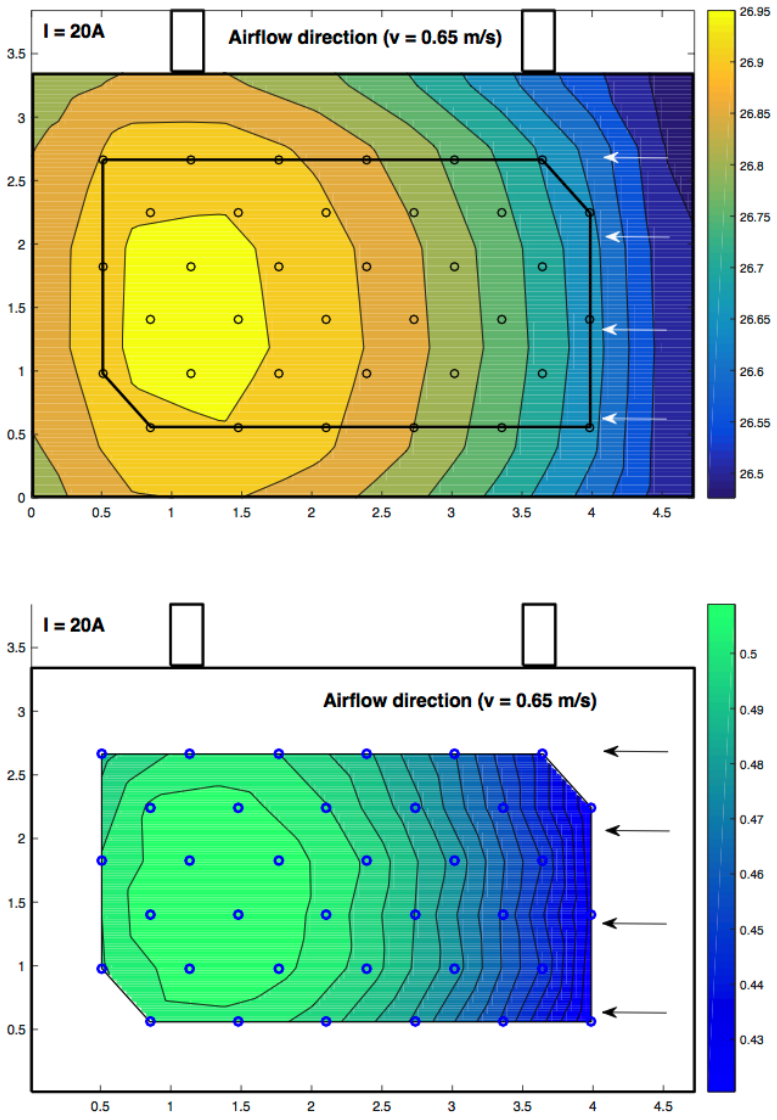

Figure 3.12: Surface temperature profiles and observability result using a 20 A charge sustaining profile and an inlet flow velocity of $v = 0.65$ m/s.

3.4.4 Temperature convergence

To show the practicality of a surface sensor versus a tab sensor, a closed loop estimation scheme can be setup for estimating the core temperature of the cell using the optimum sensor placement results of the eigenmode projection method. The closed loop scheme is based on a Kalman filter [68] in a discrete time domain. Given the thermal system described in Eqs. 2.5 through 2.9, one can formulate the system in discrete time domain as given by

the following equations:

$$x(k+1) = A_d x(k) + B_d u(k) + w(k), \tag{3.13}$$

$$y(k) = Cx(k) + v(k), \tag{3.14}$$

where $x(k)$ is a vector of all the temperature states, and $y(k)$ is the observed or measured temperature (for example, the tab sensor). $w(k)$ and $v(k)$ are the process and measurement noise respectively. For the above system, the discrete Kalman filter equations can be formulated as:

- At the measurement time (measurement update)

$$\hat{x}(k) = \bar{x}(k) + P(k)C^T R^{-1}(y(k) - C\bar{x}(k)), \tag{3.15}$$

  where

$$P(k) = M(k) - M(k)C^T(CM(k)C^T + R)^{-1}CM(k). \tag{3.16}$$

- Between measurements (time update)

$$\bar{x}(k+1) = A_d\hat{x}(k) + B_d u(k), \tag{3.17}$$

  and

$$M(k+1) = A_d P(k) A_d^T + Q, \tag{3.18}$$

where $Q = \varepsilon\{w(k)w^T(k)\}$ and $R = \varepsilon\{v(k)v^T(k)\}$.

Since in an actual battery, the interior temperature cannot be measured, a closed loop simulation is performed with the Kalman filter outlined above to show the convergence of the interior temperature of the cell under wrong initial conditions and given 3 different surface measurements (tab sensor, 3 sensors on surface, and 1 sensor on surface). Simulation shows that using one or three sensors on the surface of the cell can achieve much faster interior temperature estimation than the tab sensor. Figure 3.13 shows that at time t=8000 sec, the temperature states of the battery are initialized to the surface temperature during a US06 cycle. The figure shows that using the one or three sensors on the surface, the interior temperature converges in 180 sec to the actual interior temperature as compared to 330 sec when using the tab sensor. Notice also that the temperature converges faster with the 3 surface sensors than the 1 surface sensor, but overshoots more than using the 1 surface sensor.

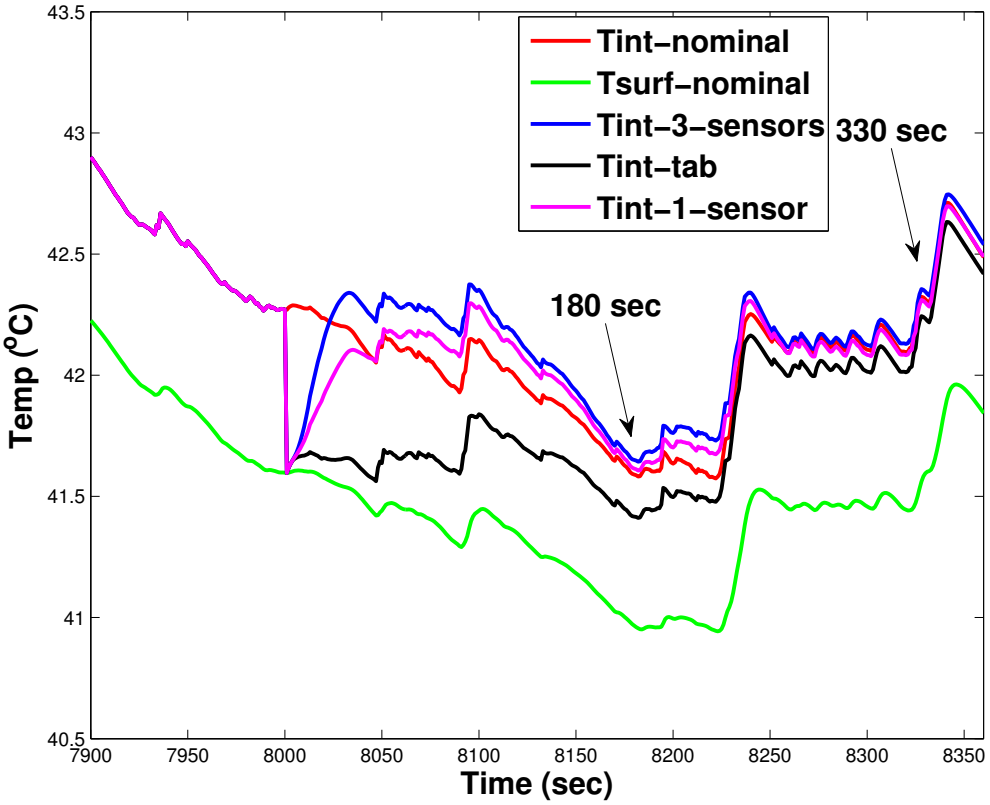

Figure 3.13: Core temperature estimation using a three sensor array (GE) on the surface versus a tab sensor (tab)

3.5 Conclusions

Two methods for looking at the observability of a thermal model for a battery cell using novel thin RTD temperature sensors have been analyzed. Results show that sensors placed over the surface of the battery provide better observability as compared to a conventional sensor placed on top of the battery (near the tabs in the Ford C-max 2013 pack). The analysis is done by looking at the trace of the observability gramian matrix and at the projection of the eigenmodes of the system matrix onto the observability subspace. A 15.79/18.12% improvement (trace method / eigenmode projection method) could be achieved if one sensor is placed at the optimal location on the surface of the battery as compared to a sensor placed on top of the battery. 241/252% improvement (trace method / eigenmode projection method) improvement could be achieved if 3 sensors are used. Simulations show that the

estimate of the core temperature of the cell converges in 180 sec using the sensors on the surface versus 330 seconds when using a tab sensor. Results indicate that maximum observability could be achieved by placing the sensors at the location of the hot spot. As the hot spot shifts around due to different airflow velocities, the location of best observability follows the hot spot location. Finally, it is shown that the current amplitude does not have any effect on the location of best observability.

Based on an accurate cell model and an optimal temperature sensor placement location, a full pack model can be devised that can exploit the accuracy and benefit of such models and sensors. In the next chapter, opportunities to downsize a battery pack using a pack model and a power limiting algorithm is looked at to potentially reduce pack costs.

CHAPTER 4

Downsizing battery packs

4.1 Introduction

Hybrid Electric Vehicle (HEV) manufacturers seek to reduce the weight and cost of their vehicles to gain competitive advantage. Mainly, this goal could be achieved by reducing the weight and/or size of powertrain - especially, an engine and a battery pack in an HEV. Studies on the downsizing and its effects including cost and fuel consumption have been addressed in literature [69, 70, 71, 72, 73]. In this chapter, the emphasis on downsizing is shifted from the engine to the battery assuming a fixed engine size and vehicle power management strategy. It is a typical approach that, in optimization or parametric studies, the power limit (or power capability) of a battery can be computed based on PNGV Hybrid Pulse Power Characterization (HPPC) method[1]. However, the PNGV method has two issues. Since the internal resistance is parameterized typically using a 10 sec pulse, the computed power limit is usually lower than actual power limit. Also, the PNGV method does not consider many operational battery constraints. Much effort has been documented in [41, 44, 74, 75, 76] to accurately compute the power capability of batteries in real-time, while considering the electrical, electrochemical, and thermal constraints such as terminal voltage, battery SOC, Li-ion concentration, and temperature. A model-based power limiting strategy based on the work in [76] is used to calculate the power limits of the battery when downsizing and changing nominal operating SOC. This method allows for higher power operation of the battery as compared to the PNGV method without compromising safety.

The 2nd generation Li-ion powered HEVs have been designed [77, 78] and are about to appear in the market. Motivated by cost reduction, the inherent safety of a model-based power limiting algorithm allows for a less conservative pack design and ultimately fewer or smaller cells. The influence on the battery performance (e.g., utilization, temperature,

[1]The PNGV HPPC method, developed by Idaho National Engineering and Environmental Laboratory, computes the instantaneous pulse power capability of a battery using an internal resistance, its open-circuit voltage, and predetermined current/voltage limits

life and cost) associated with pack downsizing and with operating SOC window, however, needs to be thoroughly studied. Battery downsizing will increase each cell's energy throughput and the root mean square (RMS) current, generating more heat and triggering potentially more often the operational voltage limits. More importantly, the battery power limits, or charge/discharge power capabilities depend on the nominal SOC operating window. In most commercial HEVs' the nominal SOC operation is centered around 50% or higher which allows for more discharge and thus higher power capabilities and battery efficiencies [79]. Using dynamic models and a predictive battery management technique, this chapter provides a case study on battery downsizing along with the selection of SOC operating window for an existing light-duty vehicle, and demonstrates the cost benefit attributed with that downsizing.

To quantitatively study the performance of a battery, it is essential to have accurate representation of the internal dynamics of the battery, i.e., electrical/thermal behavior and capacity fading. To that end, an equivalent-circuit model, a lumped thermal capacitance model based on [31], and a semi-empirical capacity fade model [80] are adopted in this work to capture terminal voltage, battery state-of-charge (SOC), temperature, and capacity loss, respectively. In particular, the capacity fading model is parameterized using a novel set of experiments that highlight the influence of nominal operating SOC on degradation as shown in Fig. 4.1. The model in [80] was parameterized for a plug-in hybrid electric vehicle (PHEV) for SOCs between 25% and 45%. The results show an significant increase in capacity fade with increasing SOC, which, if extrapolated to higher SOCs, could lead to errors for the higher SOCs. The experiments in this chapter extend the SOC range to 65% which is more important for an HEV application.

In cost analysis, Argonne National Laboratory's Battery Performance and Cost (BatPaC) model is used. The BatPaC model provides cost estimates based on materials and cell/pack design and hence it has been used for cost analysis in literature [81, 82, 83, 84]. In investigating downsizing of a battery pack, an actual current profile from the battery pack equipped from a light duty vehicle HEV is used. The profile assumes a fixed engine and vehicle power management and is scaled as number of cells is changed to match the total power demanded or supplied.

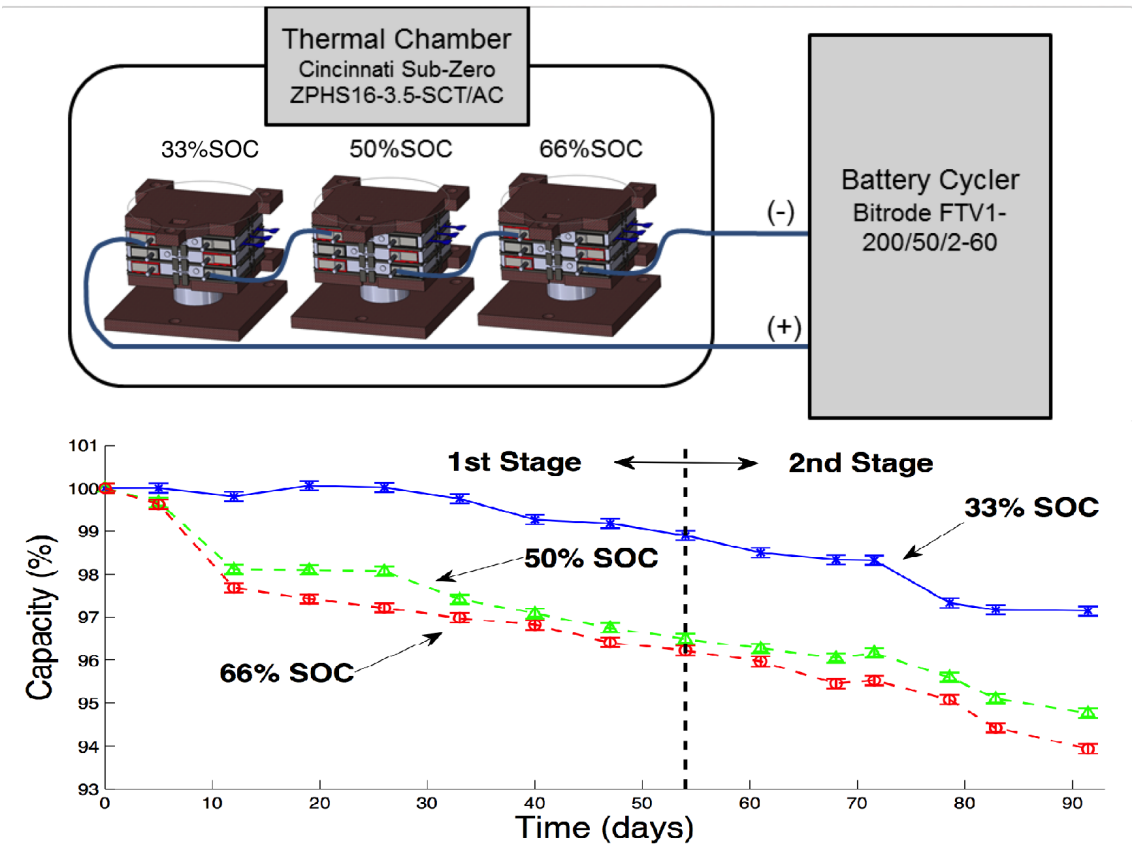

Figure 4.1: Setup and results of experimental capacity fade testing at different SOCs

The main contribution in this chapter is to identify opportunities to downsize a battery pack. This is done by reducing battery count, and shifting the center of nominal operating SOC window on the battery performance in an HEV application. The associated cost reduction due to the downsizing is calculated and the additional benefit of a faster warm up is shown, especially at low temperatures. The parametric study in this work shows that the battery pack under consideration can be scaled down from 76 to 64 cells without experiencing any discharge or charge power denials when nominal operating SOC is shifted from 50% to 35% at an ambient temperature of 25°C. Here we define a power denial as requested battery power greater than the limit set by the control algorithm. Also, each cell in the pack would experience a 19% increase in energy utilization with only a 0.5% capacity fade increase. Total cost of the battery pack could be decreased by 10%, and the cells experience a faster warmup which helps in reducing power denials, especially at low temperatures.

4.2 Pack electro-thermal model

A two state thermal, three state electrical model based on the model introduced in Chapter 2 is formulated. The cell electrical model can be represented by Eqs. 4.1 and 4.2.

$$\begin{bmatrix} \dot{V}_1 \\ \dot{V}_2 \\ \dot{z} \end{bmatrix} = \begin{bmatrix} -\frac{1}{R_1 C_1} & 0 & 0 \\ 0 & -\frac{1}{R_2 C_2} & 0 \\ 0 & 0 & 0 \end{bmatrix} \begin{bmatrix} V_1 \\ V_2 \\ z \end{bmatrix} + \begin{bmatrix} \frac{1}{C_1} \\ \frac{1}{C_2} \\ -\frac{1}{Q} \end{bmatrix} \begin{bmatrix} I, \end{bmatrix} \tag{4.1}$$

$$V_t = OCV - IR_s - V_1 - V_2. \tag{4.2}$$

The cell thermal model can be represented by Eqs. 4.3 and 4.4.

$$\dot{T}_{core} = \frac{1}{(\rho c V)_{core}} \left(\dot{Q} + \frac{KA}{L} \left(T_{surf} - T_{core} \right) \right), \tag{4.3}$$

$$\dot{T}_{surf} = \frac{1}{(\rho c V)_{surf}} \left(\frac{KA}{L} \left(T_{core} - T_{surf} \right) + hA \left(T_{amb} - T_{surf} \right) + Q_{cond} \right), \tag{4.4}$$

where Q_{cond} is the heat conduction between two consecutive cells. $\dot{Q}$ is the heat generation from the electrical model. $K = K_{xy} = 22\ W/m^2K$ from Table 2.1, $(\rho c)_{core} = 2.75e6\ J/m^3K$ and $(\rho c)_{surf} = 2.42e6\ J/m^3K$ are the corresponding parameters from Table 2.1, A is the surface area of the cell, and L is half of the width of the cell. The heat transfer coefficient, h, is a function of the airflow velocity between the cells. To be able to identify h, the pack model was modeled using a finite element model that represents the exact structure of the pack. Figure 4.2 shows a detailed structure of the pack with the inlet and outlet air ducts and the corresponding flow rates between the cells in the front and rear packs. The airflow paths are represented in red.

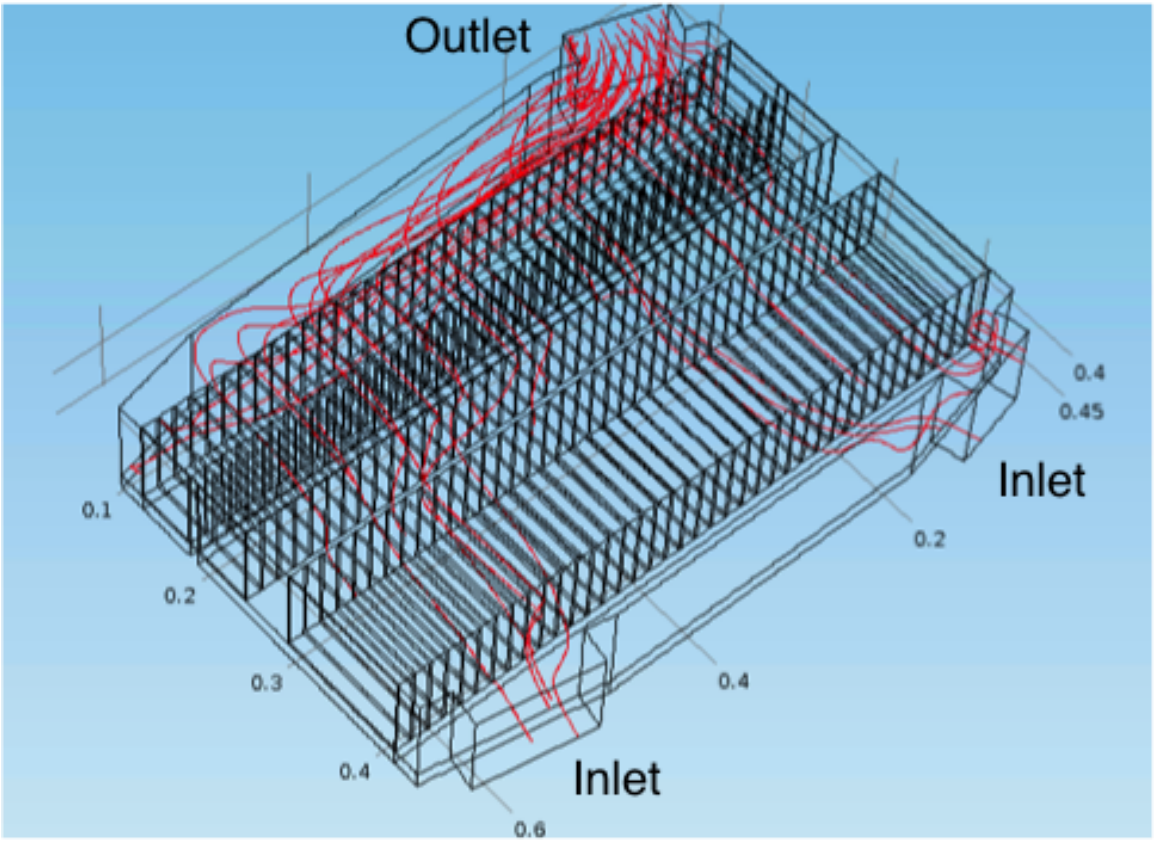

Figure 4.2: Airflow across the front and rear pack represented in red lines

Given the flow rate ranges experienced by the pack, the flow field between the cells is considered laminar. As such, the following equations for calculating the heat transfer coefficient given a laminar flow [55] can be used:

$$Re = \frac{\rho v H}{\mu}, \tag{4.5}$$

$$Pr = \frac{\nu}{\alpha}, \tag{4.6}$$

$$Nu = 0.664 Re^{\frac{1}{2}} Pr^{\frac{1}{3}}, \tag{4.7}$$

$$h = \frac{Nuk}{H}, \tag{4.8}$$

where v is the velocity of the air between two consecutive cells. Re, Pr, and Nu are Reynolds, Prandtl and Nusselt numbers respectively. ρ, μ, ν, α and k are the density, dynamic viscosity, kinematic viscosity, thermal diffusivity, and thermal conductivity of air. H is the characteristic dimension. For flow between two parallel plates, H is twice the

distance between the plates [85].

The heat conduction Q_{cond} in Eq. 4.4 is due to the tabbing connecting the cells in series. This can be represented as:

$$Q_{cond} = \beta_{cond} \left(T_{surf,i} - T_{surf,i+1} \right) \tag{4.9}$$

where β_{cond} is a tunable conduction parameter, and $T_{surf,i}$ and $T_{surf,i+1}$ are the surface temperatures of two consecutive cells connected through tabbing.

Finally, due to the complex geometry of the pack, the finite element model was used to quantify the airflow distributions between the cells in the front and rear pack. Running the finite element model resulted in three different parameters, γ_{under}, $\gamma_{through}$ and γ_{mix} for airflow distributions. The configuration of the pack allows for air to go through and under the front pack facing the inlet ports of the airflow. The airflow that goes under and through the front pack then mixes and goes through the rear pack which is closer to the outlet. γ_{under} is a scalar value that defines the percentage of air that goes under the first pack. $\gamma_{through}$ is a vector that defines the percentage of air that goes through each of the spaces between the cells in the front pack. So given, any input mass flow rate, $\dot{m}_{input}$, the resulting distribution of mass flow rates through the spaces between the front pack cells, $\dot{m}_{front}$, can be identified as:

$$\dot{m}_{front} = \gamma_{through} \left((1 - \gamma_{under}) \, \dot{m}_{input} \right) . \tag{4.10}$$

The resulting $\gamma_{through}$ vector distribution is shown in Fig. 4.3, which shows that more air goes through the cells closer to the airflow inlets.

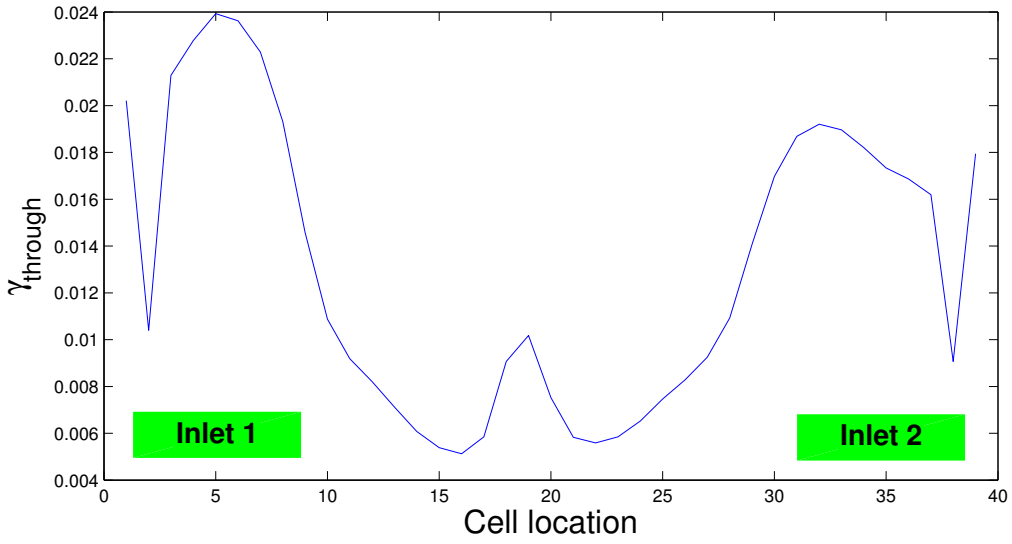

Figure 4.3: Scaled distribution of the airflow through the front pack.

The resulting velocity between the cells could thus be calculated as:

$$v_{front} = \frac{\dot{m}_{front}}{\rho_{air} A_{gap}}, \tag{4.11}$$

where ρ_{air} is the density of air and A_{gap} is the area of the gap between the cells. The identified velocity in Eq. 4.11 can be plugged back into Eq. 4.5 to find the resulting heat transfer coefficient h.

The parameter γ_{mix} is a matrix that defines how the airflow distributes in the spaces in the rear pack for each airflow through each of the cells in the front pack. For example, looking at Eq. 4.12, the first column shows that 78% of air goes from the first space in the front pack to the first space in the rear pack and 22% goes from the first space in the front pack to the second space in the rear pack.

$$\gamma_{mix} = \begin{bmatrix} 0.78 & 0 & ... & 0 & 0 \\ 0.22 & 0.87 & ... & 0 & 0 \\ 0 & 0.13 & ... & 0 & 0 \\ ... & ... & ... & 0.95 & 0 \\ 0 & 0 & ... & 0.05 & 1 \end{bmatrix} \tag{4.12}$$

Finally, for tuning the pack electro-thermal model, 3 different tuning factors should be accounted for:

1. The conduction factor, β_{cond} which accounts for the heat conduction between con-

secutive cells.

2. A factor, β_{shift}, which accounts for the amount of airflow that goes under versus through the first pack. Although a separate analysis was performed using a finite element model to calculate the amount of air that goes under the first pack versus through it, the actual airflow distribution in the pack could be different because the geometry is more complex and could not be captured using the finite element model. The β_{shift} factor subtracts and adds the γ_{under} and $\gamma_{through}$ factors respectively.

3. A factor, $\beta_{convection}$, which divides the heat transfer coefficient such that $h_{corrected} = \frac{h}{\beta_{convection}}$. In the scenario where the pack is instrumented with extra sensors, the resulting flow rate due to the increased pressure drop because of the added restrictions would skew the corresponding airflow rate calculations. This is why the $\beta_{convection}$ factor is needed.

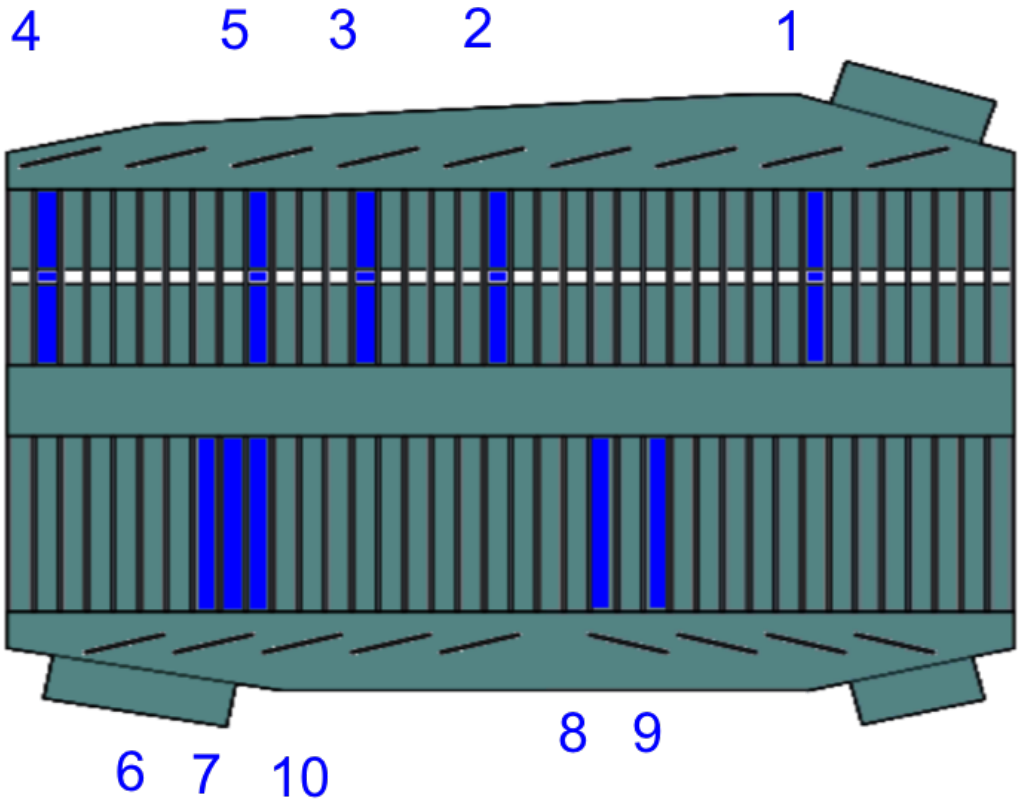

Figure 4.4: Location of sensors (marked in blue) in the pack.

Given the pack sensor configuration shown in Fig. 4.4 shown in blue, different duty

cycles were used to parameterize and validate the pack electro-thermal model. The drive cycle shown in Fig. 4.5 was used for tuning and parameterizing the pack electro-thermal model. Parameterization was done using least squares method where the objective function to be minimized is:

$$J = \sum_{n=1}^{10} \sqrt{\sum_{t=0}^{t_{end}} (\bar{T}_n(t) - T_n(t))^2}, \tag{4.13}$$

where $\bar{T}_n(t)$ and $T_n(t)$ are the measured and simulated temperatures respectively at the sensor locations shown in Fig. 4.4 at time t.

The results of the pack modeling are shown in Figs. 4.5 through 4.12. Note that across the sensor locations, the maximum error between the measured and simulated temperatures is less than 3°C. The different drive cycles have different flow rates, ambient temperatures and current profiles.

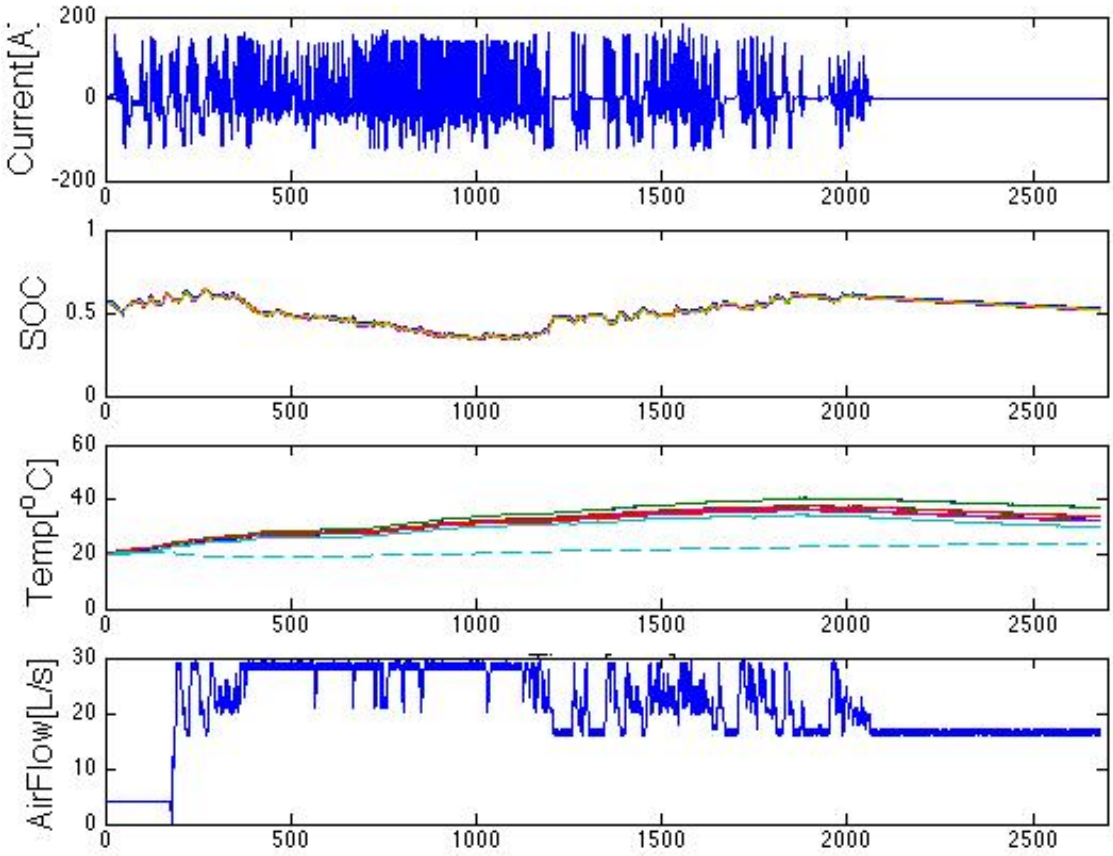

Figure 4.5: Drive 24 profile used for tuning the model.

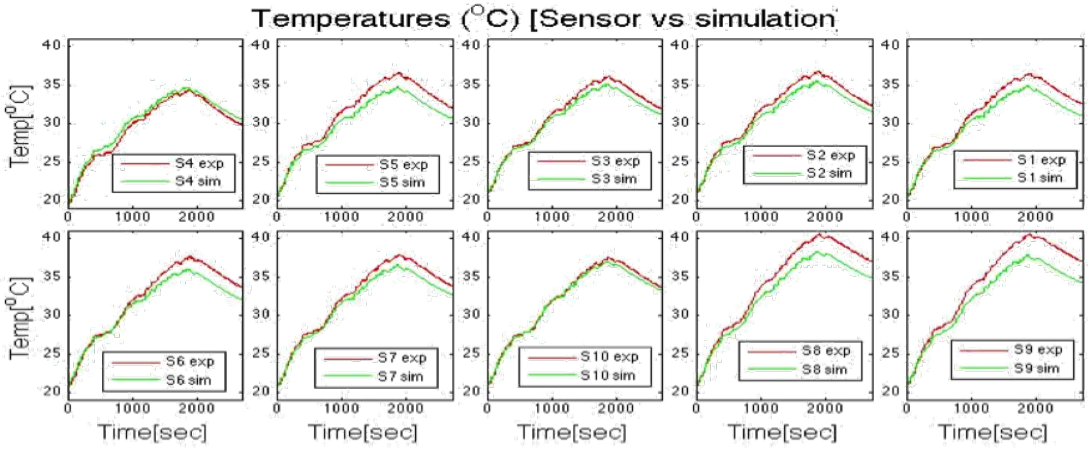

Figure 4.6: Drive 24 temperature simulation results

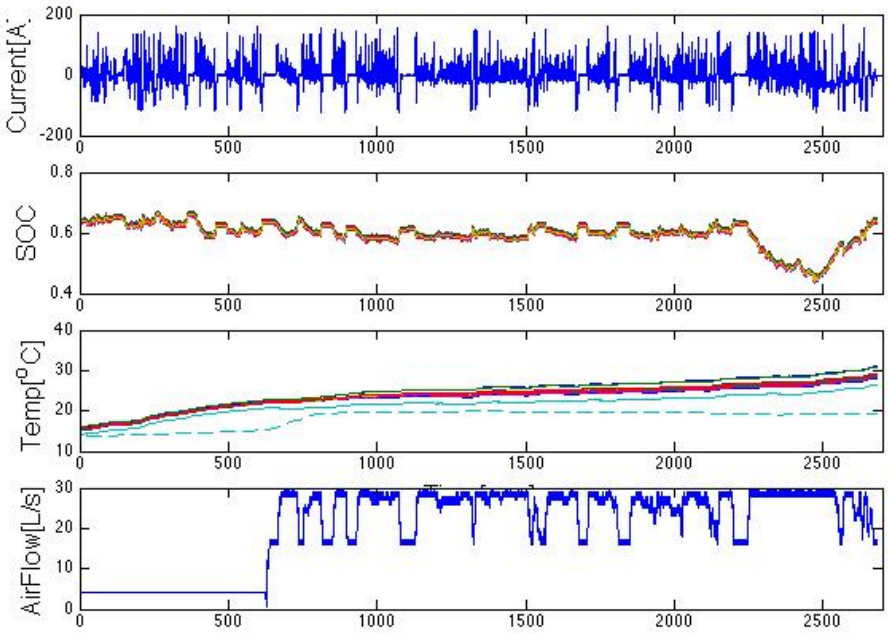

Figure 4.7: Drive 97 profile used for validating the model.

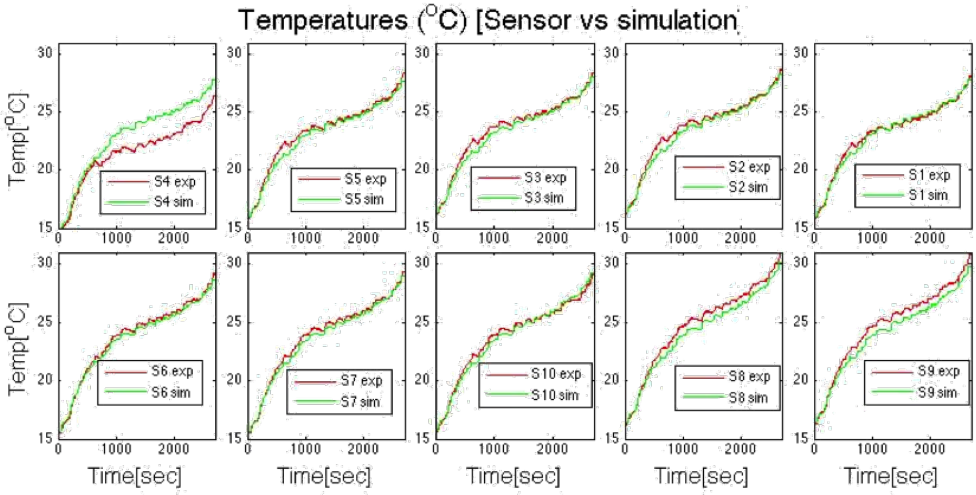

Figure 4.8: Drive 97 profile temperature simulation results

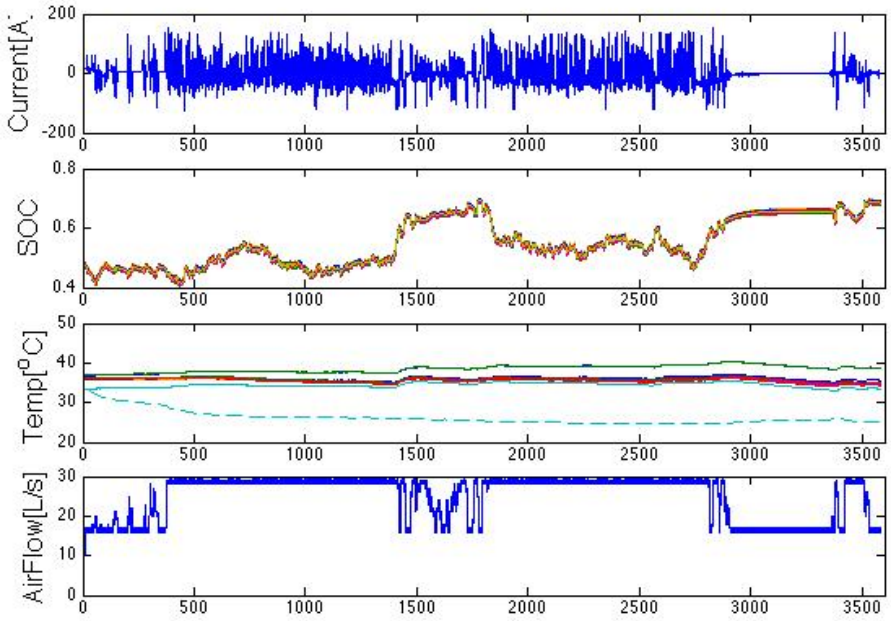

Figure 4.9: Drive 111 profile used for validating the model.

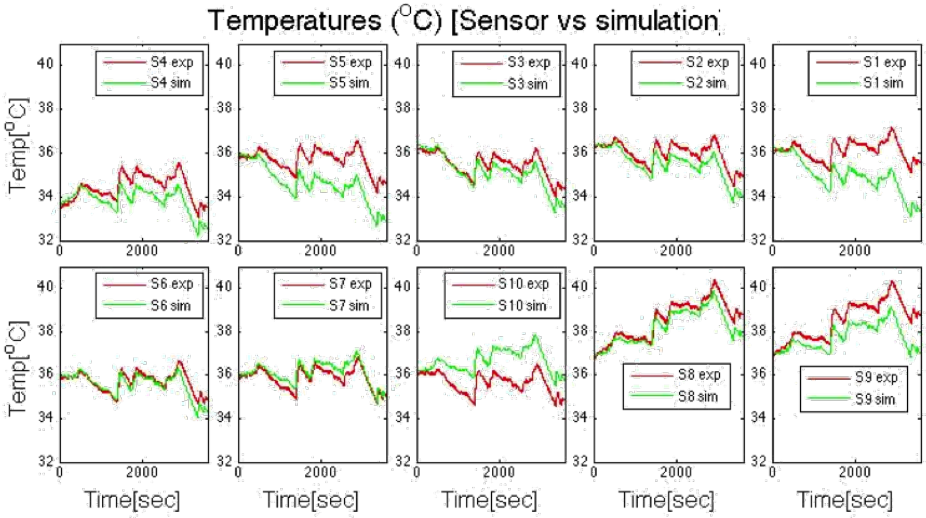

Figure 4.10: Drive 111 profile temperature simulation results.

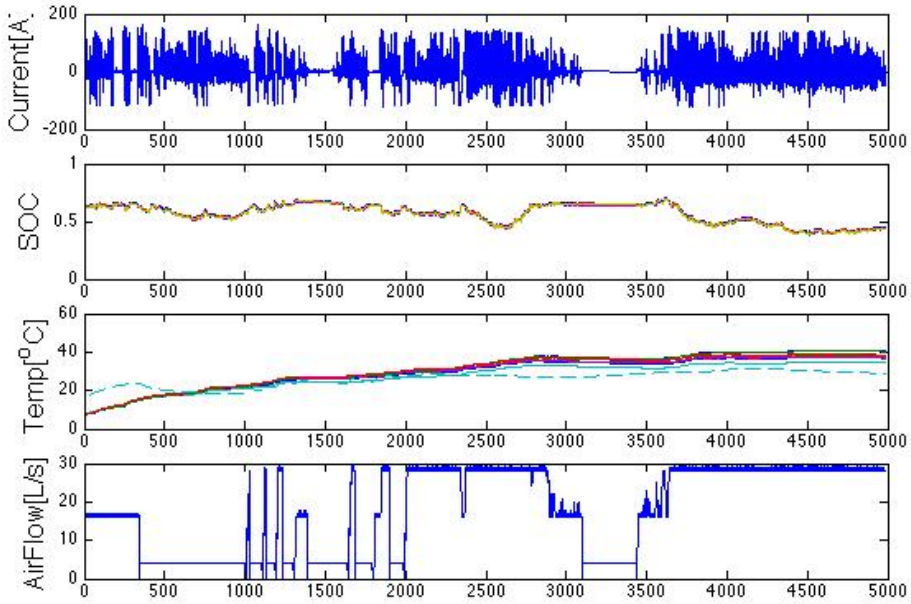

Figure 4.11: Drive 16 profile used for validating the model.

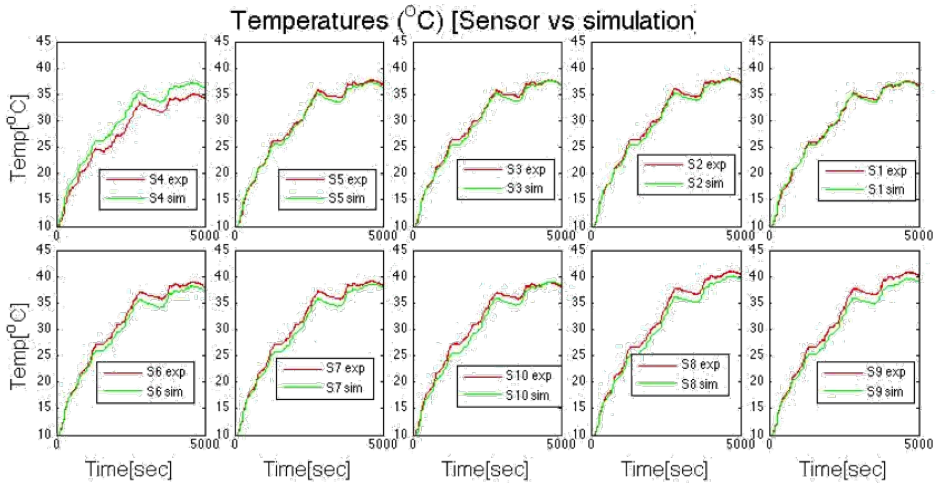

Figure 4.12: Drive 16 profile temperature simulation results.

4.3 Optimal temperature sensor placement

Many different optimal sensor placement techniques have been studied in literature. The majority have been formulated around the observability (O_b) and observability gramian

(W_o) matrices. Scalar metrics such as the trace, the condition number, the smallest eigenvalue and the determinant of the observability gramian matrix have been used [61, 86, 87, 88]. In this section, two different methods are used to study the issue of optimal sensor placement in the pack. The first is based on maximizing the rank of the observability matrix, while the second is based on the work in [89] which looks at the trace of the observability gramian matrix.

The observability matrix is defined as:

$$O_b = \begin{bmatrix} C \\ CA \\ \vdots \\ CA^{n-1} \end{bmatrix}, \tag{4.14}$$

where A is the system matrix, and C is a matrix defining the locations of the sensors. A system is thus fully observable if and only if the O_b is full rank [90]. The observability gramian matrix is defined in Eq. 3.6.

The original pack design has 10 sensors distributed throughout the pack (refer Fig. 4.4). Thus in the analysis process, 10 sensors are permuted across the pack and the results are analyzed using the methods proposed above. However, given the limited number of sensors to be placed in the pack with 76 cells, the following observations can be made:

1. Given any permutation of the sensors, the system remains unobservable.

2. The problem thus becomes one of maximizing the rank of the observability matrix (O_b) or maximizing the trace of the observability gramian matrix (W_o).

3. Given that there are 76 cells and 10 sensors in the pack, the possible number of sensor combinations is:
$$C(76, 10) = \frac{76!}{10!(76-10)!} = 9.5 \times 10^{11} \tag{4.15}$$

4. To avoid this large computational burden, the pack is divided into 10 sections and only 1 sensor is permuted in each section. This also meant that, for example, the cases where all 10 sensors are placed next to each other are avoided.

The results of the optimal sensor placement are shown in Fig. 4.13. The figure shows 4 pack layouts with different sensor arrangements. The grey circles in all 4 arrangements show the existing RTD thin film sensor locations in the pack. The upper left arrangement shows the current sensor arrangement (blue) using the existing sensors (Ford sensors). The

upper right arrangement shows the optimal sensor placement (red) using the rank of the observability matrix when the sensors are constrained to move only between the existing RTD sensor locations. The lower left arrangement shows the optimal sensor placement (pink) using the trace of the observability gramian matrix when the sensors are free to move across the pack, and the lower right arrangement shows the optimal sensor placement (green) using the rank of the observability matrix when the sensors are also free to move across the pack. It should be noted that, using the rank of the observability matrix, several combinations could lead to the maximum rank but only one of those combinations are plotted in Fig. 4.13.

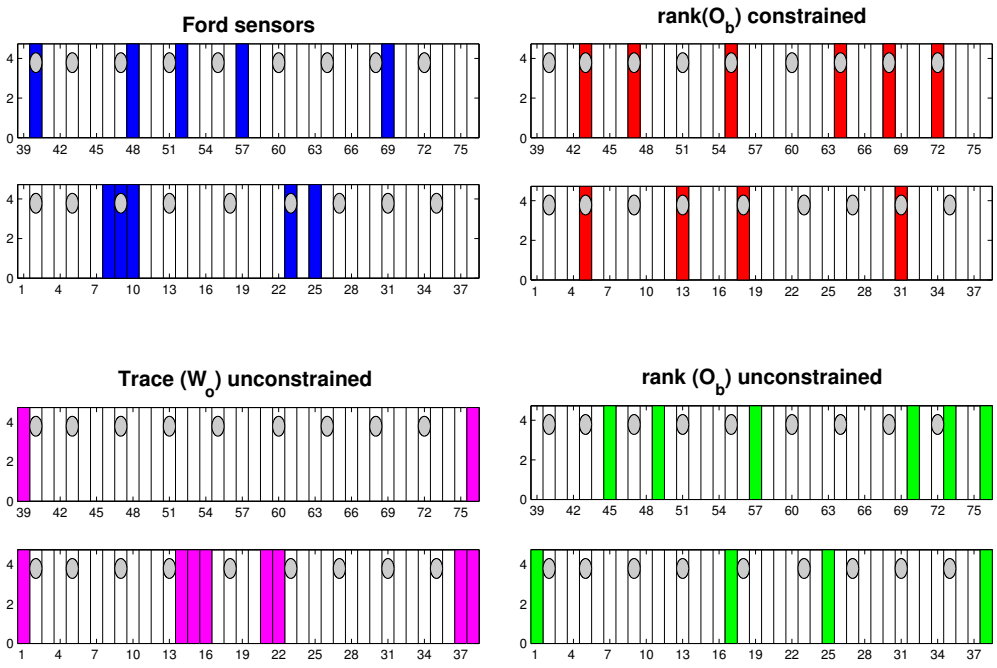

Figure 4.13: Results of the optimal sensor placement in the pack.

To look at the optimality of the locations identified in Fig. 4.13, 4 different simulations using the cycles from Figs. 4.5 through 4.12 were used with wrong temperature initial conditions with a closed loop model for temperature estimation. This closed loop model is discussed in section 4.4. The root mean square (RMS) on the temperature difference between the wrong and correct simulated temperatures is plotted in Figs. 4.14 through 4.17 along with the maximum error at any given cell in the pack at different time instants.

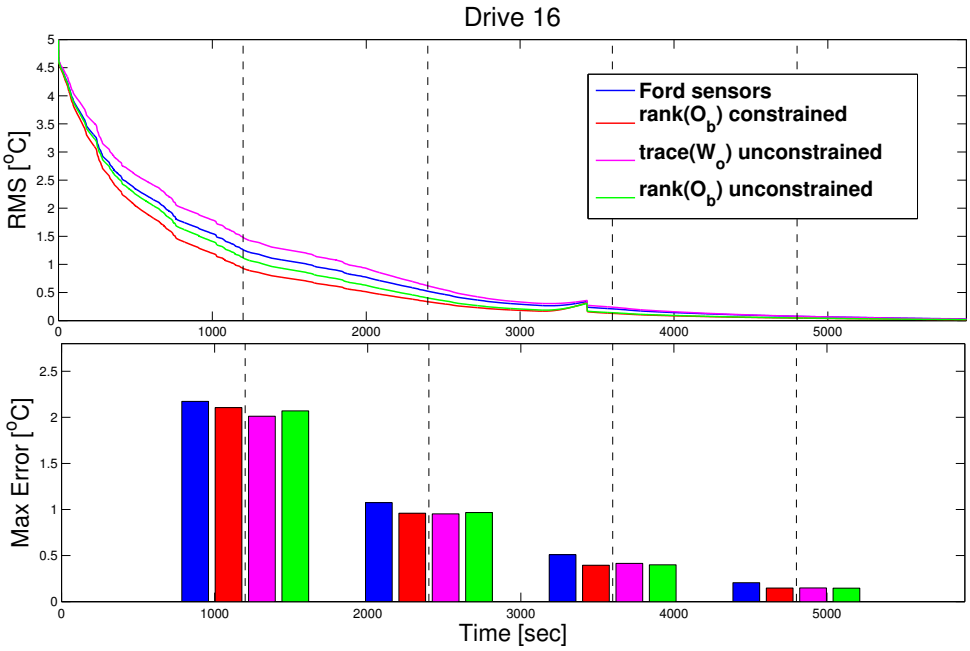

Figure 4.14: RMS and maximum error on the convergence of temperature using drive 16 cycle.

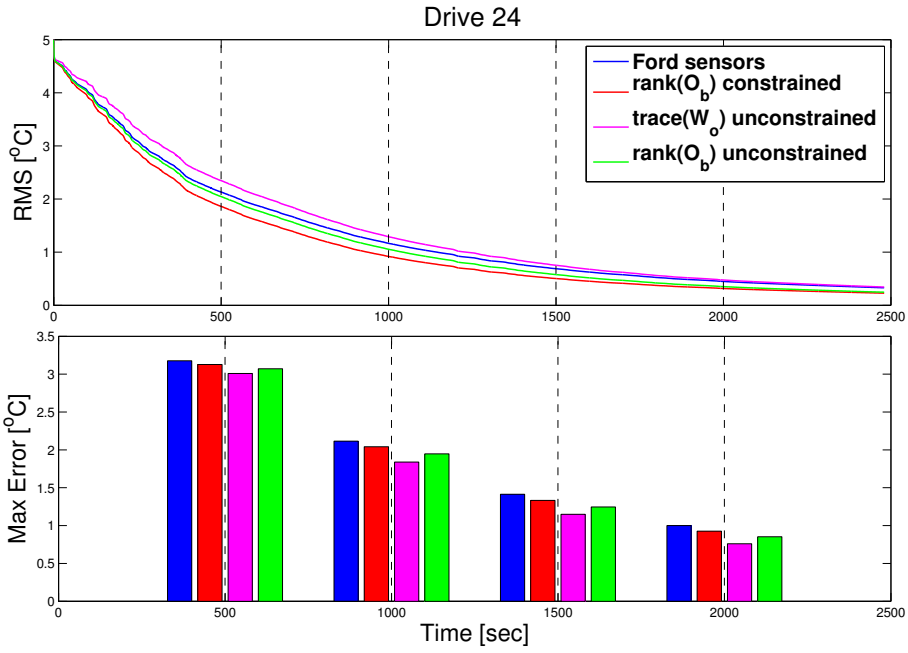

Figure 4.15: RMS and maximum error on the convergence of temperature using drive 24 cycle.

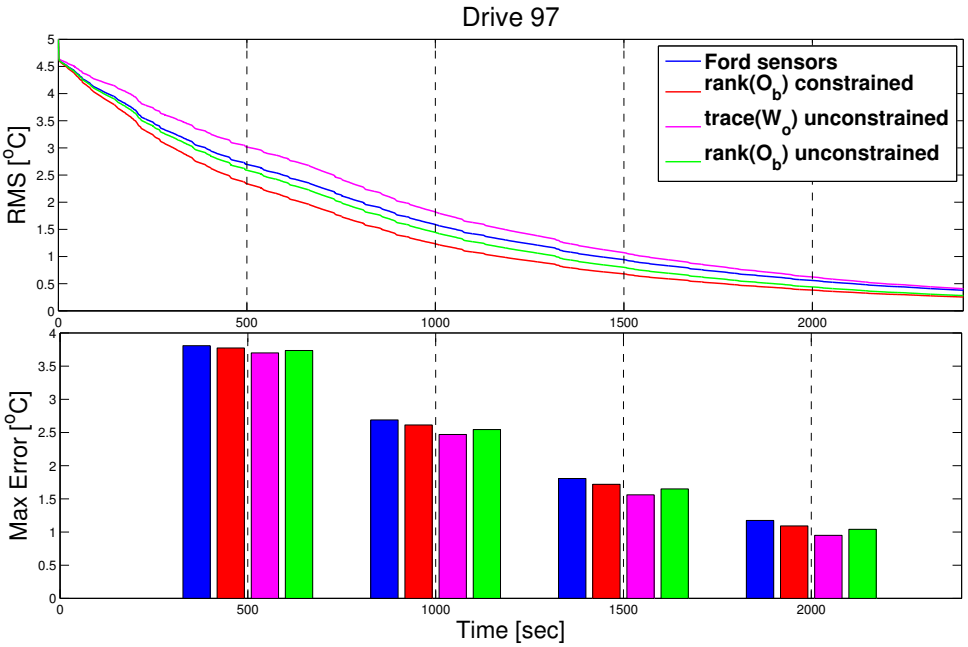

Figure 4.16: RMS and maximum error on the convergence of temperature using drive 97 cycle.

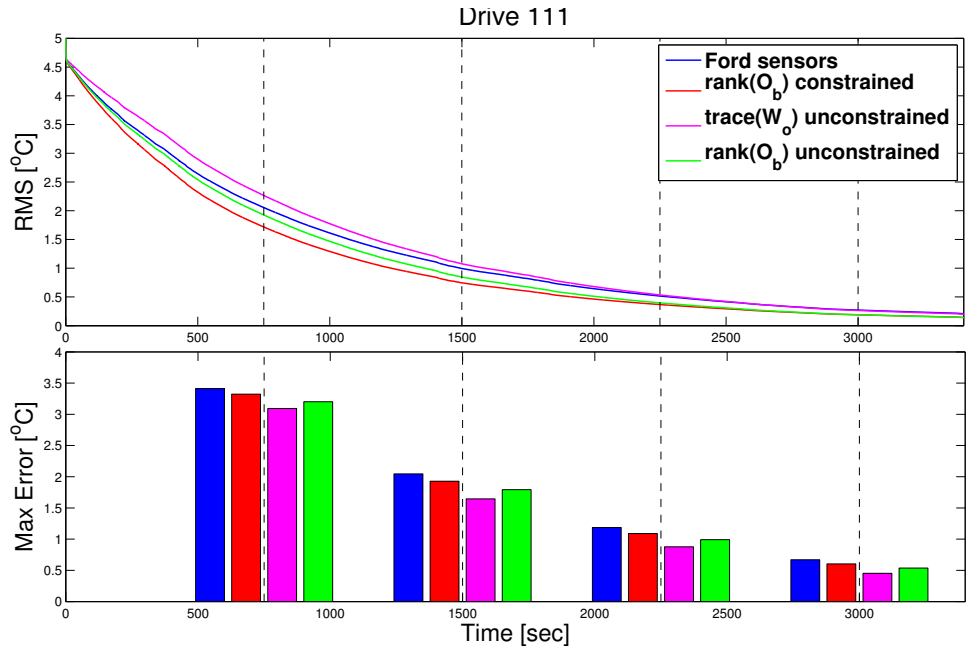

Figure 4.17: RMS and maximum error on the convergence of temperature using drive 111 cycle.

Results show that the sensor configuration identified using the rank of the observability matrix (second arrangement of Fig. 4.13) has the fastest convergence rate. However, the maximum error on the temperature is not smallest. This configuration of sensors is used in the closed loop formulation of the pack electro-thermal model. This is discussed in section 4.4 below.

4.4 Closed loop pack model

The pack electro-thermal model takes the form of a closed loop electrical and closed loop thermal model. A closed loop electrical model is needed mainly for state of charge estimation. On the other hand, given that there are limited number of temperature sensors in the pack, the closed loop thermal model is needed to estimate the unknown temperatures of the un-instrumented batteries.

Several different methods have been used for state of charge estimation in literature. The most basic is calculating SOC using coulomb counting [91, 92]. However this method is prone to errors in estimation due to inaccurate current measurements [93]. More advanced methods used artificial networks [94]. These methods are not very suitable for online estimation as they need training data for fitting their parameters. One of the most common estimation methods are those that rely on observers, like the Luenberger observer [95], or Kalman filters [96, 97, 98]. The main disadvantage of using Kalman filters is that they need large computing capacities and suitable or accurate battery models. Since the cell and pack battery models developed in sections 4.2 and 2.2 are shown to be sufficiently accurate, an extended Kalman filter is used for SOC estimation. The large computational burden is avoided by employing a gain scheduling technique.

The electrical state equations representing the ith cell in the pack are:

$$\begin{bmatrix} \dot{V}_{1,i} \\ \dot{V}_{2,i} \\ \dot{z}_i \end{bmatrix} = \begin{bmatrix} -\frac{1}{R_{1,i}C_{1,i}} & 0 & 0 \\ 0 & -\frac{1}{R_{2,i}C_{2,i}} & 0 \\ 0 & 0 & 0 \end{bmatrix} \begin{bmatrix} V_{1,i} \\ V_{2,i} \\ z_i \end{bmatrix} + \begin{bmatrix} \frac{1}{C_{1,i}} \\ \frac{1}{C_{2,i}} \\ -\frac{1}{Q_i} \end{bmatrix} \begin{bmatrix} I \end{bmatrix}, \tag{4.16}$$

where Q_i and z_i are the nominal capacity and state of charge of the ith cell respectively. $V_{1,i}$ and $V_{2,i}$ are the voltages across the double RC pair and I is the current through the pack. The output equation is:

$$V_{t,i} = V_{OCV,i} - V_{1,i} - V_{2,i} - IR_{s,i}. \tag{4.17}$$

Putting all the equations for the 76 cells together and separating the $\dot{V}_1$ and $\dot{V}_2$ terms

from the $\dot{z}$ terms (for faster computation), we get the following:

$$\dot{Z} = A_z Z + B_z U_z, \tag{4.18}$$

$$\dot{V}_{RC} = A_{RC} V_{RC} + B_{RC} U_{RC}, \tag{4.19}$$

$$V_T = H_z Z + H_v V_{RC} + R_s I + D, \tag{4.20}$$

where

$$Z_{(76\times1)} = \begin{bmatrix} z_1 \\ z_2 \\ \vdots \\ z_{76} \end{bmatrix} \qquad V_{RC(152\times1)} = \begin{bmatrix} V_{1,1} \\ V_{2,1} \\ \vdots \\ V_{76,1} \\ V_{1,2} \\ V_{2,2} \\ \vdots \\ V_{76,2} \end{bmatrix} \qquad V_{T(76\times1)} = \begin{bmatrix} V_{t,1} \\ V_{t,2} \\ \vdots \\ V_{t,76} \end{bmatrix}$$

$$A_{z(76\times76)} = \begin{bmatrix} 0 & 0 & \dots & 0 \\ 0 & 0 & \dots & 0 \\ \vdots & \vdots & \ddots & \vdots \\ 0 & 0 & \dots & 0 \end{bmatrix} \qquad B_{z(76\times1)} = \begin{bmatrix} -\frac{1}{Q_1} \\ -\frac{1}{Q_2} \\ \vdots \\ -\frac{1}{Q_{76}} \end{bmatrix} \qquad U_{z(1\times1)} = \begin{bmatrix} I \end{bmatrix}$$

$$A_{RC(152\times152)} = \begin{bmatrix} -\frac{1}{R_{1,1}C_{1,1}} & 0 & \dots & 0 & 0 & 0 & \dots & 0 \\ 0 & -\frac{1}{R_{1,2}C_{1,2}} & \dots & 0 & 0 & 0 & \dots & 0 \\ \vdots & \vdots & \ddots & \vdots & \vdots & \vdots & \ddots & \vdots \\ 0 & 0 & \dots & -\frac{1}{R_{1,76}C_{1,76}} & 0 & 0 & \dots & 0 \\ 0 & 0 & \dots & 0 & -\frac{1}{R_{2,1}C_{2,1}} & 0 & \dots & 0 \\ 0 & 0 & \dots & 0 & 0 & -\frac{1}{R_{2,2}C_{2,2}} & \dots & 0 \\ \vdots & \vdots & \ddots & \vdots & \vdots & \vdots & \ddots & \vdots \\ 0 & 0 & \dots & 0 & 0 & 0 & \dots & -\frac{1}{R_{2,76}C_{2,76}} \end{bmatrix}$$

$$B_{RC(152\times1)} = \begin{bmatrix} \frac{1}{C_{1,1}} \\ \frac{1}{C_{1,2}} \\ \vdots \\ \frac{1}{C_{1,76}} \\ \frac{1}{C_{2,1}} \\ \frac{1}{C_{2,2}} \\ \vdots \\ \frac{1}{C_{2,76}} \end{bmatrix} \qquad U_{RC(1\times1)} = \begin{bmatrix} I \end{bmatrix} \qquad H_{z(76\times76)} = \begin{bmatrix} \frac{\partial V_{OCV}}{\partial z_1} & 0 & \dots & 0 \\ 0 & \frac{\partial V_{OCV}}{\partial z_2} & \dots & 0 \\ \vdots & \vdots & \ddots & \vdots \\ 0 & 0 & \dots & \frac{\partial V_{OCV}}{\partial z_{76}} \end{bmatrix}$$

$$H_{RC(76\times152)} = \begin{bmatrix} -1 & 0 & \dots & 0 & -1 & 0 & \dots & 0 \\ 0 & -1 & \dots & 0 & 0 & -1 & \dots & 0 \\ \vdots & \vdots & \ddots & \vdots & \vdots & \vdots & \ddots & \vdots \\ 0 & 0 & \dots & -1 & 0 & 0 & \dots & -1 \end{bmatrix} \qquad R_{s(76\times1)} = \begin{bmatrix} -R_{s,1} \\ -R_{s,2} \\ \vdots \\ -R_{s,76} \end{bmatrix}$$

$$D_{(76\times1)} = \begin{bmatrix} b_1 \\ b_2 \\ \vdots \\ b_{76} \end{bmatrix},$$

where the D matrix contains all the constants from the linearization of the V_{OCV} curve with respect to z.

Therefore, in implementing the Kalman filter equations, we get the following for SOC estimation:

$$\dot{Z} = A_z Z + B_z U_z + K_z(V_T - \hat{V}_T), \tag{4.21}$$

$$\dot{P}_z = A_z P_z + P_z A_z^T - K_z H_z P_z + Q_z, \tag{4.22}$$

$$K_z = P_z H_z^T R_z^{-1}, \tag{4.23}$$

However, since there are 76 cells and accordingly the matrices are large, which makes the code computationally expensive, $\dot{P}_z$ in Eq. 4.21 is reduced to $P_z = f(SOC)$. The function $f(SOC)$ is predetermined in offline simulations to calculate the optimal P_z at different SOCs. This reduces the computational burden significantly.

The same is done for the double RC voltages, where:

$$\dot{V_{RC}} = A_{RC}V_{RC} + B_{RC}U_{RC} + K_{RC}(V_T - \hat{V}_T), \tag{4.24}$$

$$P_{RC} = g(I), \tag{4.25}$$

$$K_{RC} = P_{RC}H_{RC}^T R_{RC}^{-1}, \tag{4.26}$$

where the function $g(I)$ is predetermined in offline simulations to compute the optimal P_{RC} at different applied currents.

The same could be done on the thermal side, where, for example for the front pack array, we have:

$$\dot{T} = A_T T + B_T U_T + K_T(\bar{T} - \hat{T}), \tag{4.27}$$

$$\dot{P}_T = A_T P_T + P_T A_T^T - K_T C_T P_T + Q_T, \tag{4.28}$$

$$K_T = P_T C_T^T R_T^{-1}, \tag{4.29}$$

where $\bar{T}$ and $\hat{T}$ are the simulated and measured temperatures at the sensor locations in the pack, and:

$$T_{(76\times1)} = \begin{bmatrix} T_{core,1} \\ T_{core,2} \\ \vdots \\ T_{core,38} \\ T_{surf,1} \\ T_{surf,2} \\ \vdots \\ T_{surf,38} \end{bmatrix} \qquad \hat{T}_{(5\times1)} = \begin{bmatrix} \hat{T}_{surf,1} \\ \hat{T}_{surf,2} \\ \vdots \\ \hat{T}_{surf,5} \end{bmatrix} \qquad \bar{T}_{(76\times1)} = \begin{bmatrix} \bar{T}_{surf,1} \\ \bar{T}_{surf,2} \\ \vdots \\ \bar{T}_{surf,5}. \end{bmatrix}$$

$T_{surf,i}$ and $T_{core,i}$ are the surface and core temperature of the ith cell in the pack respectively. Also matrices A_T, and B_T are shown below:

$$A_{T(76\times76)} = \begin{bmatrix} -\frac{KA}{L(\rho cV)_{core}} & 0 & \dots & 0 & \frac{KA}{L(\rho cV)_{core}} & 0 & 0 & \dots & 0 \\ 0 & -\frac{KA}{L(\rho cV)_{core}} & \dots & 0 & 0 & \frac{KA}{L(\rho cV)_{core}} & 0 & \dots & 0 \\ \vdots & \vdots & \ddots & \vdots & \vdots & \vdots & \vdots & \ddots & \vdots \\ 0 & 0 & \dots & -\frac{KA}{L(\rho cV)_{core}} & 0 & 0 & 0 & \dots & \frac{KA}{L(\rho cV)_{core}} \\ \frac{KA}{L(\rho cV)_{surf}} & 0 & \dots & 0 & -\frac{KA/L+(h_1+h_2)A+\beta_{cond}}{(\rho cV)_{surf}} & \frac{\beta_{cond}}{(\rho cV)_{surf}} & 0 & \dots & 0 \\ 0 & \frac{KA}{L(\rho cV)_{surf}} & \dots & 0 & \frac{\beta_{cond}}{L(\rho cV)_{surf}} & -\frac{KA/L+(h_2+h_3)A+\beta_{cond}}{(\rho cV)_{surf}} & \frac{\beta_{cond}}{L(\rho cV)_{surf}} & \dots & 0 \\ \vdots & \vdots & \ddots & \vdots & \vdots & \vdots & \vdots & \ddots & \vdots \\ 0 & 0 & \dots & \frac{KA}{L(\rho cV)_{surf}} & 0 & 0 & 0 & \dots & -\frac{KA/L+(h_{38}+h_{39})A+\beta_{cond}}{(\rho cV)_{surf}} \end{bmatrix}$$

$$B_{T(76\times77)} = \begin{bmatrix} \frac{1}{(\rho cV)_{core}} & 0 & \dots & 0 & 0 & 0 & 0 & \dots & \dots & 0 \\ 0 & \frac{1}{(\rho cV)_{core}} & \dots & 0 & 0 & 0 & 0 & \dots & \dots & 0 \\ \vdots & \vdots & \ddots & \vdots & \vdots & \vdots & \vdots & \dots & \ddots & 0 \\ 0 & 0 & \vdots & \frac{1}{(\rho cV)_{core}} & 0 & 0 & 0 & \dots & \dots & 0 \\ 0 & 0 & \dots & 0 & \frac{(h_1A)/2}{(\rho cV)_{surf}} & \frac{(h_2A)/2}{(\rho cV)_{surf}} & 0 & \dots & \dots & 0 \\ 0 & 0 & \dots & 0 & 0 & \frac{(h_2A)/2}{(\rho cV)_{surf}} & \frac{(h_3A)/2}{(\rho cV)_{surf}} & \dots & \dots & 0 \\ \vdots & \vdots & \ddots & \vdots & \vdots & \vdots & \vdots & \vdots & \ddots & \vdots \\ 0 & 0 & \dots & 0 & 0 & 0 & 0 & \dots & \frac{(h_{38}A)/2}{(\rho cV)_{surf}} & \frac{(h_{39}A)/2}{(\rho cV)_{surf}} \end{bmatrix}$$

And finally, the input matrix U_T is:

$$U_{T(77\times 1)} = \begin{bmatrix} \dot{Q}_1 \\ \dot{Q}_2 \\ \vdots \\ \dot{Q}_{38} \\ T_{air,1} \\ T_{air,2} \\ \vdots \\ T_{air,39} \end{bmatrix}$$

,

where $\dot{Q}_i$ is the heat generation in the ith cell, and $T_{air,j}$ is the temperature of the air passing through the gap between cells $i-1$ and i.

4.5 Degradation testing and modeling

To predict capacity fade of the battery, a semi-empirical model, which has been widely used in literature [99, 100, 80], is adopted. A capacity fade model uses a power law with Arrhenius relation in order to relate stress factors such as charge throughput (Ah) and temperature to capacity fade. In [80], nominal operating SOC is considered as another stress factor.

However, the model cannot be applied without modifications since the chemistries of the battery in this study are not the same. Therefore, the model is parameterized against experimental data. Experiments are performed using a continuous charge sustaining current profile obtained from a light duty vehicle HEV operating on a US06 cycle. Each of the three fixtures is operating at three different nominal SOCs[2]. Each fixture is composed of three cells connected in series. The experiments are performed in two stages. In the first stage, the nominal operating SOC of fixtures 1, 2 and 3 is set to 33%, 50% and 66% SOC respectively. The temperature of the battery at quasi steady state is regulated at 25°C and the ambient temperature is controlled at 10°C. Data is collected for 56,000 miles or an equivalent 36 kAh. During the second stage of the experiment, the nominal operating SOC of fixtures 1, 2 and 3 is set to 40%, 50% and 60% SOC respectively. The temperature of the battery at quasi steady state is regulated at 49°C and the ambient temperature is controlled

[2]The power management system in HEV typically regulates battery pack's SOC around the center of an operating window; however, this does not necessarily mean that the average SOC is at the center value of the target SOC operating window. In our work, power demand is the input without any SOC regulation, therefore the term *nominal SOC*, is used to refer to the initial SOC and not the average operating SOC.

at 25°C. Also, the current is scaled up by a factor of 1.3. Data is collected for 40,000 miles or an equivalent 27 kAh.

The experimental procedure consists of cycling the cells continuously using a US06 cycle for 900 cycles [corresponding to 7,200 miles or 4.6 KAh]. This is followed by a discharge capacity test and a pulse test for measuring resistance. Both tests are outlined below:

Capacity measurement:

i) Charge cells using a CCCV (constant-current constant-voltage) protocol to 4.1 V (100% SOC) at 1C rate. Rest for 24 hrs.

ii) Discharge cells to 2.9 V (0% SOC) at 1C rate (5 A).

iii) Measure and record discharge capacity.

Pulse test:

i) Charge cells using a CCCV (constant-current constant-voltage) protocol to 4.1 V (100% SOC) at 1C rate. Rest for 24 hrs.

ii) Discharge cells to 60% SOC at 1C rate. Rest for 1 hour.

iii) Apply a 120 A, 10 sec discharge pulse on all cells.

iv) Discharge cells to 50% SOC at 1C rate. Rest for 1 hour.

v) Apply a 120 A, 10 sec discharge pulse on all cells.

vi) Discharge cells to 40% SOC at 1C rate. Rest for 1 hour.

vii) Apply a 120 A, 10 sec discharge pulse on all cells.

Figure 4.1 shows a schematic of the setup used for capacity testing of the cells along with the results of capacity fading. The cells are connected in series so that the same current is applied to all of them and placed in a thermal chamber for ambient temperature control. They are clamped and constrained similar to what they would experience in the battery pack.

The choice of the driving cycle and nominal SOCs are deliberate. First, the US06 cycle is the most aggressive standard driving cycle requiring high power demand from/to the battery, which makes the power profile reasonable to investigate the battery performance related to power denials which relates to the drivability of the vehicle. Second, the rate of capacity fade is accelerated when operating around high stress and SOC [101, 102].

Authors in [103] observed that bulk force of constrained batteries increased with respect to increasing SOC. To study the effect of operating SOC on capacity fade, three nominal SOCs are selected.

The following empirical model is used to predict capacity loss,

$$S_{\text{loss}} = \left(\alpha_c + \gamma_c(0.66 - \text{SOC}_0)^c\right) \cdot \exp\left(\frac{-E_{\text{ac}}}{R_{\text{g}}T}\right) \cdot \text{Ah}^{\xi}, \tag{4.30}$$

where S_{loss} is the capacity fade in percentage, SOC_0 is the nominal SOC, $\text{SOC}_0 \in [0.33, 0.66]$, Ah is the charge throughput, R_{g} is the universal gas constant, 8.314 J/Kmol, and T is the cell temperature. Note that, due to lack of sufficient data to reflect the influence of temperature, the activation energy E_{ac} is assumed to be the same as the value in [80][3], 22406 J/mol. Identified constants, α_c, γ_c, c, ξ, E_{ac} and R_{g}, are listed in Table 4.1.

The performance of the capacity fade model is shown in Fig. 4.18 by comparing with experimental data. The model would allow for capacity calculation up to 100,000 miles for the different operating nominal SOCs and temperatures. The calculated degraded capacity after 100,000 miles is used instead of the initial capacity for battery simulation in Section 4.6.

[3]The chemistries of batteries in [80] are NMC-LMO/graphite.

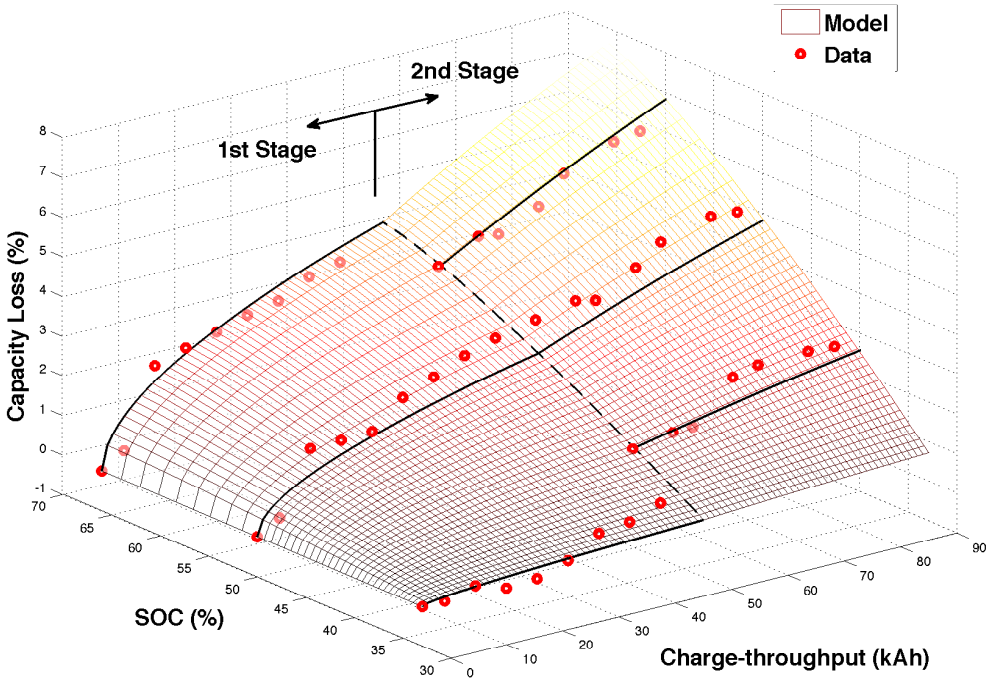

Figure 4.18: A capacity fade model with experimental data

Table 4.1: Constants for the Capacity Fade Model Eq. (4.30)

Constant	α_c	γ_c	c	ξ	E_{ac}	R_{g}
Value	153.4	-557	1.257	0.510	22406	8.314

Note that the degradation testing also resulted in an increase in the resistance of the cell. Since in an HEV application, characterizing the series resistance R_s is much more important than the dynamic resistances R_1 and R_2, the degradation of resistance R_s is only considered in this section. In [104], the increase in the value of R_s with degradation is shown to be more significant than that of the double RC pairs. It should be noted that for other applications, where the dynamic resistances are important, the degradation of those resistances should be considered. For the identification of R_s, an OCV-R-RC or an OCV-R-RC-RC should yield similar results. Thus, for simplicity and only for identification purposes, an OCV-R-RC model is formulated. A least squares identification method is used and outlined below. If we consider an OCV-R-RC equivalent circuit model in discrete-time

domain:

$$
\begin{aligned}
z(k+1) &= z(k) - \frac{\Delta T}{Q} I(k), \\
V_c(k+1) &= \left(1 - \frac{\Delta T}{R_1 C_1}\right) V_c(k) + \frac{\Delta T}{C_1} I(k), \\
V(k) &= OCV(z(k)) - V_c(k) - R_s I(k),
\end{aligned}
$$

Also, if the measured signal is the output signal:

$$
y = OCV(z(k)) - V(k) = V_c(k) + R_s I(k),
$$

then we can, by manipulating the equations, derive a parametric form as:

$$
y(k) = \theta^T \phi(k),
$$

where

$$
\begin{aligned}
y(k) &= OCV(z(k)) - V(k), \\
\theta &= [b_1, b_0, a_0]^T, \\
\phi(k) &= [I(k), I(k-1), -y(k-1)]^T,
\end{aligned}
$$

where

$$
\begin{aligned}
a_0 &= \frac{\Delta T}{R_1 C_1} - 1, \\
b_0 &= \frac{\Delta T (R_1 + R_s)}{R_1 C_1} - R_s, \\
b_1 &= R_s.
\end{aligned}
$$

Accordingly, the series resistance R_s can be determined from the parameter b_1.

The final results of resistance increase are shown in Fig. 4.19. Results are plotted for all 3 fixtures at the 3 different pulsing SOCs. Note that the results show a big variation. However for the final design of the pack, the resistance increase after 100,000 miles[4] is considered by applying a linear fit to the data. This is also consistent with the work in [80], where the results show a linear increase of resistance with charge throughput with a large variation in the identified resistance. The resistance increase after 100,000 miles is

[4]Automakers such as Nissan, Chevrolet, Toyota and Ford guarantee their battery packs for at least either 8 years or 100,000 miles whichever comes first.

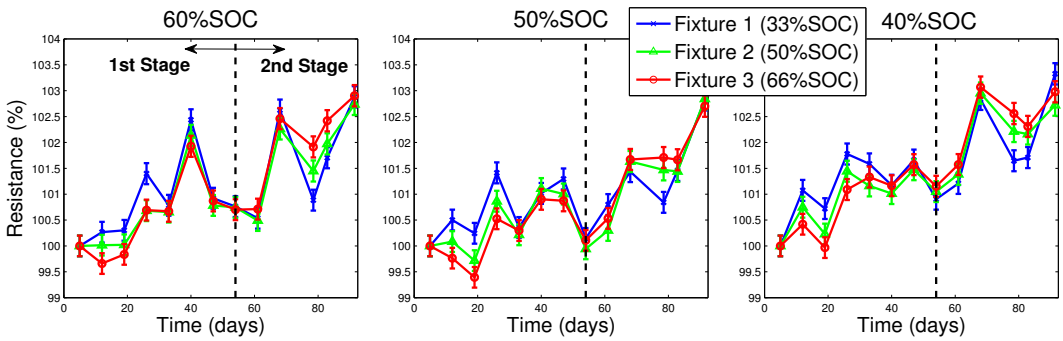

Figure 4.19: Series resistance increase as a function of degradation time for all three fixtures. Resistance results are shown at 60%, 50%, and 40% SOC.

calculated and used in the simulation results in Section 4.6.

Finally, for cost analysis, a Battery Performance and Cost model, BatPaC (the detailed description of BatPaC is available in [81]), is adopted. This model is developed by Argonne National Laboratory, and is publicly available and has been widely used for calculating battery cost [82, 83, 84]. The calculated battery cost is meant to represent projections of a 2020 production year with an assumption of an annual production level 20,000–500,000. This model allows to design a battery pack for a specified power, energy, different type of electrified vehicles, and cooling conditions. The objective of using the BatPaC in is to compute a battery pack cost with variation in the number of cells while battery performance is satisfied.

The battery of interest is a prismatic Nickel-Manganese-Cobalt/Graphite Li-ion cell in HEV application; thus, NMC333-G and HP-HEV (High Power HEV) are chosen as a cell chemistry and vehicle type, respectively. In addition, cabin air is considered as a heat transfer fluid in this study. The battery cells are all connected in a series, and two modules per a battery pack are assumed based on a baseline pack design, Ford's HEV.

4.6 Results

Quantitative analysis on battery performance is conducted by testing the battery model and the power limiting method described before with the simulated US06 power input at various operation conditions: (1) ambient temperatures, $T_\infty \in \{-5, 25\}^\circ$C; (2) nominal SOCs, $\text{SOC}_0 \in \{0.35, 0.4, 0.45, \cdots, 0.65\}$; and (3) number of cells in a battery pack, $N_b \in \{48, 50, \cdots, 76\}$. These changes in operating conditions affect the battery performance such as battery utilization, average current, temperature rise, and capacity fade. As the battery size changes, the battery power in a cell level is scaled correspondingly to provide

the same power in a pack level. The limits on voltage and SOC for the power limiting algorithm are shown in Table 4.2. Note that the SOC limits define a window of 40% SOC operating range. All results in this section are based on cell level and not pack level.

Table 4.2: Upper and lower limits on Voltage and SOC

Output	Lower/Upper Bound	Unit
Voltage	2.5/4.1	V
SOC	$SOC_0 \pm 0.2$	–

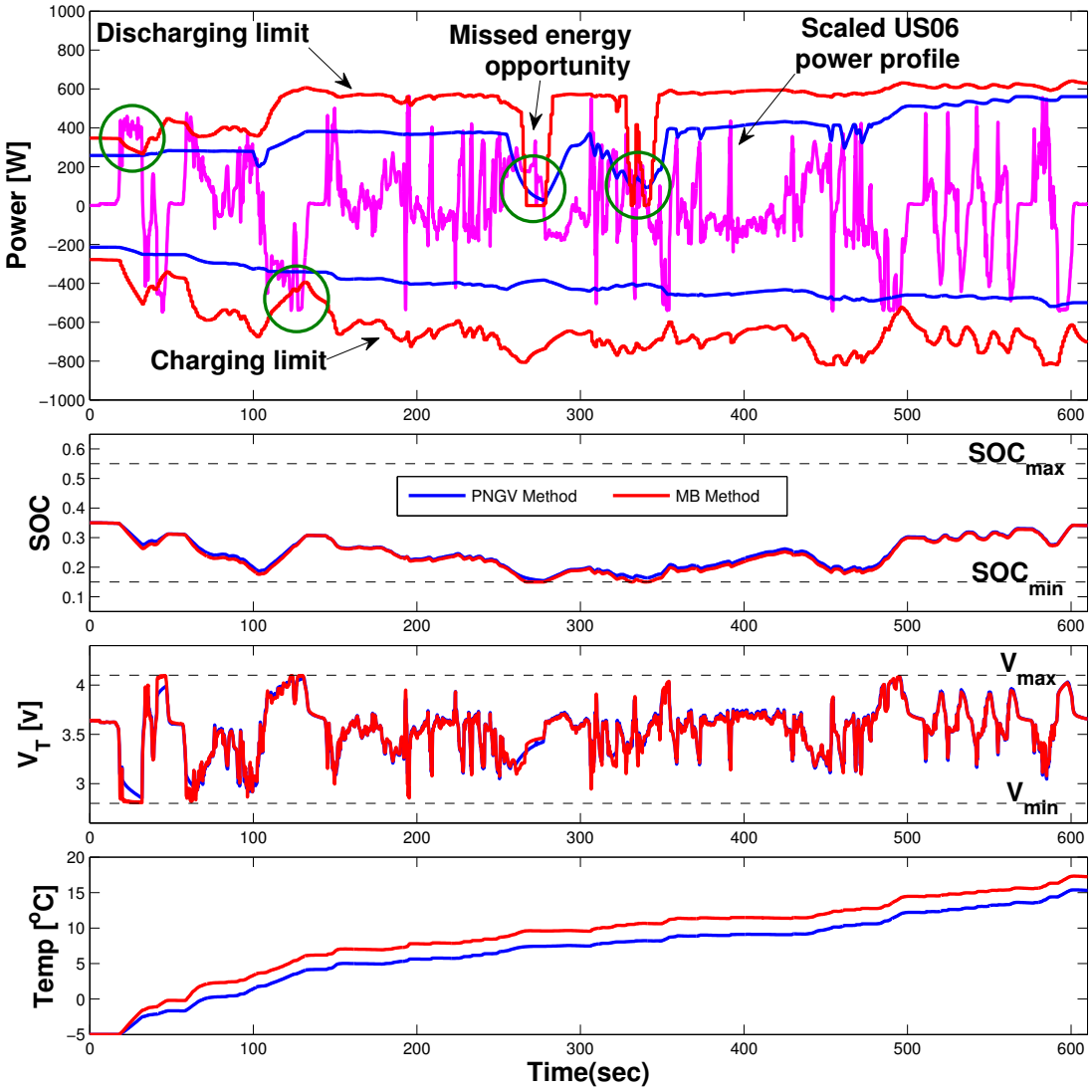

Figure 4.20: Power, SOC, voltage, and temperature profiles at 35% SOC, $T_\infty = -5°$C and number cells = 64

To provide a better understanding, time series plots of power, SOC, voltage and temperature at 35% SOC, $T_\infty = -5°$C and $N_b = 64$ are shown in Fig. 4.20, as an example. The first subplot shows a scaled (by a factor of 1.2) simulated battery power associated with US06 drive cycle, and the discharge (+) and charge (-) power limits for one cell in the $N_b = 64$ cell pack. These power limits vary because the battery's internal states and parameters change. Note that the actual power input to the battery is clamped by these two limits. The first subplot also shows instances (highlighted in green circles) where the power input to the battery exceeds the power limits. The first two circles at $t = 20$ sec

and $t = 120$ sec show instances where the lower and upper voltage limits respectively are reached and so power is clamped. Moreover, the third and fourth circles show instances where the lower SOC limit is reached and, thus, also the power limit is clamped. These violations represent missed energy opportunities that the cell could have provided. Also, for reference, the PNGV power limits are also shown with the resulting SOC, voltage and temperature profiles. Notice, how the MB power limiting algorithm allows for more utilization of the battery than the PNGV model. For this case of $N_b = 64$ cells in the pack, since the battery power input is increased, the cell needs to provide more power and current when compared to the baseline case ($N_b = 76$ or power factor = 1). Thus, changes in total energy-throughput, root-mean-square averaged current and temperature rise can also be determined. Apart from potential power denial concerns, the total energy-throughput during power denials – where the magnitude of battery power is greater than or equal to power capability – is of interest because this number would be related to fuel consumption, i.e. the supervisory controller in the HEV will increase the power demand from the engine.

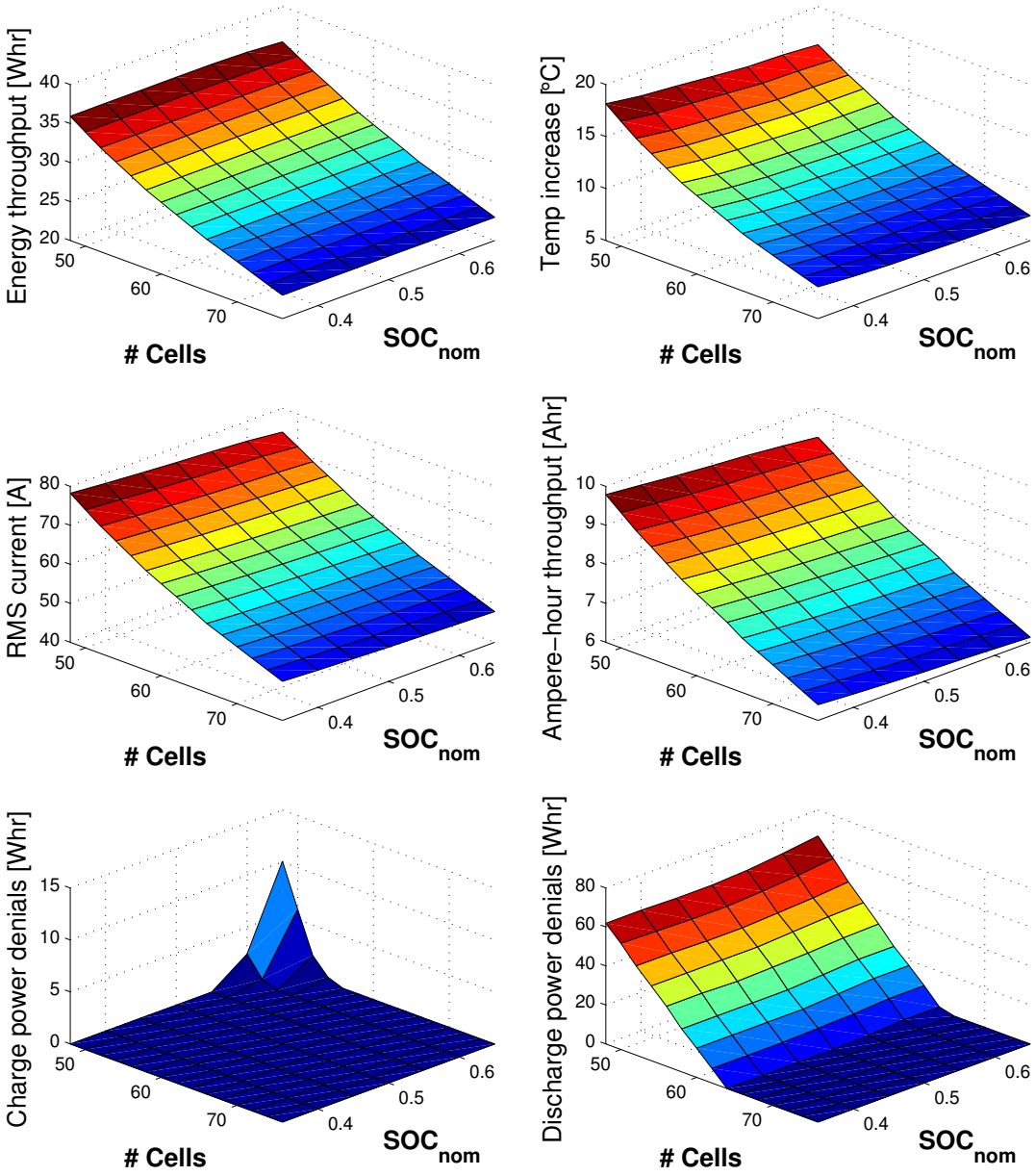

Figure 4.21: Energy throughput, temperature, RMS current, Ampere-hour throughput, and charge and discharge power denials at $T_\infty = 25°\text{C}$.

Simulation results of the parametric study for one cell in a pack of N_b cells are plotted in Fig. 4.21. The energy-throughput utilization (upper left), temperature increase (upper right), RMS current (middle left), Ampere-hour throughput (middle right), charge power denials (lower left), and discharge power denials (lower right) are plotted as a function of

nominal SOC and number of cells at an ambient temperature of $T_\infty = 25°\text{C}$. The charge power denials (CPD) and discharge power denials (DPD) are computed by:

$$\text{CPD} = \sum \min\{P_\text{b}^\text{dmd} - \bar{P}_\text{b}^\text{chg}, 0\}\Delta t,$$
$$\text{DPD} = \sum \max\{P_\text{b}^\text{dmd} - \bar{P}_\text{b}^\text{dch}, 0\}\Delta t,$$

where the battery power demand, the maximum charge power and the maximum discharge power are denoted by P_b^dmd, $\bar{P}_\text{b}^\text{chg}$ and $\bar{P}_\text{b}^\text{dch}$, respectively.

All results are computed after completing one simulated US06 power cycle. The simulation assumes a degraded cell resistance and capacity after 100,000 miles instead of a fresh cell. As expected, results show that as number of cells in a pack decrease, the energy throughput increases. Accordingly, the temperature, RMS current and Ampere-hour throughput increase as well. The charge power denials graph shows only violations at the high SOC and with low number of cells. This is expected since with lower number of cells and higher operating SOC, the cell is more likely to hit the high voltage limits. More interestingly, the discharge power denials graph shows that the number of cells in a pack can be scaled down without violating any discharge power constraints, meaning that drivability is not affected.

Since different number of cells and operating SOCs result in different temperature rise as seen in Fig. 4.21, the effect of temperature is isolated by adjusting the cooling to maintain the same equilibrium temperature. By decoupling this effect, and by using Eq. (4.30), the simulated capacity fade after 100,000 miles of the cell is shown in Fig. 4.22 for two different temperatures. Figure 4.22 shows that capacity fade is significantly affected by the nominal operating SOC but not by the number of cells (or indirectly by the Ampere-hour throughput), and is accelerated at higher temperatures. This means that downsizing a pack will not lead to a significant increase in capacity fade.

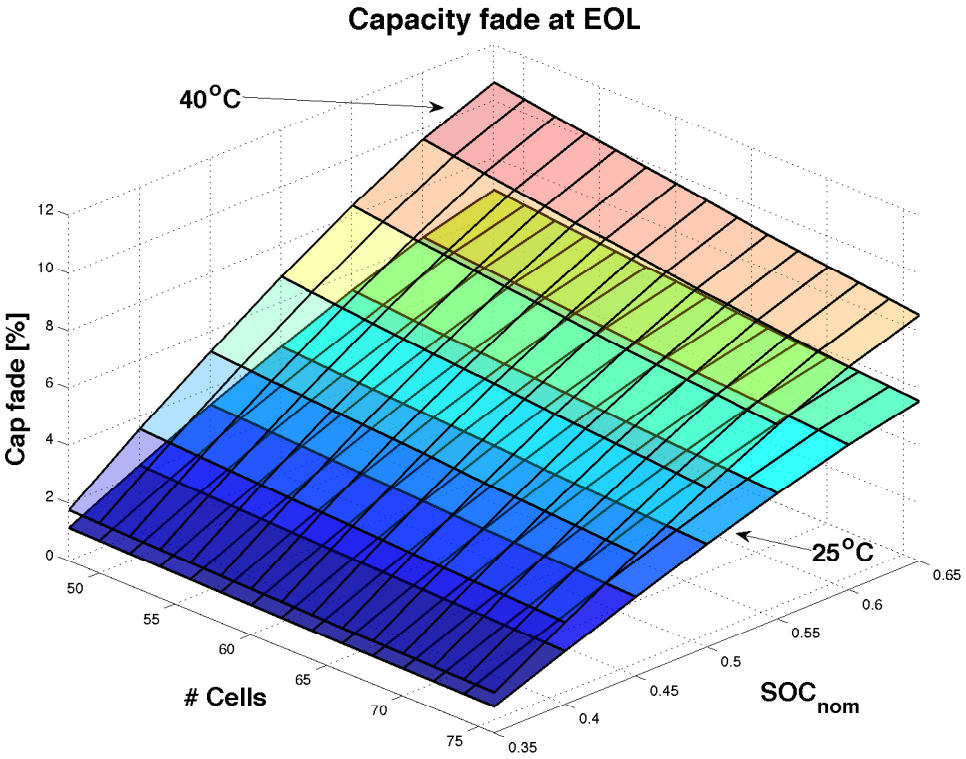

Figure 4.22: Capacity fade after 100,000 miles at a cell temperature of $25°$C and $40°$C.

Also, instead of adjusting the cooling capacity to maintain same equilibrium temperature, one could look at the projected capacity loss while maintaining the same cooling conditions. Accordingly, the Ampere-hour throughput from Fig. 4.21 can be used to find the projected Ampere-hour throughput at 100,000 miles along with the equilibrium temperature for a given pack cooling condition. The resulting capacity fade after 100,000 miles is shown in Fig. 4.23.

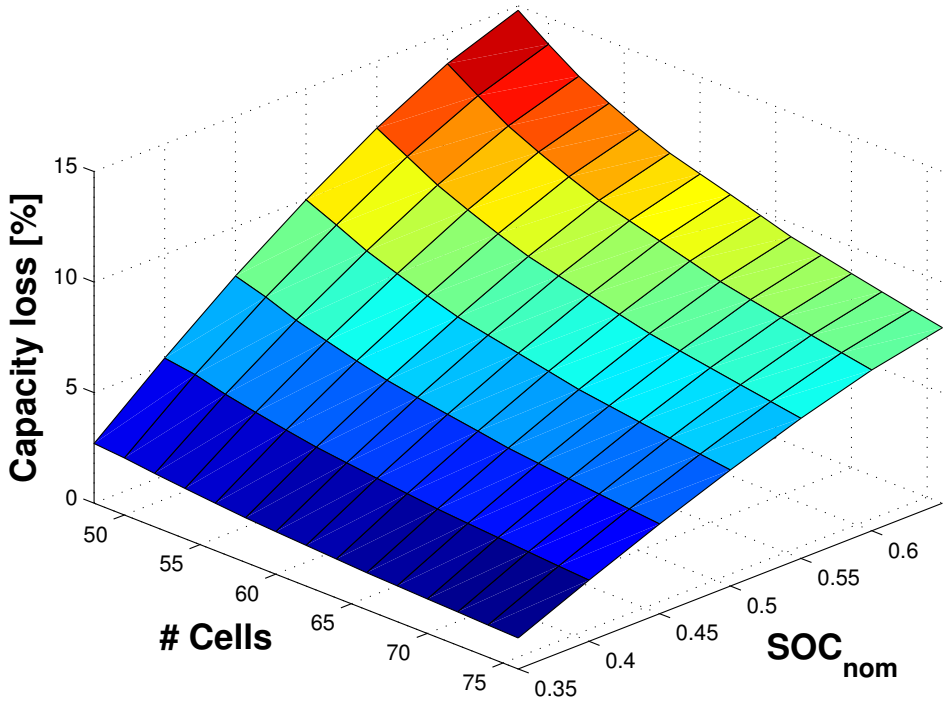

Figure 4.23: Capacity fade after 100,000 miles for a given constant cooling condition at T_∞ = 25°C.

Figures 4.21, 4.22 and 4.23 together show that the number of cells could be scaled down which results in higher cell utilization and without experiencing any discharge power denials (i.e. unavailable discharge energy throughput is zero). Also, operating the cell at a lower SOC would result in minimal capacity fade after 100,000 miles, even with a smaller number of cells.

The efficiency of the battery is also calculated for the case of zero charge and discharge power denials at T_∞ = 25°C. In computing the efficiency of the battery, a charge sustaining current profile during a US06 driving cycle is scaled down to allow the SOC to swing with a $\pm 10\%$ window. The battery efficiency, η_{b} in percentage, is calculated according to Eq. (4.31),

$$\eta_{\text{b}} = \frac{\sum \left(|E_{\text{thru}}| - |E_{\text{loss}}| \right)}{\sum |E_{\text{thru}}|} \times 100, \tag{4.31}$$

where E_{thru} is the energy throughput and $E_{\text{loss}} = I^2 R_s + V_1^2/R_1 + V_2^2/R_2 - ITdU/dT$ is the loss through the battery. Accordingly, Fig. 4.24 shows a plot of the efficiency of the battery for the cases of zero power denials. Notice that the efficiency of the cell only

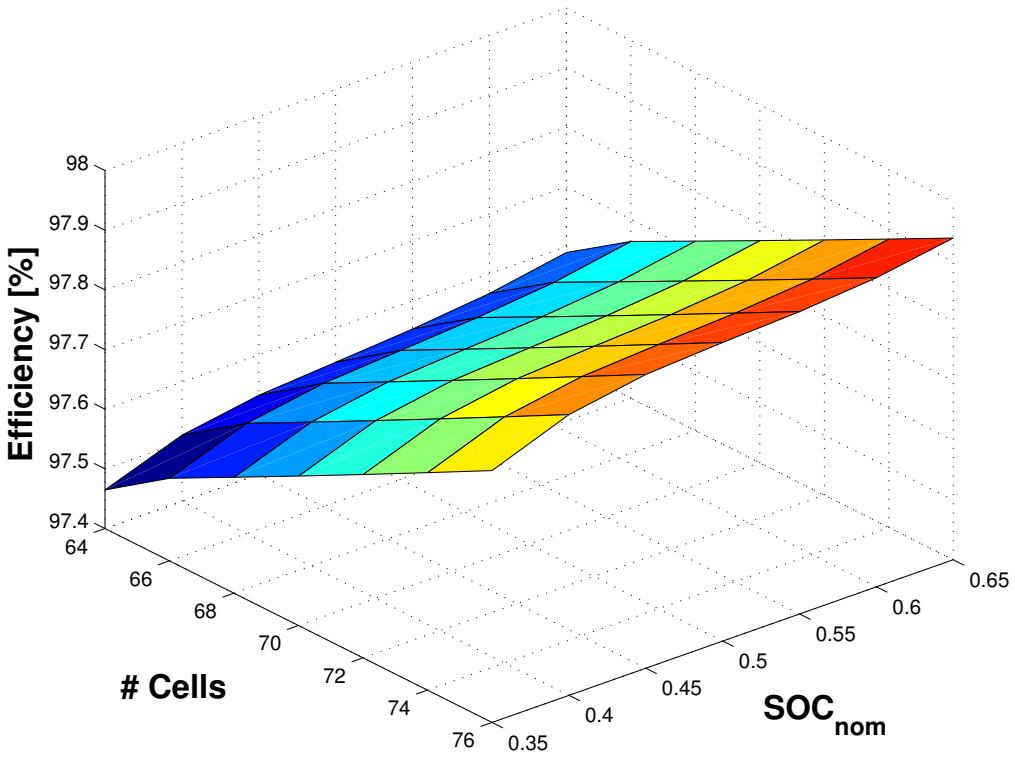

Figure 4.24: Efficiency of the battery for the zero power denials case at $T_\infty = 25°$C.

changes slightly as the nominal SOC is lowered from 65% to 35%. Also, as the number of cells are lowered, the efficiency decreases since there is higher current through the battery and accordingly even more losses.

Figure 4.25 shows the resulting energy throughput utilization, temperature increase, root mean square (RMS) current increase, Ampere-hour throughput, charge power denials and discharge power denials as a function of nominal SOC and number of cells at an ambient temperature of $T_\infty = -5°$C. Results again show that operating at lower SOCs will result in higher cell utilization with minimal discharge power denial even with a scaled down battery pack size (lower number of cells). However, at these low temperatures, the resistance of the battery is large, and thus, even with a full pack ($N_b = 76$ cells), voltage limits are violated and power is clamped. Therefore, as shown in Fig. 4.25, the discharge power denials subplot shows that there are no instances where discharge power constraints are not violated. However, the charge power denials plot shows that operation at lower SOC is preferable. This is because operation at higher SOCs means that the cell is more likely to hit the upper voltage and SOC limits. Also, since, collectively, the charge and dis-

charge power denials are less at lower SOCs than at higher SOCs, this means that the cell can allow more energy throughput initially. This helps warm up the cell and thus further decreases the power denials because of the decreased resistance. Moreover, even though, the cell experiences power denials at $T_\infty = -5°$C, downsizing the pack can actually help warm up cells. Figure 4.26 shows the temperature profiles for both the PNGV and MB method for a pack of 76 and 64 cells. Notice how the cells warm up faster with a downsized pack and especially using the MB algorithm since it allows more utilization than the PNGV algorithm.

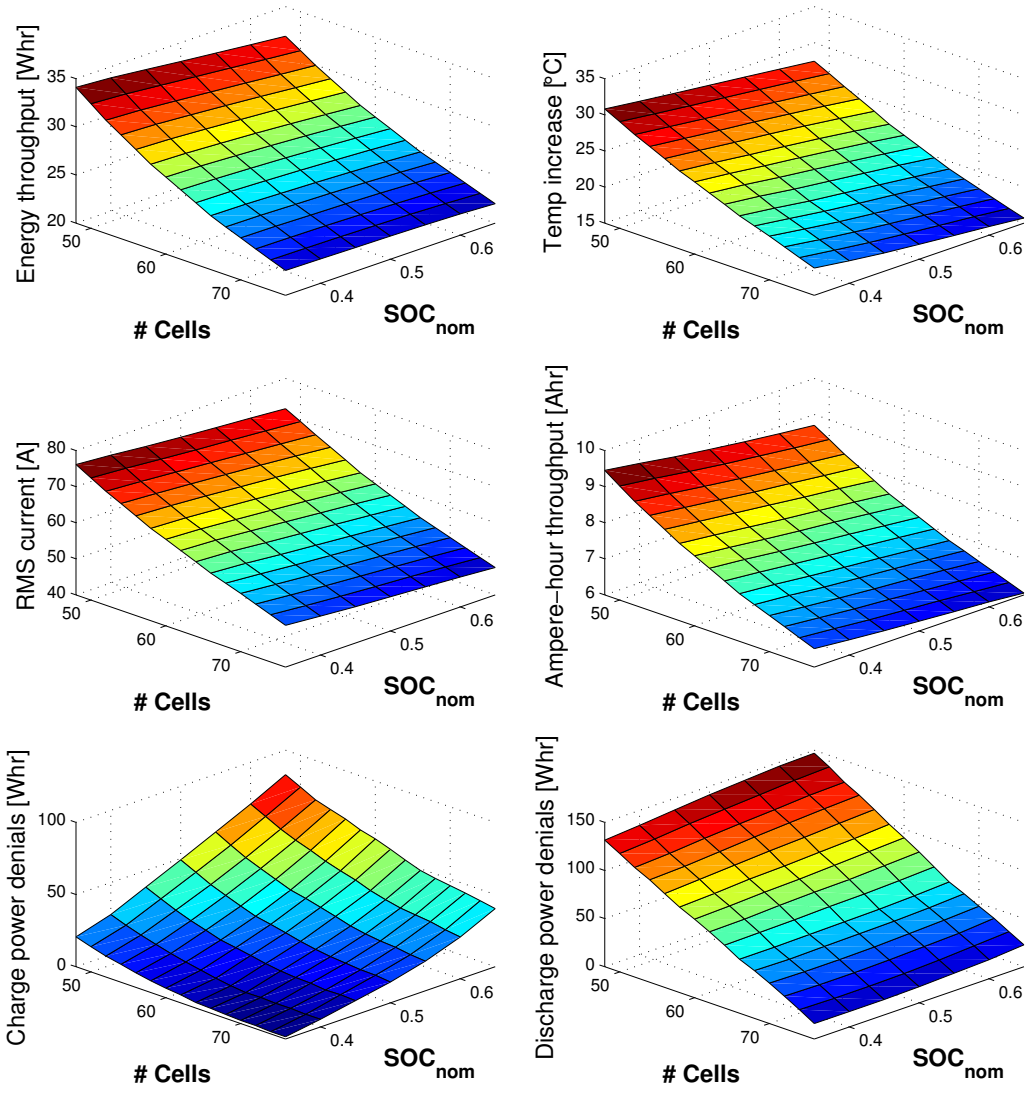

Figure 4.25: Energy throughput, temperature, RMS current, Ampere-hour throughput, and charge and discharge power denials at $T_\infty = -5°$C.

From Fig. 4.21, it can be deduced that at 35% SOC (preferable operating SOC in terms of capacity fade), the number of cells could be decreased from 76 to 64 without violating any discharge power constraints.

A zero power denials line could be extracted from Fig. 4.21. This line defines the minimum number of cells at each SOC for which the cell can provide full discharge power, even after 100,000 miles of operation. Figure 4.27 shows the zero power denials line on a plot of capacity fade after 100,000 miles versus energy throughput per cell. In order for

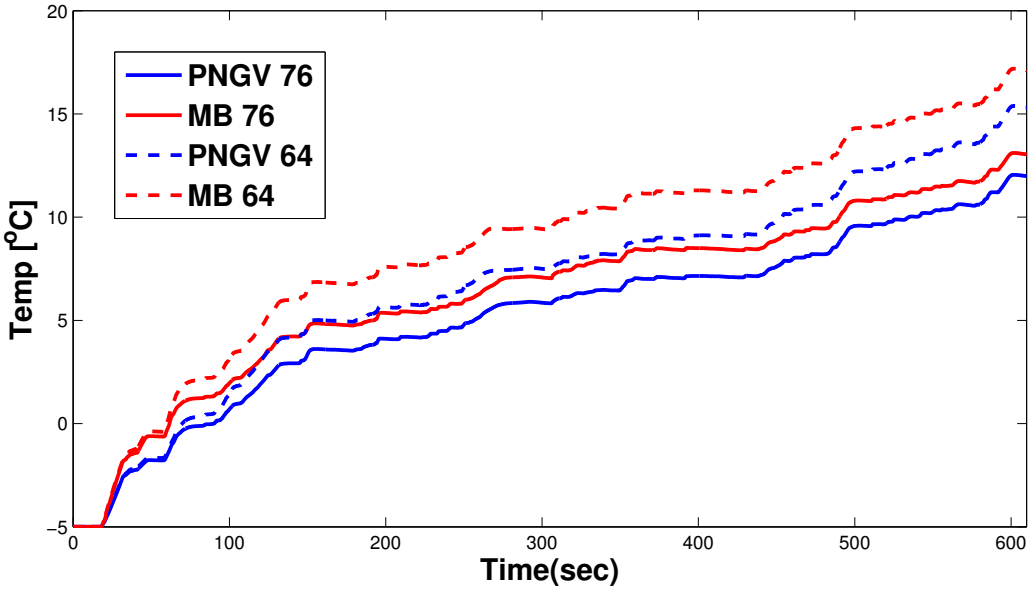

Figure 4.26: Temperature profiles for a pack of 76 and 64 cells using the PNGV and MB algorithms at $T_\infty = -5°$C.

the pack to deliver full discharge power, the operating point has to be to the left of the zero power denials line, meaning there are no violations of the discharge power constraints. The plot shows that for low energy throughput, operation could be around any SOC. As the number of cells is decreased, the energy throughput per cell is increased. At higher SOCs the capacity fade is much faster than at lower SOCs as shown in Fig. 4.22, this means that the cells are more susceptible to exceed the SOC limits. This is why operation at lower SOCs allows for a smaller battery pack. However, if the capacity fade after 100,000 miles is less than that specified by the manufacturer warranty, then the number of cells can be significantly decreased in a hybrid pack while experiencing zero power denials. For example, in designing a battery pack, according to Fig. 4.27, if the capacity fade after 100,000 miles should be less than 7%, then to maintain the ability of all cells to provide full discharge power, a minimum of 64 cells can be used that operate nominally at any SOC between 35% and 50% SOC. The resulting energy throughput per cell would be close to 27.45 Whr. Based on the above analysis, it is thus possible and beneficial to downsize a battery pack from 76 cells to 64 cells.

Table 4.3 summarizes the results of decreasing the number of cells from 76 to 64 at a nominal SOC of 35%. Note that the results are for a single simulated US06 power input cycle assuming operation for 100,000 miles, and the capacity fade is the total capacity

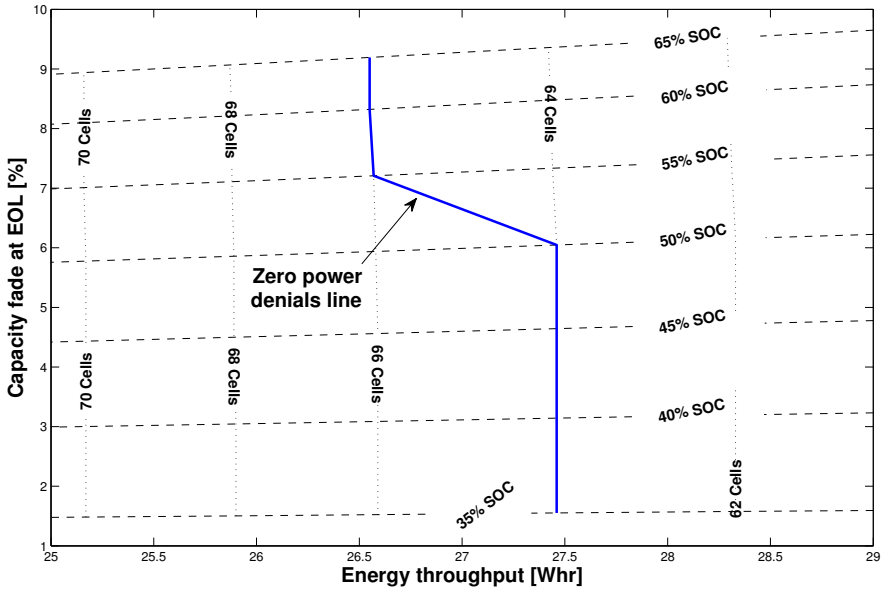

Figure 4.27: Zero power denials plot of capacity fade after 100,000 miles vs. energy-throughput per cell at $T_\infty = 25°\text{C}$.

fade projected at 100,000 miles. It is calculated by taking the equilibrium battery operation temperature of the cell using a simulated US06 power input cycle, and using Eq. (4.30) to predict the capacity loss. For $N_b = 64$ cells, a 19% Whr increase in utilization per cell results only in a 0.5% increase in capacity fade over the lifetime of the battery without experiencing any discharge power denials (violating discharge power constraints) as compared to a base case of $N_b = 76$. The RMS current also increases because of higher power request, and accordingly, the temperature of the cell also increases. Next, we look at the financial aspect or the cost associated with decreasing the number of cells in the pack.

In investigating the cost associated with downsizing the number of cells in a pack,

Table 4.3: Results of Battery Downsizing at $T_\infty = 25°\text{C}$ and 35% SOC.

Number Cells	76	64	Change
Energy utilization [Whr]	22.99	27.45	+19 %
Temperature increase [°C]	8.04	11.23	+3°C
RMS current [A]	50.00	59.76	+20 %
Discharge denials [sec]	0	0	–
Capacity fade [%]	1.54	2.05	+0.5 %
Efficiency [%]	97.8	97.4	-0.4 %
Cost [%]	1540	1388	-10 %

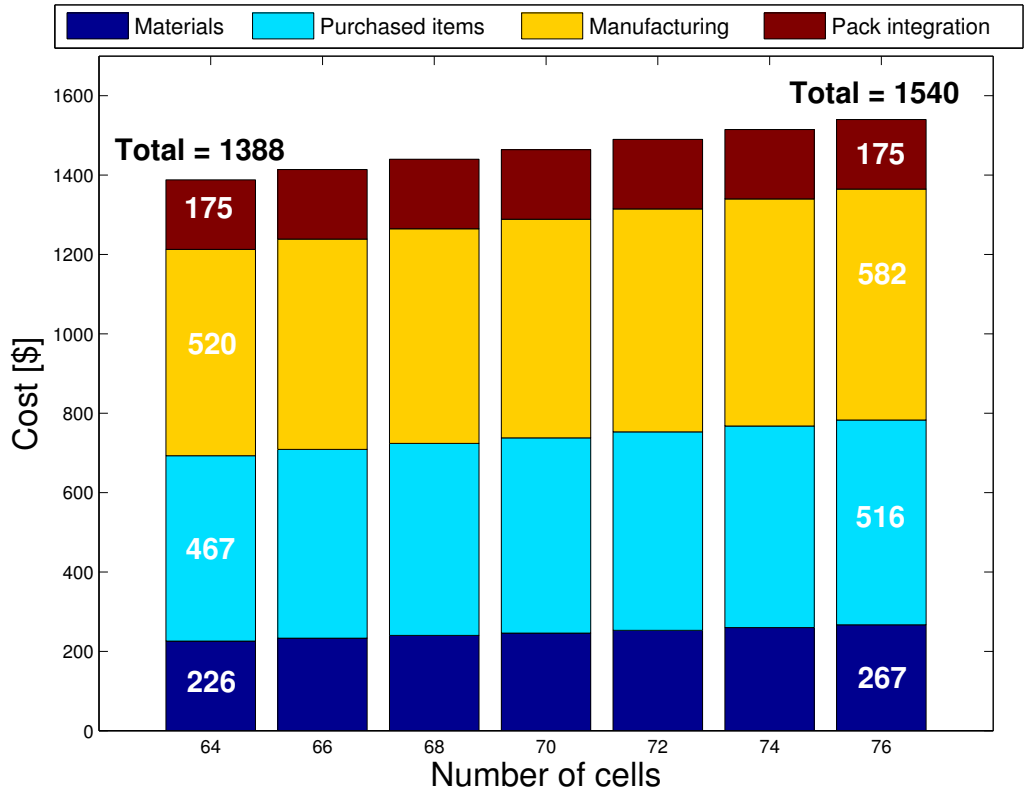

Figure 4.28: Cost breakdown of the battery pack as a function of the number of cells.

the BatPac model is used. Since BatPac model scales the size of the cell as the number of cells are decreased, the model is modified to allow for the cells to maintain the same size and capacities as their number changes. Accordingly, Fig. 4.28 shows the total cost of the battery pack to the OEM as the cells are decreased. The total cost consists of the cost of materials, purchased items, manufacturing and pack integration. Results show that decreasing the number of cells from 76 to 64 leads to a 10% decrease in total cost from $1540 to $1388. The biggest reduction is from the cost of materials at 15%. The cost of purchased items and manufacturing are reduced by 9% and 11% respectively, while the cost of pack integration remains the same at $175.

4.7 Conclusions

This section presented an opportunity to downsize a battery pack – especially, for an HEV application – from 76 cells to 64 cells without experiencing any power denials and with only a 0.5% increase in capacity fade. The effect of varying nominal operating SOC and the number of cells in the battery pack on the performance of the Li-ion batteries

was considered. Specifically, performance metrics including energy-throughput utilization, temperature increase, RMS current, unavailable discharge/charge energy, capacity fade, and cost were considered for a quantitative analysis.

In evaluating the performance of the battery of interest, a predictive thermo-electric model and a semi-empirical capacity fade model were used to capture SOC, voltage, temperature and capacity fade of the Li-ion cells. Particularly, the capacity fading model was parameterized using data collected from a novel set of experiments for the NMC chemistry in which an actual power profile from an HEV over an aggressive federal driving schedule, US06, was used. A new performance metric of power denial was introduced to identify regions of zero power denials (no violations of discharge/charge power requirements) as a function of nominal operating SOC, capacity fade and energy throughput per cell. As a result of battery downsizing, a 10% cost could be reduced, which was assessed by using Argonne National Laboratory's Battery Performance and Cost (BatPac) model.

Future work would explore coupling the presented analysis with a full hybrid electric vehicle model including all powertrain components and a supervisory controller, and analyze the resulting change in miles per gallon when downsizing a battery pack and how that compares to the cost saved by switching to a smaller battery pack.

The final chapter will introduce a novel method for estimating the capacity fading in a battery pack. This is important in applications of EVs and PHEVs where capacity defines the range of those vehicles.

CHAPTER 5

Capacity Estimation

5.1 Introduction

Lithium ion batteries have been one of the most popular choices for use as power sources in electric vehicles (EVs) and hybrid electric vehicles (HEVs). Their popularity stems from their high energy and power densities and their ability to achieve long driving ranges. However, their performance suffers from aging and degradation [15, 16, 17] that should be accounted for and recognized for efficient long term performance. Thus significant research has been focused on trying to understand the aging mechanisms in Li-ion cells and connect them with measurable and identifiable features in an effort to improve the utilization and reliability of these cells through the battery management system (BMS). Many important battery states are affected by aging which is also names as the state of health (SOH). The SOH of a battery is usually quantified using either resistance growth [39, 18, 19, 105, 106, 107] or capacity fading [20, 21, 22, 108]. This chapter focuses on capacity fading as an indicator of SOH.

Several methods haven been introduced in literature for the evaluation of the aging in battery. Traditional and conventional methods rely on voltage measurements. In Cyclic Voltammetry (CV), the electrode potential is ramped linearly versus time [23]. The resulting cyclic voltammogram shows the anodic and cathodic currents. The shift in these peaks is correlated with aging. This method, however, can not be practically used in a vehicle pack as it requires, besides the cell and data acquisition system, a potentiostat, current-to-voltage converter and a reference electrode. Probability density function (PDF) applies a statistical method to the charge/discharge voltage data of a cell to extract the PDF curve [24]. As the cell degrades, the PDF curve shifts which allows for aging detection. Another widely known method is the differential voltage (DV) method [100, 109, 110]. The method plots the differential of voltage over capacity with respect to capacity. Finally, one of the most recent methods in literature is the incremental capacity analysis (ICA) [22, 108, 109, 111]. In many cell chemistries, the cells are characterized by a voltage

plateau for a wide range of SOCs. The ICA method plots the incremental capacity over voltage (dQ/dV) with respect to voltage, which allows for clearly identifiable peaks that correlate with capacity fading. This method has been recently shown to predict capacity fading with less than 1% error [22].

Although the ICA method has been shown to be accurate in estimating capacity fade, it still has some major setbacks. First, the method is sensitive to voltage measurements. Computing the differential of voltage could result in noise (since dV=0). This is especially the case in Lithium iron phosphate (LFP) cells which are characterized by flat voltage curves. Second, the ICA peaks in discharge are centered around the low SOC range. For example, in the case of a Nickel-Manganese-Cobalt Oxide (NMC) cell, the ICA peaks are centered around 40%. This means that the BMS has to traverse the low SOC range in order to estimate and monitor capacity fading. Also, in a battery pack where cell expansion is limited, measuring the strain can be hard and can result in low signal to noise ratios, which makes the methods, such as that presented in [112], hard to implement.

In more recent work, focus has been directed towards understanding and modeling the mechanical behavior of batteries [28, 29, 112, 113] in an attempt to provide better means to estimate the states of a battery, mainly SOC and SOH. In [29], it has been shown that force measurements can decrease the mean and standard deviation of the SOC estimation error by up to 50% in some regions. The authors in [113] show that, unlike voltage which changes minimally with C-rate, strain can vary significantly and can be used for characterizing dynamic system states. More recently, other methods have investigated the first and second derivative of strain with respect to charge, by measuring the strain on the surface of the battery during charging and discharging. Note that these methods have been applied to a battery that is not constrained in any way and is allowed to expand freely. In [112], it is shown that the second derivative of strain with respect to capacity exhibits similar shift in peaks as those resulting from the DV method as the cell degrades in a more consistent and reliable manner.

In exploring the mechanical behavior of cells packaged in commercial packs and how the measured behavior can be used for better SOH estimation, this chapter introduces a novel method of monitoring force measurements associated with electrode expansion using the ICA method to derive the IC curves. In lithium-ion batteries, charging causes volume change or swelling of the electrodes as the lithium ions intercalate in the negative electrode. In such cases, the work in [112] is applicable since the free expansion can be measured. However, in applications where the batteries are constrained or compressed to prevent expansion, as in the case in a real vehicle application, the swelling causes a stress. This stress can be measured using a force sensor mounted on the end plates of a cell pack or module

as described in Sec. 5.2.1. The resulting measured force can thus be used in the incremental capacity analysis. Incremental capacity analysis based on force measurements (ICF) is promising since force does not necessarily exhibit the flatness that the voltage curves versus SOC exhibit making the force derivative easier to compute and more accurate without the need for expensive force sensors. In the case of an NMC cell, the ICF peaks occur around 70% SOC while those of the ICV occur around 40% SOC. Hence the proposed ICF based SOH monitoring could happen more frequently within the regular use of a vehicle involving short trips where the SOC does not usually fall below 50%.

This chapter is organized as follows: first, Section 5.2 shows the experimental fixture for measuring force and states of the battery of the cells is shown along with the degradation experiments used. The results of the capacity fading are presented in Sec. 5.3.1. Then the ICF method is shown in Sec. 5.3.2 and 5.3.3. Finally, the C-rate dependance of the ICF method is investigated in Sec. 5.3.4.

5.2 Experimental setup

5.2.1 Force measurements

The batteries used in this study are Lithium Nickel-Manganese-Cobalt (NMC) Oxide battery. Each battery is $120 \times 85 \times 12.7$ mm with a 5Ah nominal capacity. A flat-wound jelly roll is encased inside the aluminum hard shell of the battery. The jelly roll does not fill the whole enclosure and thus there are air gaps around the sides and the top of the cell. The structure of the jelly roll results in electrode expansion in the direction perpendicular to its largest face [113]. The NMC cells are extracted from a HEV battery pack. Usually in a free expansion case [112, 113], cycling the cells results in a measurable strain or expansion. The second derivative of this strain can further be used in estimating the stage transitions in electrodes and the degradation of a cell [112]. However in a HEV pack, multiple cells are stacked together in an array and constrained together under compression to prevent expansion. Thus, as these cells are cycled in an actual vehicle pack, it will be easier to measure stress and not strain. To emulate the typical pack conditions in lab, 4 different fixtures were fabricated consisting of three lithium ion batteries each. Figure 5.1 shows one of those fixtures. Since SOH or capacity fading is the primary objective of this study, the 4 different fixtures are intended to test the effect of nominal operating SOC and initial preloading conditions on the degradation rates of cells. The details about the degradation experiments are presented in Sec. 5.2.2. Each fixture has two garolite end plates in between which are the 3 batteries, a garolite middle plate and a load cell. The fixture is clamped

together using bolts with lock nuts to prevent it from loosening. The load cell is a 500 lbs (LC305-500) Omega load cell sensor (strain gauge type) that is instrumented to measure the resulting force when the cells are being cycled. It has a 500 lbs full range with an accuracy of 1 lbs. The garolite middle plate is meant to act as a separator between the load cell and the cells. This is to prevent the load cell from acting directly on the cells and possibly puncturing them. The middle plate is also slightly lifted off the ground as to not allow the ground friction to absorb some of the force exerted by the cells. The cells are separated by a plastic spacer with dimples on it to allow for air to flow between the cells for cooling purposes and also maintain compression between the batteries. Also, since thermal expansion of the cell material can result in measurable strain or expansion in the cells [114], affecting the force, it is important that the temperature of the cells be measured, and the thermal expansion is avoided or taken into account. A set of 4 arrays of resistance temperature detector (RTD) sensors are instrumented on one side of the middle battery of each of the 4 fixtures. The RTD arrays are made from flexible kapton substrate and composed of platinum with a nominal 100 Ω resistance. They are less than 100 μm thick and have a 0.5°C accuracy. Each array has 4 RTD sensors totaling 16 temperature sensors in each fixture. The RTDs allow for spatial surface temperature measurement of the middle cell as it is being cycled. These RTDs have been shown to improve the observability and convergence of the core temperature estimation of the battery as compared to a conventional thermistor sensor placed close to the tabs [33]. The accurate estimation of the cell core temperature is important at high C-rates for clarifying how much of the observed force is due to thermal expansion and how much is attributed to lithium ion intercalation. All data is sampled at a 1 Hz rate. The fixtures are placed in a thermal environmental chamber for ambient temperature control.

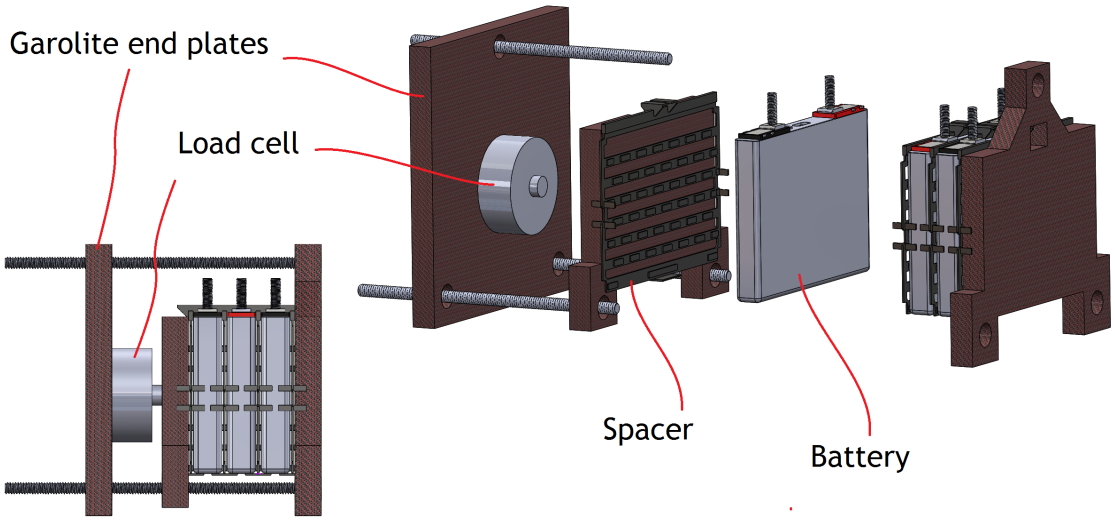

Figure 5.1: Schematic showing 3 lithium ion cells sandwiched between two garolite end plates. A load cell is installed for measuring the force due to cell expansion. The end plates are bolted together while the garolite middle plate is meant to act as a separator between the cells and the load cell.

5.2.2 Degradation experiments

Typically, quantitative analysis of degradation is either based on capacity fade [20, 21] or growth in internal resistance of the battery [39, 18, 19, 105, 106, 107]. In this chapter, the focus is on capacity fade since it is very important for the range of EVs, and could be important in the future for hybrids if the SOC window for these batteries widens. Since aging related mechanisms are shown to be coupled to mechanical effects [16, 115], the 4 fixtures are designed to test degradation while cycling with the same current profile at different states of charge (SOC) and initial preloading conditions. Capacity fade is shown to be slower at lower SOCs as shown in other studies [35, 102, 116], perhaps due to the lower bulk stresses on the battery [103]. As such, Table 5.1 shows the nominal SOC and preloading force for all 4 fixtures. The nominal SOC is defined as the nominal SOC at which the cell is being cycled at, and preload is the initial force that is used to clamp the cells before any degradation experiments. The preload is set at an initial SOC of 50% at 25^{o}C for all 4 fixtures.

Table 5.1: Operating conditions for all 4 fixtures

(1^{st} stage / 2^{nd} stage)	Fixture 1	Fixture 2	Fixture 3	Fixture 4
Initial SOC [%]	$33/40$	$50/50$	$66/60$	$50/50$
Ambient Temperature [°C]	$10/25$	$10/25$	$10/25$	$10/25$
Initial Preload [lbs]	$168/168$	$168/168$	$168/168$	$334/334$
ΔSOC [%]	$20/26$	$20/26$	$20/26$	$20/26$
ΔVoltage [V]	$0.46/0.62$	$0.41/0.48$	$0.43/0.48$	$0.41/0.47$
ΔForce [lbs]	$47/81$	$33/66$	$21/47$	$37/71$

Note that this is a two stage degradation experiment. During the first stage of the experiment, fixtures 1 through 4 are set to $\{33, 50, 66, 50\}$ % initial SOCs and a preload of $\{168, 168, 168, 334\}$ lbs respectively at the ambient temperature of 10°C. During the second stage of the experiment, the current is scaled by a factor of 1.3 and the ambient temperature is raised to 25°C. Since the current was scaled in the second stage, the initial SOCs for fixtures 1 and 3 had to be moved closer to 50% SOC, otherwise voltage limits would be violated due to the high current rates. Specifically, the fixtures 1 through 4 are set to $\{40, 50, 60, 50\}$ % initial SOCs without changing the preload. A charge sustaining current profile is used for cycling the cells. The profile is the result of the hybrid power split. The fixtures are connected in series, hence, the same current passed through all the cells in all fixtures. Since the triple of cells in each fixture are at different SOCs, the resulting power throughput is, however, different. The details of the current profile is detailed in Appendix A.1. After cycling the cells continuously for 450 cycles, a test to measure capacity of the cells is performed. The corresponding procedure for measuring capacity is also detailed in Appendix A.2. After the capacity test, the testing continued for another 450 more cycles when another capacity test is performed. The entire testing involved 3500 cycles of stage 1 type experiments followed by 2700 cycles of stage 2 type experiments for a total of 64 KAh. This corresponds to 95000 total miles traveled for the Hybrid Ford Fusion.

5.3 Results

In the following sections, the capacity fading results of the degradation experiments are shown in Sec. 5.3.1. Sections 5.3.2 and 5.3.3 present the results of using bulk force measurements for offline bulk fixture capacity estimation and individual cell capacity esti-

mation respectively using incremental capacity analysis.

5.3.1 Capacity fading

To study the capacity fading mechanisms in the different fixtures, an approximately 20 min charge sustaining current profile, which is detailed in App. A.1, is applied to the cells continuously for 450 cycles. After that a capacity test is applied to the cells using a 5 A (1 C-rate) discharge current. The protocol for the capacity test is detailed in in App. A.2.

The results of the capacity fading are plotted in Fig. 5.2. The dashed vertical line represents the moment at which the second stage degradation experiment started. Since each fixture has 3 cells, the average capacity for each fixture is plotted against the number of cycles. The plot shows both absolute and percent capacity fade. Also, since each fixture is comprised of 3 cells each, a bar is used to represent the span of capacities of each of the 3 cells at each point. Notice, for example, that around 2700 cycles, the difference in capacity between the 3 cells in fixture 4 is around 2.5%. This is the largest imbalance between the 3 cells in any given fixture at any given time during the experiment. This is important because the capacity analysis that follows in Sec. 5.3.2 and 5.3.3 is based on the fact that the imbalance between the cells is not larger than 2.5%. However, a separate experiment is also performed to test the applicability of the capacity estimation method on cells that have an imbalance larger than 2.5%. This is detailed at the end of Sec. 5.3.3.

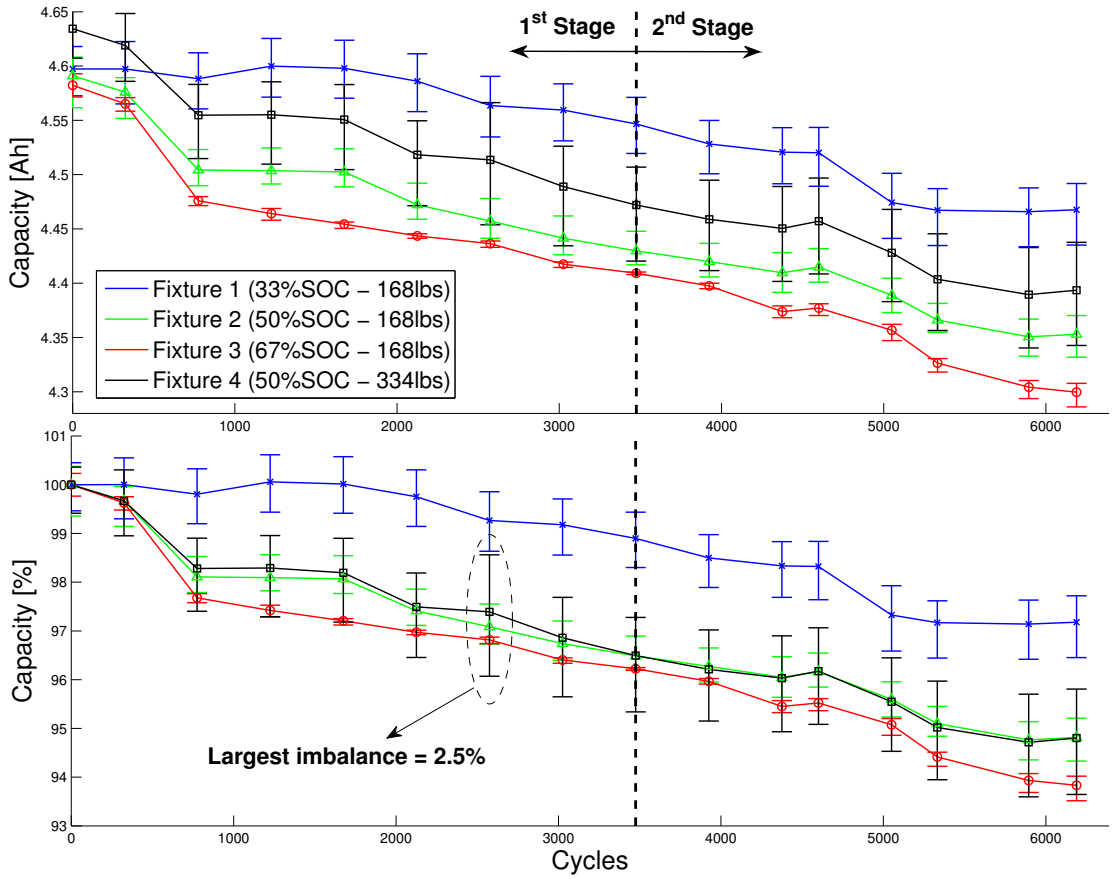

Figure 5.2: Capacity fading measured as it evolved for the various cells in the 4 different fixtures

Results show that fixture 1 which operates at 33% nominal SOC has the slowest rate of capacity fade, while fixture 3 which operates at the highest SOC (66%) degrades the fastest, similarly to what was shown in previous research [35, 102, 116]. Another important observation is that both fixtures 2 and 4 which have same SOC (50%) but different preloads (168 lbs and 334 lbs respectively) show almost identical rate of capacity fade. Also it is noticed that, except for fixture 1, all fixtures experience a significant drop in capacity initially. This could be a characteristic of the NMC cell being used and could be further investigated. Moreover, it seems that, during the second stage degradation experiment, where the temperature has been increased and the current has been scaled, the degradation rates do not change significantly. More data would be needed to verify this result since the second stage degradation was over 2700 cycles only.

In summary, results indicate that operation at low SOC results in slower rates of degradation. Also it is shown that the preload at this magnitude ($\sim$100 KPa) does not affect

degradation. In fact, it is only at higher pressures (>1 MPa) that a change in degradation rates can be noticed [117], with higher rates of applied pressure leading to higher rates of capacity fade. The results of the capacity fading experiments will be used for validation against the capacity estimation method to be presented in Sec. 5.3.2 and 5.3.3.

5.3.2 Offline incremental capacity analysis for bulk capacity estimation

Much focus has been directed towards the ability to monitor capacity fade [20, 21, 22, 108]. One of the approaches that yields appropriate capacity estimation results is the incremental capacity approach (ICA) [22, 108, 109, 111]. This method plots the differential of capacity to the differential of voltage versus voltage. Accordingly, one can easily identify peaks which correlate with capacity fading. This chapter shows that a non-electrical signal could be used in capacity fading identification, or more specifically, force measurements can correlate with capacity fading. The analysis in this section and the following section is done offline. Future work would have to include the implementation of these techniques online in on-board battery management systems.

Figure 5.3 shows the voltage and force plot as a function of discharge capacity during the 1C discharge test (refer App. A.2) for fixture 1 after different number of cycles. It is apparent that as the cell is discharged, the voltage and force decrease. As expected, the voltage decreases with the increasing number of cycles due to the fact that the cell capacity fades as the cell is cycled. Figure 5.3 also shows that the force changes as the cells are cycled. Unfortunately, this change is not monotonic with time as the cells are aged. This non-monotonic behavior could be the result of degradation or creep that is inherent to the fixture being used and has to be investigated further. One would have to revert to the derivative of the force measurements since those would be less dependent on the fixture and sensor attachment. From Fig. 5.3, one can extract the corresponding dV/dQ and dF/dQ curves. Figure 5.4 shows the dV/dQ and dF/dQ curves for fixture 1 after $N = 325$ cycles.

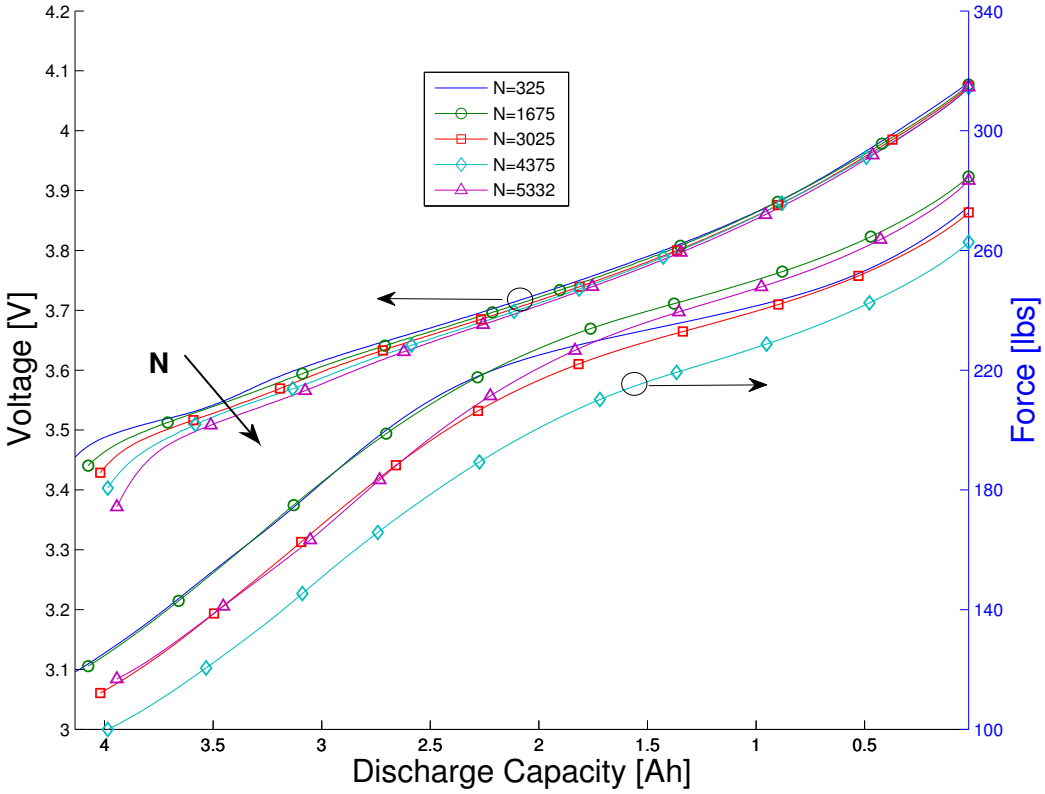

Figure 5.3: Voltage and force measurements during the 1C discharge capacity test after different N number of cycles

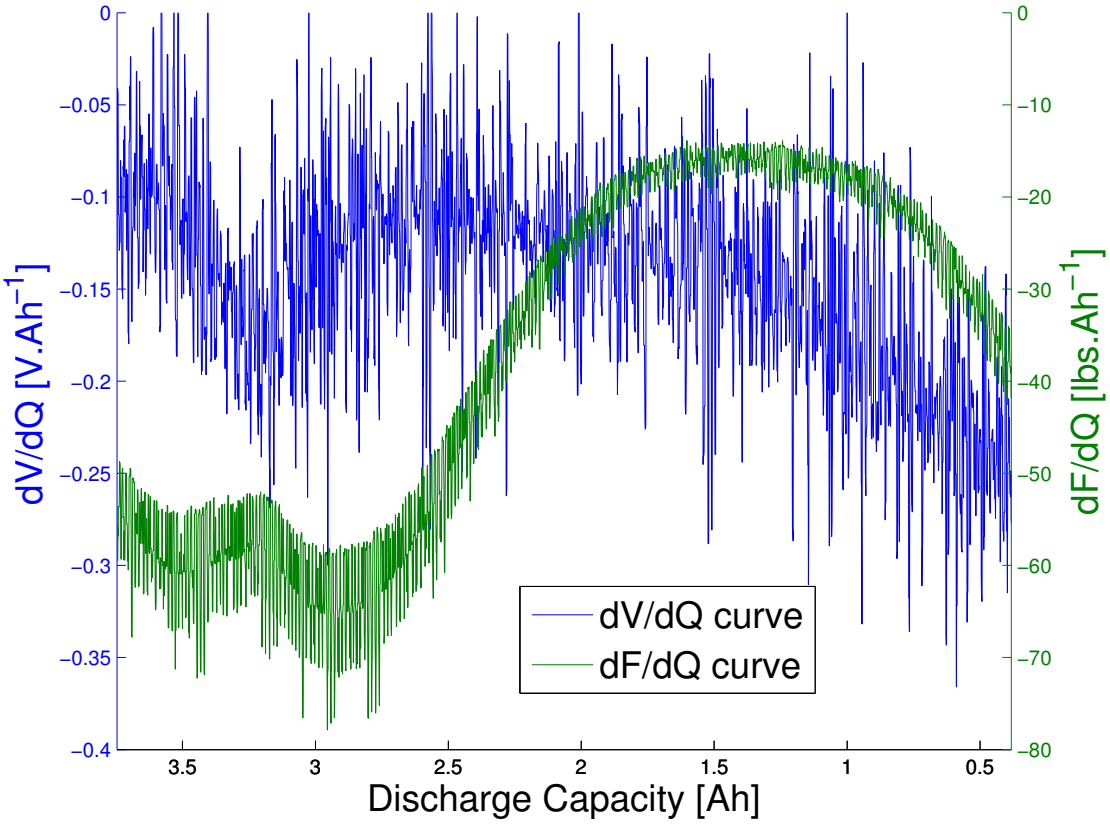

Figure 5.4: The dV/dQ and dF/dQ curves during 1C discharge capacity test for fixture 1 after $N = 325$ cycles

The plot in Fig. 5.4 shows that the derivative curves are very noisy and need filtering. Notice, however, that the dF/dQ curve has a better signal to noise ratio than the dV/dQ curve since the amplitude of the force signal is much bigger than that of the voltage signal. This makes data processing for the dF/dQ curve easier. Also, in other cell chemistries, not investigated here, such as the Lithium iron phosphate cells (LiFePO4), the voltage curves are characterized by voltage plateaus for a wide range of SOC [118]. As a result, this insensitivity would lead to even lower signal to noise ratios for the dV/dQ curves, since the value of dV is almost zero. In this study, a Savitsky-Golay (SG) filtering technique was used to process the data [119]. This methods fits to successive sets of data a low order polynomial using least squares method, and can improve the signal to noise ratio without affecting or distorting the signal. The SG filter requires the window or frame length (F) and the polynomial order (n) to be specified. The details of the filter are shown in App. C. For this study, $F = 951$ and $n = 3$ are chosen and are shown to result in a smooth fit.

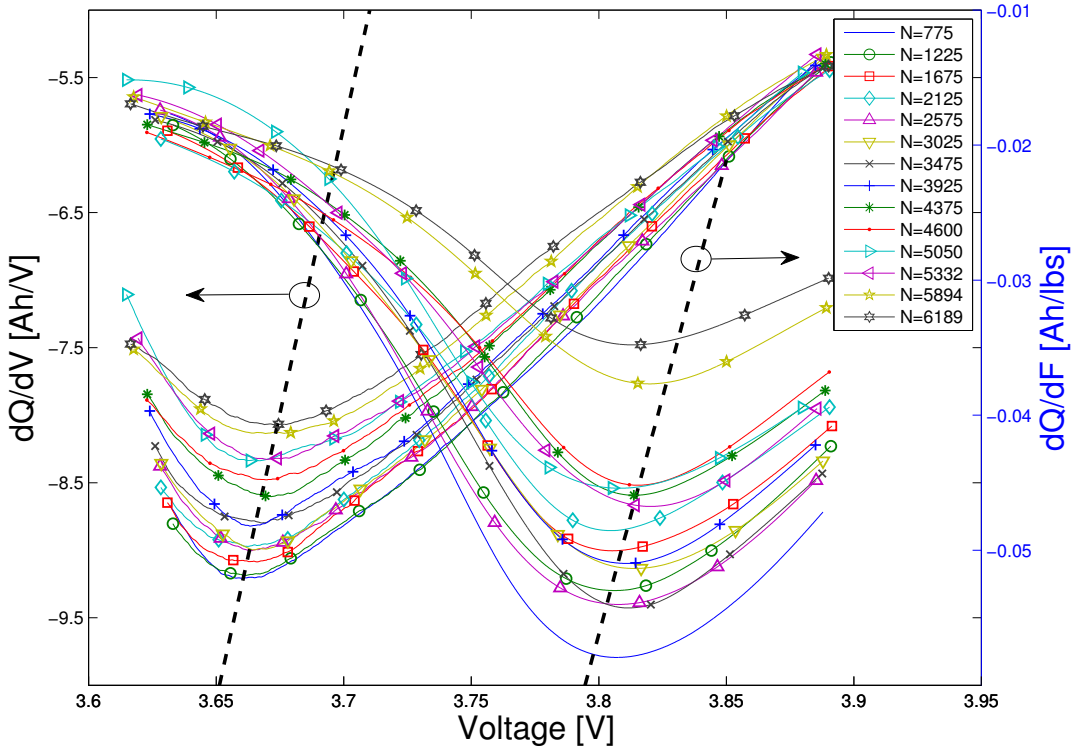

Figure 5.5: IC curves during 1C discharge capacity test for fixture 1 after different N number of cycles. Also shown is a linear fit of corresponding peak values.

With the new filtered data, the IC curves for both voltage and force are plotted specifically. The IC curves are defined as the inverse of the dV/dQ and the dF/dQ curves. Figure 5.5 shows a plot of the dQ/dV (ICV) and dQ/dF (ICF) curves as a function of voltage at different cycles. Notice that both the ICV and ICF curves exhibit the same behavior with shifting peaks as the number of cycles increases similarly to the findings in literature [22, 108, 112]. Figure 5.5 shows that the identified ICF peaks are at higher voltage (and thus higher SOC). This behavior is important in EVs and PHEVs since one does not have to traverse to the lower SOCs every time a capacity monitoring scheme has to be applied. Also, Fig. 5.5 shows two linear fits to the ICV and ICF peak values. The corresponding voltages at which the ICV and ICF peaks occur is defined as $\tilde{V}_{ICV}$ and $\tilde{V}_{ICF}$.

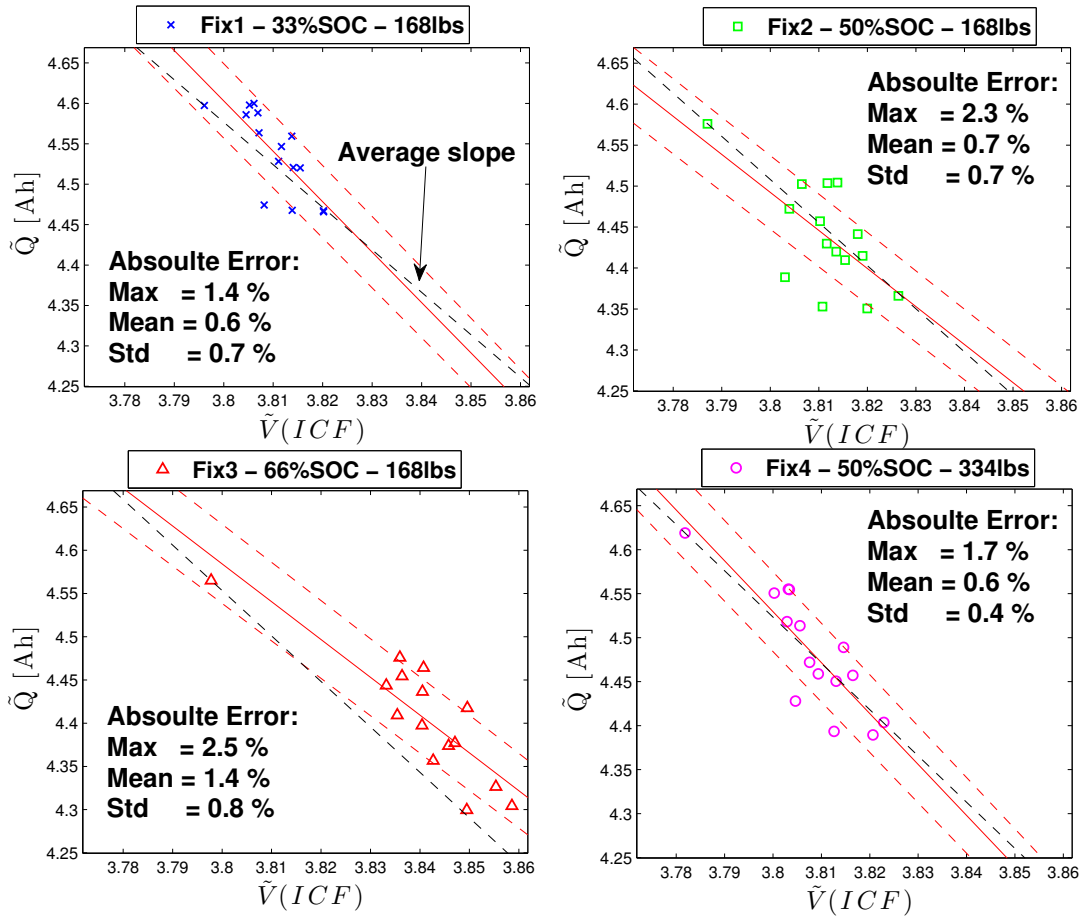

Figure 5.6: The measured capacity ($\tilde{\text{Q}}$) versus voltage ($\tilde{V}_{ICF}$) at peak ICF for all fixtures with a linear fit with a band of 1% (red line). Also black dashed line is the average slope from all fixtures fitted through the first data point of every fixture. This slope is used for the capacity estimation ($\hat{Q}$). The respective absolute maximum, mean and standard deviation on the error between the measured capacity ($\tilde{\text{Q}}$) and the estimated capacity ($\hat{Q}$) using the average slope of all fixtures is also shown.

Finally, a plot of the measured capacity ($\tilde{\text{Q}}$) of the cell versus the identified voltage at which the ICF peak occurs ($\tilde{V}_{ICF}$) can be created. Figure 5.6 shows the resulting measured capacity ($\tilde{\text{Q}}$) versus the $\tilde{V}_{ICF}$ values. Results show a linear trend of capacity fade with shifting ICF peaks. The 4 subplots show the corresponding measured capacity ($\tilde{\text{Q}}$) versus $\tilde{V}_{ICF}$ values with a linear fit with a 1% band (in red solid and dashed lines) for all 4 fixtures. Also using all 4 fixtures, an average slope ($\alpha_{avg} = -5.28$ [Ah/V]) of the 4 different linear fits to the 4 fixtures can be calculated. This slope is considered to be representative of the degradation mechanisms of the NMC cells being used in these experiments. The resulting

estimated change in capacity ($\Delta\hat{Q}$) can thus be calculated using Eq. 5.1.

$$\Delta\hat{Q} = \alpha_{avg} \times \Delta\tilde{V}_{ICF}, \tag{5.1}$$

or when expanded,

$$\hat{Q} - \tilde{Q}_0 = \alpha_{avg} \times (\tilde{V}_{ICF} - \tilde{V}_{0,ICF}), \tag{5.2}$$

where $\tilde{Q}_0$ is the initial measured capacity of the cell, $\tilde{V}_{0,ICF}$ and $\tilde{V}_{ICF}$ are the corresponding measured voltages at which the peak ICF occurs during a 1 C discharge experiment for $\tilde{Q}_0$ and $\hat{Q}$ respectively, and $\alpha_{avg} = -5.28$ [Ah/V] is the calculated average slope using the degradation experiments on all 4 fixtures.

Thus, in each subplot in Fig. 5.6, Eq. 5.1 is represented by a dashed black line that fits through the initial capacity measurement of each fixture and is used for the estimation of capacity. The resulting max, mean and standard deviation on the absolute error between $\hat{Q}$ and $\tilde{\mathrm{Q}}$ is also shown in each subplot. The absolute error is defined using Eq. 5.3.

$$\text{Absolute error}[\%] = \left| \frac{\hat{Q} - \tilde{Q}}{\tilde{Q}} \right| \times 100, \tag{5.3}$$

The maximum error on capacity estimation is $\leq 2\%$ for fixtures 1, 2 and 4 that operate at low SOC levels. The mean error is $\leq 0.5\%$. Fixture 3, however, has a maximum error of 2.5% with a mean error of 1.5%. This could be due to the fact that the initial measurement for the first data point might be inaccurate, which resulted in the fitted line being below the rest of the consecutive measured data points as shown in Fig. 5.6. This could also be attributed to the fact that a first order linear fit used here oversimplifies the actual degradation mechanism which could follow a higher order fit. This is to be verified with more experimental data. The results thus show that using a linear fit on all data from all 4 fixtures, the estimated capacity difference is $\leq 2.5\%$ (worst case). The analysis above describes the ability of this method to estimate the bulk capacity of each fixture using bulk force measurements. However, since each fixture is comprised of 3 cells each, the ICF method lumps and smears the effect of all the 3 cell degradation. In the following section, the potential of a bulk force measurement for individual cell capacity estimation is analyzed.

Note also that ICF curves are identified using a 5 A (1 C-rate) discharge test (refer App. A.2). It would be interesting to investigate whether the ICF curves exhibit the same peak locations for different C-rates, or whether they are less sensitive to C-rates than the ICV curves. The authors in [112] showed that the second derivative of strain with respect to capacity ($d^2\epsilon/dQ^2$) is more suitable at predicting stage transitions in electrode materials at C-rates of up to C/2. Section 5.3.4 will investigate the dependance of the ICF curves

to different C-rates, and whether the force behavior matches the strain behavior shown in [112].

5.3.3 Offline incremental capacity analysis for individual cell capacity estimation

The adequacy of the above prescribed method of using bulk force measurements to estimate individual cell capacities in each of the 3 cells constrained in a fixture is analyzed in this section. Figure 5.7 shows the ICF curve versus the bulk voltage of the 3 cells in fixture 1 and versus individual cell voltages after $N = 325$ cycles. Notice that since the cells have slightly different capacities, the resulting ICF curve has different peak locations for the different cells. Using the average slope ($\alpha_{avg} = -5.28$ [Ah/V]) of capacity fade versus $\tilde{V}_{ICF}$ identified in Sec. 5.3.2, the estimated capacity ($\hat{Q}$) of each individual cell can be identified using Eq. 5.1 for all the cells in all 4 fixtures. Figure 5.8 shows the estimated ($\hat{Q}$) and measured capacity ($\tilde{\text{Q}}$) for all cells in the 4 fixtures, with the corresponding errors between the measured and estimated capacity. Results show that, over 6200 cycles (corresponding to 95000 miles), bulk force measurements results can be used to estimate the individual cell capacities.

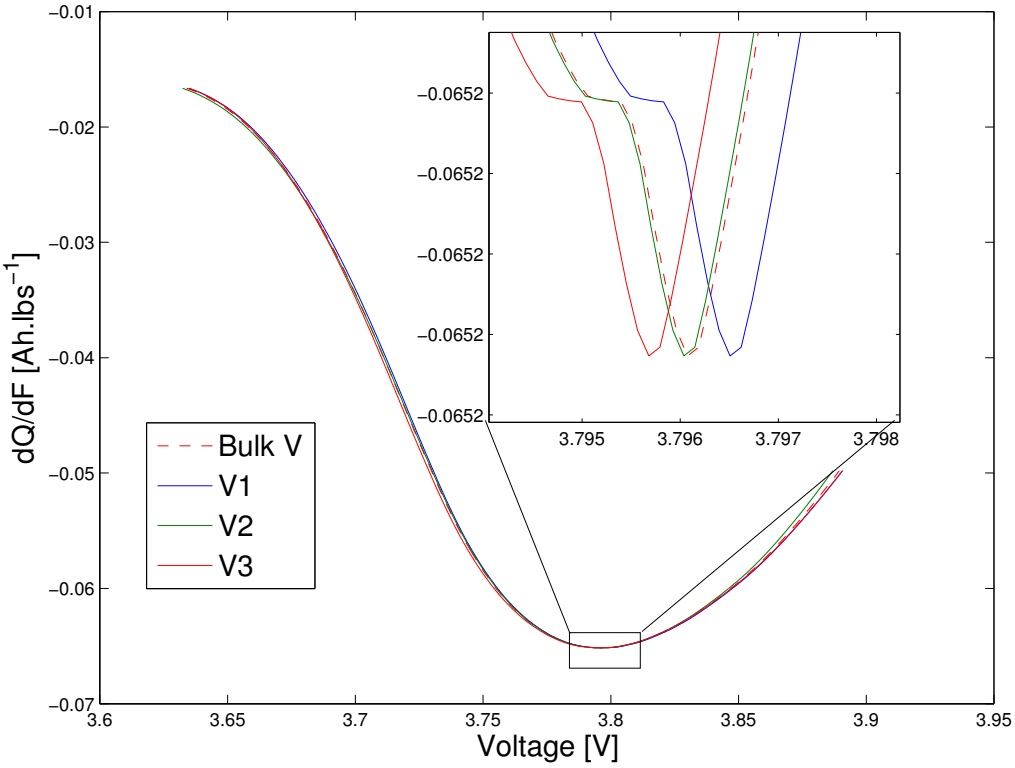

Figure 5.7: ICF curve vs bulk fixture voltage and individual cell voltages for fixture 1 after 325 number of cycles.

The maximum error between the measured and estimated capacities across all fixtures at any given time during the 6200 cycles is 3.1%, while the absolute mean and standard deviation on the error is 0.42% and 1.14% respectively, as shown in Fig. 5.9.

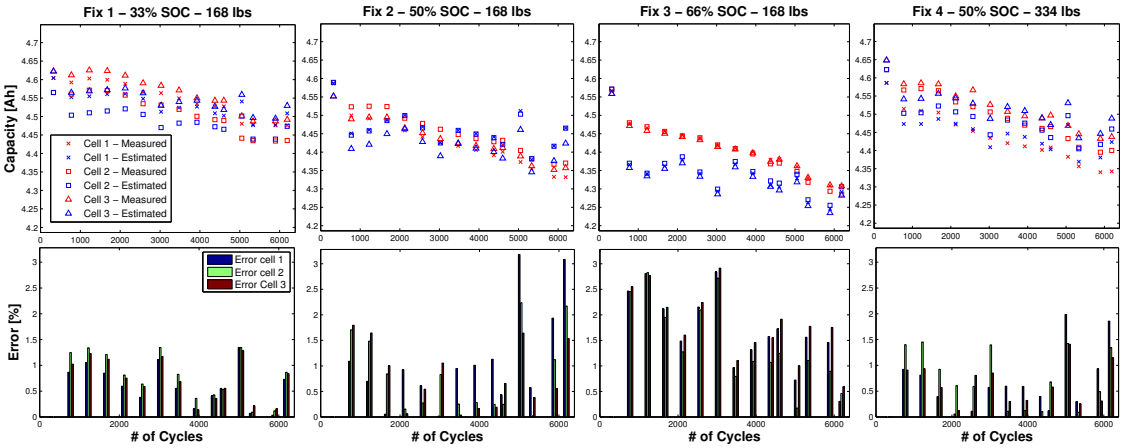

Figure 5.8: Results of using bulk force measurements to estimate individual cell capacities. Row 1 shows the estimated and measured cell capacities in each fixture over 6200 cycles. Row 2 shows the resulting errors on the measured and estimated capacities.

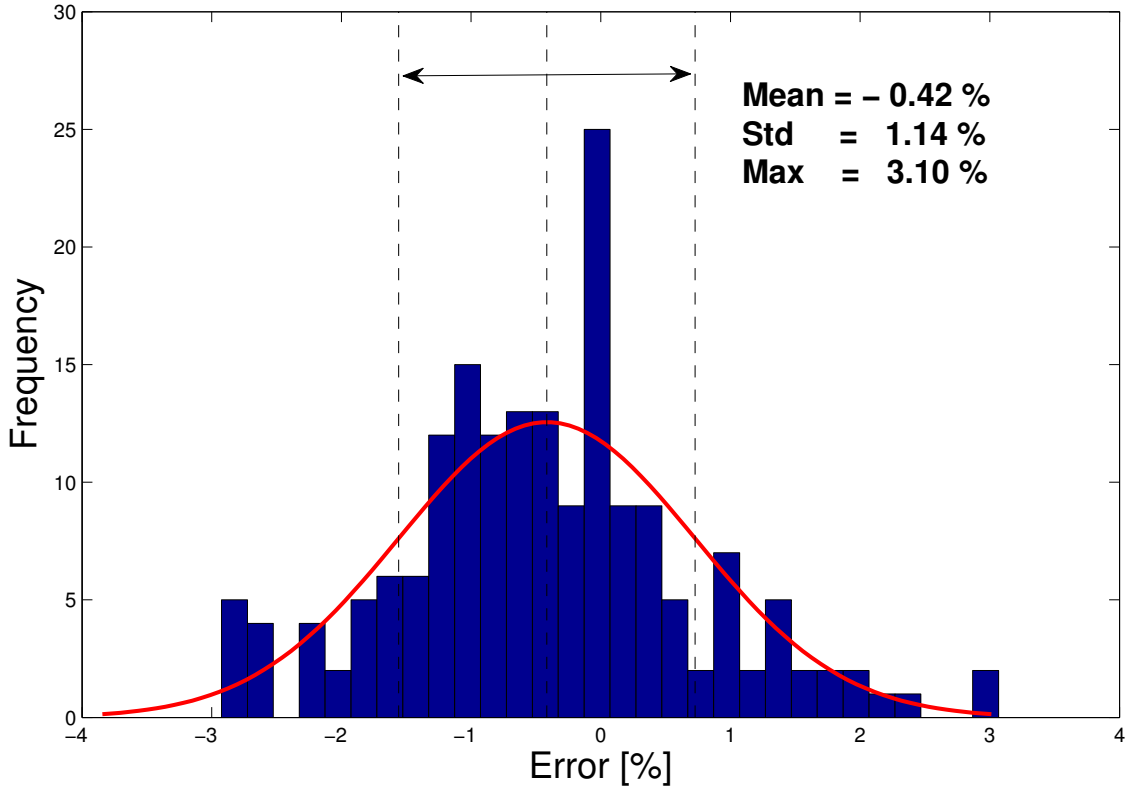

Figure 5.9: Histogram of errors on capacity estimation using the ICF method for the 4 different fixtures with 3 cells each. The estimation is done over 6200 cycles of degradation (corresponding to 95000 miles).

Note that this result has been shown for cells in which the maximum imbalance in capacity is 2.5%. This means that at any given time, the difference in capacities between the 3 cells in any given fixture is $\leq 2.5\%$. To investigate the adequacy of this method for estimating capacity for cells that are more imbalanced, an experiment with two different fixtures was performed. Table 5.2 shows the capacity of the cells in two fixtures. The first fixture has a large degraded cell bundled with two other slightly degraded cells. The mean difference in capacity between the large degraded cell and the slightly degraded cells is 27.5%. The second fixture has a fresh cell bundled with two other slightly degraded cells. The mean difference in capacity between the fresh cell and the slightly degraded cells is 4.7%. The degraded and fresh cells are highlighted in bold in Table 5.2.

Table 5.2: Cell capacities for the two fixtures

Cell Capacities	Fixture 1	Fixture 2
Cell 1 [Ah]	4.47	4.31
Cell 2 [Ah]	4.44	**4.51**
Cell 3 [Ah]	**3.23**	4.31

By using Eq. 5.1 and the peak values from the bulk ICF curve, Table 5.3 shows the estimated capacities and the resulting error between the estimated ($\hat{Q}$) and the measured ($\tilde{\mathrm{Q}}$) capacities of each cell. Results show that fixture 1, with the degraded cell, the estimation resulted in a 29% error between the measured and the estimated capacity for the degraded cell. The error on the other two cells was 5.6% and 5.4% respectively. For fixture 2, with the fresh cell, the estimation resulted in a 1.3% error between the measured and the estimated capacity for the fresh cell, while the error on the two other cells was 3.5% and 3.0% respectively.

Table 5.3: Estimated cell capacities for the two fixtures along with the error between the estimated and measured capacities for each cell using a 5 A discharge capacity test.

Cell Capacities	Fixture 1 Est. [Ah] / % Err.	Fixture 2 Est. [Ah] / % Err.
Cell 1	$4.22/5.6\%$	$4.46/3.5\%$
Cell 2	$4.20/5.4\%$	**4.45/1.3%**
Cell 3	**4.17/29%**	$4.44/3.0\%$

To better understand why the estimation error is large on the fixture with the degraded cell, a separate experiment was performed, whereas each cell in fixture 1 was discharged separately using a 3 A current while the other two were kept fully charged (at 100% SOC). The results from this experiment are shown in Fig. 5.10. Subplot 1 in Fig. 5.10 shows the resulting force measurements as a function of discharge capacity [Ah] for all 3 cells. It is clear that the degraded cell (cell#3) exhibits a different force shape than the other two cells, which have similar force curves. Subplot 2 shows the resulting individual dF_i/dQ (where $i = 1, 2, 3$) curves as a function of discharge capacity [Ah]. The calculated bulk $d\bar{F}_b/dQ$ curve is also shown in a solid black line. This curve is obtained by summing the individual dF_i/dQ curves of all 3 cells ($d\bar{F}_b/dQ = \sum_{i=1}^{3} dF_i/dQ$). In comparison, an experimental bulk dF_b/dQ curve is also plotted in dashed black line. This curve was obtained by discharging all cells together using a 3 A discharge current. Interestingly, the $d\bar{F}_b/dQ$ curve which was calculated from the individual dF_i/dQ curves and the experimental dF_b/dQ curve obtained by discharging all cells together exhibit the same shape but are scaled differently. This is because in the case where each cell is discharged separately, two cells are held at 100% SOC when the third cell is discharged, while in the case when all cells are discharged together, the SOCs change simultaneously, resulting in a differently scaled bulk dF_b/dQ curve.

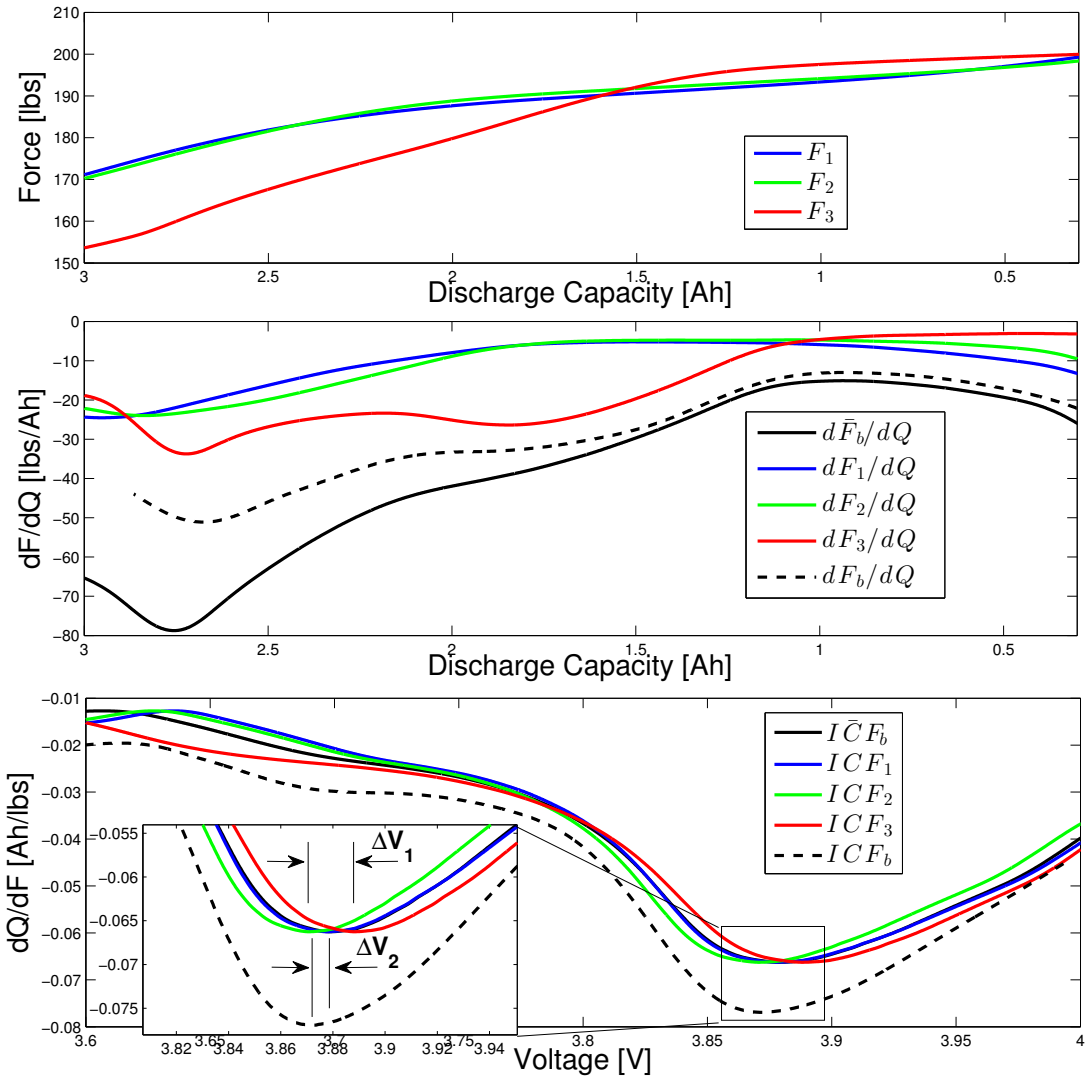

Figure 5.10: Plots of corresponding force, dF_i/dQ and ICF_i curves for the cells in fixture 1 using a 3 A discharge current. Also shown is the calculated bulk $d\bar{F}_b/dQ$ and $I\bar{C}F_b$ curves and a comparison with the experimental bulk dF_b/dQ and ICF_b curves when all cells are discharged simultaneously using a 3 A current.

Finally, the $d\bar{F}_b/dQ$ curve which was calculated from the individual dF_i/dQ curves can be inverted to form the bulk calculated ICF curve ($I\bar{C}F_b$). The $I\bar{C}F_b$ curve is plotted against the mean voltage of the cells in the fixture. The mean voltage is calculated by taking the mean of each cell voltage at the same discharge capacity. In comparison, the experimental ICF_b curve is also shown. This curve is obtained by inverting the dF_b/dQ curve in subplot 2 and it is also plotted against the mean voltage of the cells in the fixture. Finally, the individual ICF_i curves are also plotted. Note that the ICF_i curves are

obtained by plotting the $I\bar{C}F_b$ curve against individual cell voltages, and not by inverting the individual dF_i/dQ curves. The reason for doing so, is that in a battery pack, only the bulk force can be measured and not the individual force responses of each cell. There are several takeaways from subplot 3:

1. The maximum voltage difference between the peaks of the ICF_i curves is $\Delta V_1 = 17.4\ mV$. This corresponds to 9.2 mAh difference in capacity. This is why the estimated capacities of fixture 1 in Table 5.3 are so close to each other although the actual capacities, shown in Table 5.2, are not.

2. The difference in the peak voltage between the $I\bar{C}F_b$ curve and the experimental ICF_b curve is $\Delta V_2 = 6.2\ mV$. This indicates that the experimental bulk ICF curve is actually the result of the individual cell force curves being smeared together.

3. For the sake of comparison, and if we assume that the individual force responses of each cell are available (which is not a practical case), one can invert the dF_i/dQ curves for each cell and plot against their corresponding voltage (instead of plotting the $I\bar{C}F_b$ curve against individual voltages as shown in subplot 3 of Fig. 5.10). By identifying the voltage at the location of the peak of these ICF curves, and by using Eq. 5.1, the resulting estimated capacities of fixture 1 are shown in Table 5.4. Results show that, for Cell 1 and Cell 2, the estimation error is 2.9% and 0.9% respectively, while that for Cell 3 is 12%. This leads to two important points that need further investigation. One is the dependance of the locations of the ICF peaks on C-rate. Since the identification of parameter α_{avg} was done using 5 A discharge current experiments, while the experiment of Fig. 5.10 was done using a 3 A discharge current, the estimation results could be erroneous. This dependance will be investigated in Sec. 5.3.4 below. The second point is the adequacy of a linear fit. The estimation is not accurate for cell 3 which has degraded by 30%. This could mean that the degradation mechanism could follow a higher order fit instead of a linear one. This is to be investigated in future work.

Table 5.4: Estimated cell capacities for fixture 1 along with the error between the estimated and measured capacities for each cell using a 3 A discharge capacity test.

Cell Capacities	Fixture 1
	Actual [Ah] / Est. [Ah] / % Err.
Cell 1	$4.47/4.60/2.9\%$
Cell 2	$4.44/4.48/0.9\%$
Cell 3	**3.23/3.62/12%**

Thus, the large error in capacity estimation for fixture 1 shown in Table 5.3 is due to the individual dF_i/dQ curves being smeared into one bulk $d\bar{F}_b/dQ$ curve for which the resulting $I\bar{C}F_b$ curve has a peak that represents some weighted average of the capacities. In fact, the individual dF_i/dQ curves and their resulting ICF curves could be used to estimate the individual cell capacities as shown in Table 5.4. Unfortunately, this is not a practical case since in a pack one does not have access to the individual force response of every cell.

5.3.4 C-rate dependance

The capacity calculation experiments performed throughout this chapter were using moderate C-rates (5 A and 3 A). To investigate the effect of C-rate on the behavior of the dF/dQ curves, another capacity calculation experiment is performed using a C/3 current rate on one of the 3 cell fixtures. By following the same procedure as before, one could extract the ICF and ICV curves for both C-rates. Figure 5.11 shows the ICV and ICF curves for the two different C-rates. The ICF curves exhibit the same behavior as the ICV curves, with the peaks shifting as the C-rate increases. This means that as the C-rate increases from C/3 to 1 C, there is a shift in the peak locations of the ICF curves.

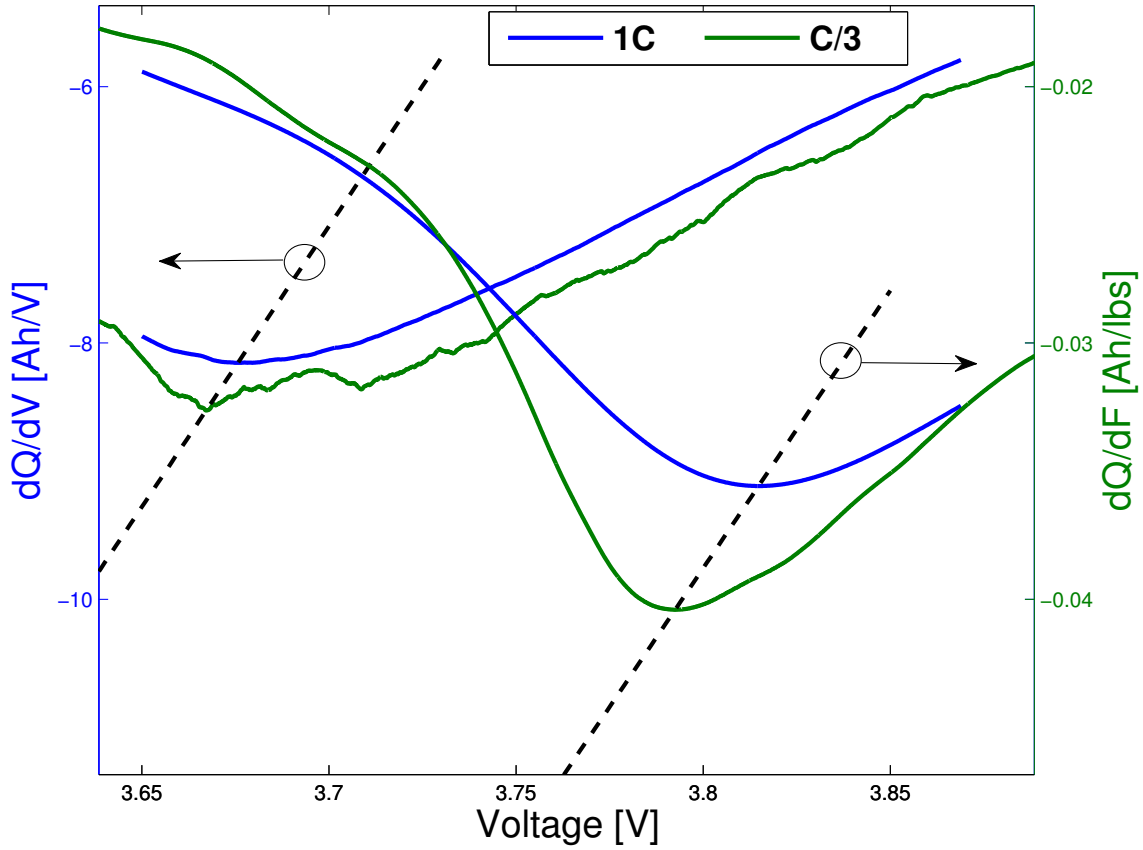

Figure 5.11: ICF and ICV curves as a function 1C and C/3 rate.

The authors in [112], however, indicate that the positions of the transition of the peaks of the $d^2\epsilon/dQ^2$ curves do not change significantly for C-rates of up to C/2. To compare the behavior of force with that of strain [112], another separate experiment was conducted, where two discharge tests were applied to the same cell. The first was a C/3 discharge current while the second was a C/20 discharge current. Figure 5.12 shows the ICF curves for both C-rates. Interestingly, the results show that for lower C-rates between C/3 and C/20, the peak locations do not shift significantly. The shift is around 3 mV which corresponds to 16 mAh in capacity estimation (or equivalently 0.4% error). Thus, the ICF method seems to follow the same behavior shown in [112], where the peaks do not shift significantly for C-rates up to C/3. However, at higher C-rates (1 C and above), the peaks appear to start shifting as was shown in Fig. 5.11. The behavior of the ICF peaks needs further investigation at higher C-rates, since there could be a thermal swelling in addition to a dynamic intercalation-based swelling effect in the cell, which could affect the force.

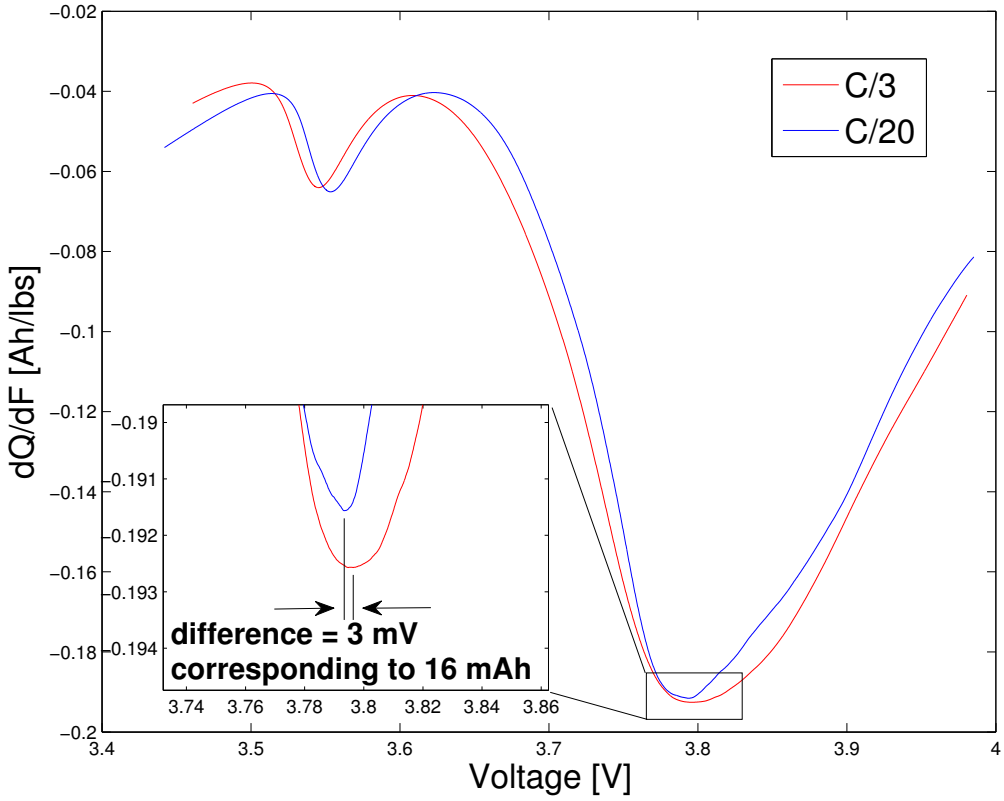

Figure 5.12: ICF curves as a function of C/3 and C/20 rate.

5.3.5 Charge behavior

The analysis in the previous sections was done during a constant discharge current. In a PHEV or an EV, it is more desirable to have the capacity estimation performed during charge. This is because the discharge behavior is very dynamic while the charge one is usually a constant one. Discharging the cells in a PHEV or an EV depends on the driving pattern while charging is only done by connecting the cells into a power source. Thus to investigate whether the cells exhibit the same ICF behavior in charge and discharge, two charge/discharge experiments were performed on two different cells with different degraded capacities. Cell 1 has a capacity of 4.47 Ah (new cell) while cell 2 has a capacity of 3.23 Ah (degraded cell). Both discharging and charging experiments were performed using a C/3 constant current. The results are shown in Fig. 5.13 and 5.14.

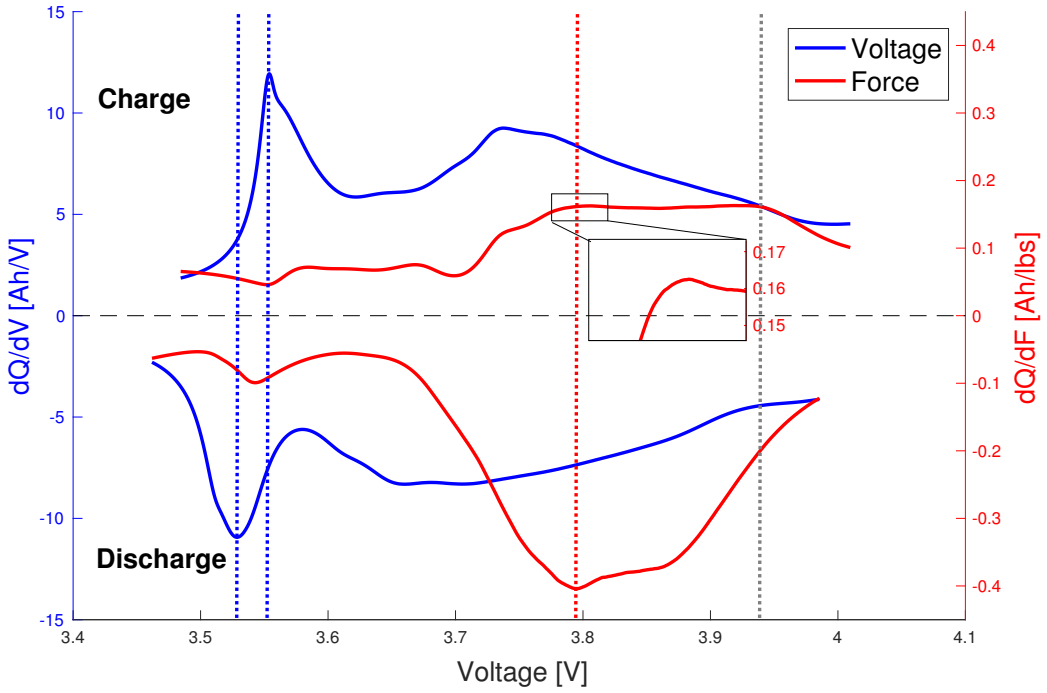

Figure 5.13: C/3 constant current charge and discharge ICV and ICF curves for a new cell (capacity = 4.47 Ah).

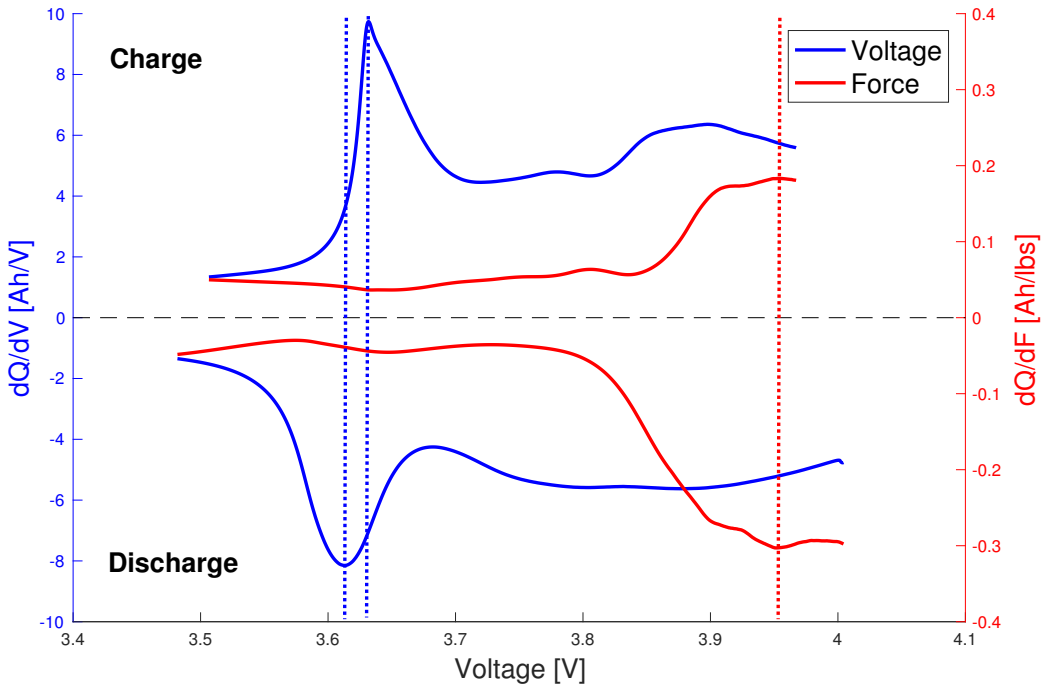

Figure 5.14: C/3 constant current charge and discharge ICV and ICF curves for a degraded cell (capacity = 3.23 Ah).

There are two main takeaways from the data shown in Fig. 5.13 and 5.14:

- In both cells, the charge and discharge ICV peaks do not have the same value. In the charge case, the ICV peak is at a higher voltage than the ICV peak in the discharge case. In the ICF case, however, both peaks in the charge and discharge case align. The ICF peaks during charge, however, are less distinct.
- In the charge case, and in the case of the new cell in Fig. 5.13, there seems to be another peak in the ICF curve which occurs at at even higher voltage (around 3.95 V shown in dotted grey line). This phenomena needs further investigation during the charging case.

Although the ICV peaks in charge and discharge do not match, initial results indicate that in the ICF case, these peaks are matching. However, further research and analysis is needed in the charging case to investigate whether the ICF peaks in the charing case follow the same trend as the discharging case as the cell degrades. In the discharging case, the ICF peaks moved to higher voltage as the cell degraded. The same procedure would have to be repeated to parameterize the degradation model in charge similarly to the discharging case

as shown in Figs. 5.3 through 5.6 and using Eq. 5.2 for capacity estimation. Also, more work is needed to understand the ICF behavior in charging, especially at high voltage, where the cell shows another ICF peak.

5.4 Conclusion

A novel method of using force in the incremental capacity analysis has been introduced. The method shows promising results since it could be used in tandem or instead of the ICV method where the differentiation of voltage with respect to capacity can result in low single to noise ratios. Also, it is able to monitor and estimate capacity fade of a battery at higher SOCs as compared to using ICV method. This means that the stack does not have to operate at low SOCs to get an estimation of the capacity fade. For an NMC cell, results using the ICF method have shown that the peaks of the dQ/dF versus V curves occur at around 70% SOC while those using the ICV method occur at around 40% SOC. Also, 4 different fixtures were tested under different SOC and preloading conditions. All fixtures seem to exhibit similar behavior with a linear decrease of capacity with increasing ICF peak voltage value. Results show that the mean capacity of each fixture can be estimated with a maximum error of 2.5% over 95000 miles of cycling. Also, it has been shown that bulk force measurements can be used to estimate individual cell capacities. Results show that the maximum error is 3.1% with an absolute mean and standard deviation on the error of 0.42% and 1.14% respectively. However, more data and further investigation is required to study the adequacy of a linear fit. Results also showed that the above proposed method can work for estimating individual cell capacities if they are closely balanced. However as the cells drift apart in capacity (results shown here for cells that have 27% difference in capacity), the method cannot estimate individual cell capacities. Finally, the dependance of the ICF curves on C-rate is shown for different C-rates. For C-rates up to C/3, the shift in the ICF curve peaks is minimal which agrees with the strain behavior in [112]. However, at higher C-rates (1 C-rate), the peaks start to shift. Finally, some preliminary work has been done on comparing the charging and discharging behavior of the ICV and ICF curve peaks for two cells with different capacities. It is shown that although the ICV peaks do not align, the peaks in the ICF cases align. The ICF peak during charging is less pronounced and possibly harder to detect. More investigation is required during charging and discharging to determine the applicability of the ICF method in charging as there seems to be another prominent peak located at the higher voltages. Future work would also include investigating the sensitivity of the ICF curves to the applied C-rate, and implementing this estimation method in on-board state of health monitoring prognostic algorithms.

CHAPTER 6

Conclusions and future work

6.1 Conclusions

This thesis has focused on utilizing state of the art sensing technologies for better battery state estimation, in an effort to decrease pack costs while maintaining performance. The techniques involved using novel thin film temperature sensors that could be embedded between the cells. This would allow more accurate and faster temperature estimation of the core temperatures of the cells. Also, force measurements were used in incremental capacity analysis for a supplementary or even complimentary method of estimating state of health or capacity fade of a battery. In conclusion, the main contributions of this thesis are summarized below.

A method for coupling the parameterization of an electro-thermal model with a high fidelity finite element model flow model was developed [31, 32]. In a battery pack where complex geometries affect airflow, it is very hard to parameterize the flow parameters and associated convection of an electro-thermal pack model. However, by coupling the parameterization of the heat generation with a finite element flow model, an accurate parameterization of the electro-thermal model can be obtained.

The electro-thermal model was validated against a wide range of operating conditions utilizing new temperature sensor technologies that enable measurement of the surface temperature of cells while operating. This allows for temperature validation of distributed thermal models over the surface of the cell. Validation is done against different nominal SOCs, ambient temperatures, current amplitudes and pulse widths.

A method for choosing the optimal sensor location on the surface of a cell [33] was developed. Conventional temperature sensors are placed near the tabs of the cells in a battery pack given the physical constraints. However, with the use of new thin film temperature sensors, the temperature at the surface locations can be measured. Thus a variation of the eigenmode projection method presented by Lim et al. [27] is developed to allow for the best thermal estimation of the core nodes of a jelly roll inside the battery.

A power management strategy that takes into account the electrical and thermal constraints of a battery is applied at a pack level. The results show that pack size can be decreased by more than 15% while shifting the operating SOC window [35]. This would result in minimal capacity fade increase (less than 1%) for the same pack energy throughput at the end of life. The downsizing of the pack also results in a 10% decrease in costs.

A novel method of using force measurements for estimating capacity fade is shown [30]. This method relies on the incremental capacity analysis. However instead of using voltage, the method relies on the force measurements during the operation of a battery. For an NMC cell, the capacity fade estimation using the incremental capacity analysis using voltage happens around the 40% of state of charge, while that using force measurements happens around the 70% of state of charge. This means that this can be used more often in an electric vehicle (EV) or plug-in hybrid electric vehicle (PHEV), which would result in better capacity estimation. Also, this method can result in individual cell capacity estimates with an absolute mean and standard deviation on the error of 0.42% and 1.14% respectively between the measured and estimated capacities. The method is shown to be insensitive to the applied C-rate for C-rates less than C/3. Furthermore, preliminary results show that estimation can be done around the same SOC in both the charging and discharging cases.

6.2 Future work

The work done throughout this thesis can be expanded upon for future work. First, more work could be done on the optimal sensor placement problem in the pack. Second and more importantly, a fully coupled electro-thermal mechanical model for a pack could be formulated that could be used for better state estimation. The results shown above regarding a model based power limiting algorithm that could potentially lead to a downsized pack can be applied in a supervisory HEV controller to study the potential change in the effective miles per gallon in the vehicle. Finally, further investigation is required into analyzing the behavior of the ICF method in estimating capacity in a charging mode, and looking at the dependance of the ICF curves to the applied C-rate.

6.2.1 Optimal sensor placement in pack

The optimal sensor locations have been looked at using two methods using the observability and observability gramian matrix of the system. However, more attention and work is needed for understanding why different methods result in different sensor locations. The work done in [120] is an important step towards this goal and will be used as a basis, among

other approaches, to look at the optimal sensor placement. This is important in understanding where the sensors should be placed and how many sensors are needed to sufficiently be able to estimate the battery dynamics.

6.2.2 Coupled Electro-thermal mechanical pack model

A fully coupled electro-thermal mechanical model that couples the electrical, thermal and mechanical behavior of a pack could be constructed. The model will utilize measurements of force in addition to the traditional temperature, current and voltage measurements to better estimate the states in the pack cells. Some significant work has been done towards that direction. The authors in [114, 121] develop phenomenological force and swelling models that can predict the thermal and intercalation force and swelling of Lithium-ion batteries when cycled. A coupled electro-thermal mechanical model was developed in [122] that was able to capture the force response under transient and dynamic cycling of cells in a constrained fixture. Thus future work could look at adopting coupled electro-thermal mechanical models for battery packs that can be used for better state of charge estimation [29] and capacity fade estimation [30].

6.2.3 Supervisory HEV controller

The work in this thesis has shown that a battery pack could potentially be downsized when a model based power limiting algorithm is utilized. A validated pack electro-thermal model and a capacity fading model were used to predict state changes and capacity fade at the end of life of a battery. Given that, when downsized, the battery pack cost could be reduced by 10%, it would be interesting to investigate the effect this downsizing has on the overall miles per gallon rating of the considered vehicle. For such a purpose, a supervisory controller is needed to optimize the power split between the battery pack and the engine.

6.2.4 Further work into ICF method

Preliminary results using the ICF method reveal that the method is indeed C-rate independent for low C-rates of less than C/3. However, as the C-rate increases the peaks of the ICF curves start shifting. Future research could investigate this phenomena and identify the root causes; whether the variability is due to temperature or mechanical issue that is C-rate dependent. Also, it has been shown that, unlike the ICV curves which have different peaks in charge and discharge, the ICF peaks are almost exactly at the same location but are less pronounced. More investigation and analysis is required to understand this behavior and

whether the ICF peaks in charging follow the same trend as they do in the discharging case. Finally, it is shown that in the charging case, there exists another prominent ICF peak at high voltage that would require further analysis into whether it is a consistent phenomenon as the cell degrades.

APPENDIX A

Degradation Experiments

A.1 US06 cycling

A charge sustaining current cycle was applied and repeated for 450 times continuously to the cells. The applied cycle is a high power cycle from a HEV operating on a US06 cycle. The current profile is applied throughout a two stage degradation experiment. Table A.1 shows the important features of the current profile for both stages of the degradation experiments. Details of the aging procedure follows:

- Set thermal chamber ambient temperature to 25°C.
- Charge all cells at 5 A (1 C-rate) using a constant-current constant-voltage (CCCV) protocol to 4.1 V (corresponding to 100% SOC), until the current reaches 0.05 A.
- Discharge fixtures 1 through 4 to $\{33, 50, 66, 50\}$ % SOCs for the first stage of degradation experiments (first 3500 cycles) and to $\{40, 50, 60, 50\}$ % for the second stage of degradation experiments (next 2700 cycles) when current increases by a factor of 1.3.
- Set thermal chamber ambient temperature to 10°C for first stage of degradation experiments and to 25°C for the second stage.
- Rest for one day.
- Apply the current profile detailed in Table A.1 for 450 cycles. In the first state of degradation experiments the current is not scaled. During the second stage, the current is scaled by a factor of 1.3.
- Proceed to capacity calculations (refer to App. A.2).

The US06 cycle profile is shown in fig. A.1 below. Also table A.1 shows the important features of the current profile for the degradation experiments.

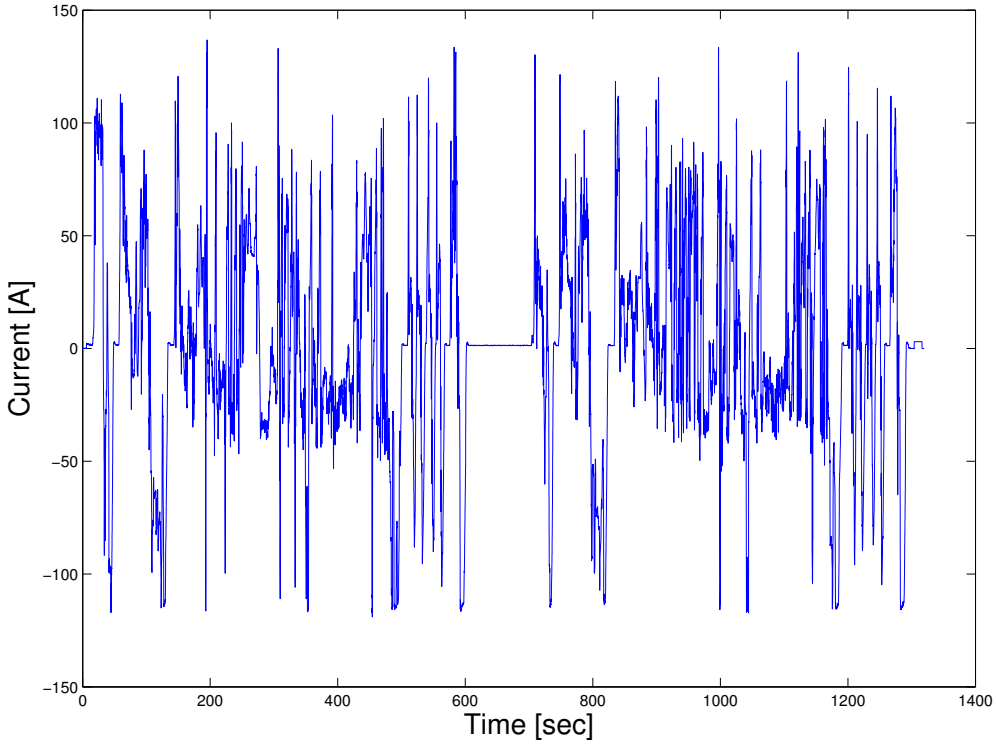

Figure A.1: US06 current profile used for the degradation experiments.

Table A.1: Current profile features during first and second stage experiments.

	First Stage	Second Stage
Duration [sec]	1320	1320
RMS current [A]	45	60
Max |Current| [A]	137	178
Max |ΔCurrent| [A]	84	109
Max SOC swing [%]	20	26

A.2 Capacity measurements

After the fixtures have been cycled with the current profile (details in Table A.1) for 450 times, a capacity calculation routine is done for all cells according to the following

procedure:

- Charge all cells with a 5 A (1 C-rate) using a constant-current constant-voltage (CCCV) protocol to 4.1 V (corresponding to 100% SOC), until the current reaches 0.05 A.
- Set thermal chamber ambient temperature to 25°C
- Rest for one day at the fully charged state at 25°C.
- Discharge all cells at 1C (5 A) rate to 2.9 v (corresponding to 0% SOC).
- Record discharging capacity of each cell. Also, the capacity of each fixture is the mean capacity of all 3 cells in the fixture.
- Proceed to current cycling.

APPENDIX B

Pulse Power Capability Computation

In determining model-based power capability, voltage and SOC constraints are considered independently based on time-scale separation. The model-based power capability is typically determined by computing limiting current and projected terminal voltage to avoid computational burden. To solve each constraint problem, a simple method described in [41] is adopted to compute the maximum current ensuring that no constraints are violated. This method is based on iteration and inversion of a dynamic model by receding horizon scheme as illustrated in Fig. B.1.

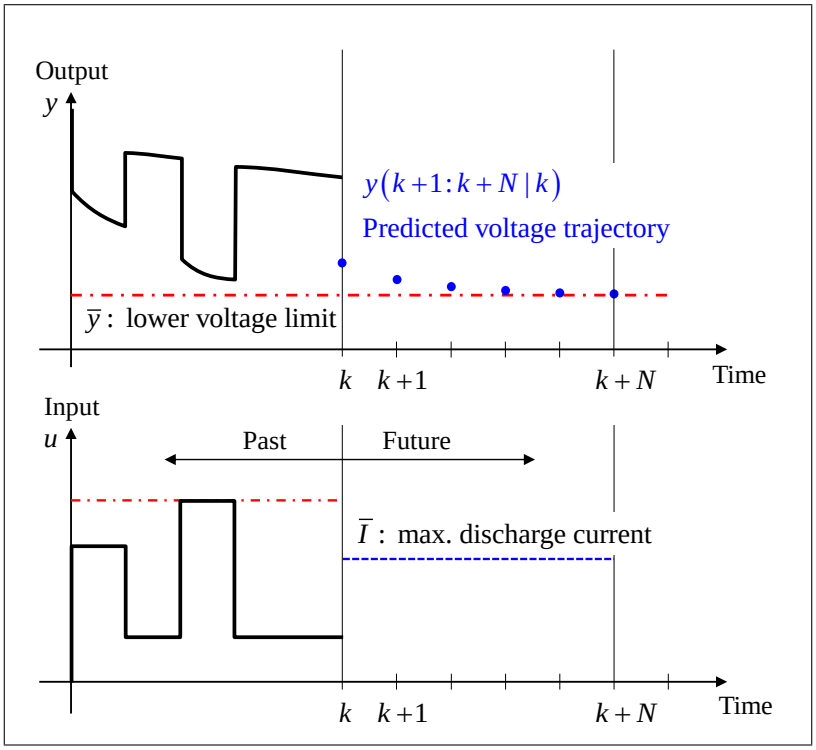

Figure B.1: A Schematic of computing power capability of a battery

Consider a linearized discrete-time electrical model whose dynamics are described by

the following set of difference equations

$$x_{k+1} = Ax_k + BI_k + E,$$
$$y_k = Cx_k + DI_k + F,$$

where system matrices associated with the output, y, are denoted by A, B, C, D, E and F[1]. For a constant current input $\bar{I}$, the state x and output y after N future steps are given by

$$x_{k+N} = A^N x_k + \sum_{i=0}^{N-1} A^i B\bar{I} + \sum_{i=0}^{N-1} A^i E,$$
$$y_{k+N} = Cx_{k+N} + D\bar{I} + F.$$

Therefore, at any instant k, the maximum permissible current that does not violate a constraint $\bar{y}$ on the output y in N future steps is determined by

$$\bar{I} = \left(\sum_{i=0}^{N-1} CA^i B + D \right)^{-1} \left(\bar{y} - CA^N x_k - \sum_{i=0}^{N-1} CA^i E - F \right).$$

For more detailed description about the method including how to handle nonlinearities in thermal dynamics, the interested reader is referred to [41]. In this study, terminal voltage and SOC are chosen as constraint parameters, i.e. $\bar{y} \in \{V_{\min}, V_{\max}, \text{SOC}_{\min}, \text{SOC}_{\max}\}$.

[1]Matrices for the electrical system are obtained through linearization and discretization processes around the operating point at each sampling time

APPENDIX C

Savitsky-Golay (SG) filter

The SG filter fits to successive sets of data a low order polynomial using least squares method, and can improve the signal to noise ratio without affecting or distorting the signal. The SG filter requires the window or frame length (F) and the polynomial order (n) to be specified. Since the sampling rate is 1 Hz, this would mean that F also represents the number of data points or samples. For a nice filtering effect, n has to be considerably smaller than F, otherwise the fitted data is being interpolated to the noisy data. Figure C.1 shows a plot of the force and the derivative of force with respect to discharge capacity for different frame lengths (F) and for $n = 3$. Notice that although, the force fit seems to be similar using the 3 different frame lengths, the resulting dF/dQ is different. For a short frame length, the derivative curve exhibits a lot of oscillations indicating that the curve is being fit to noise and is not being filtered. As the frame length increases, the derivative curve becomes smoother.

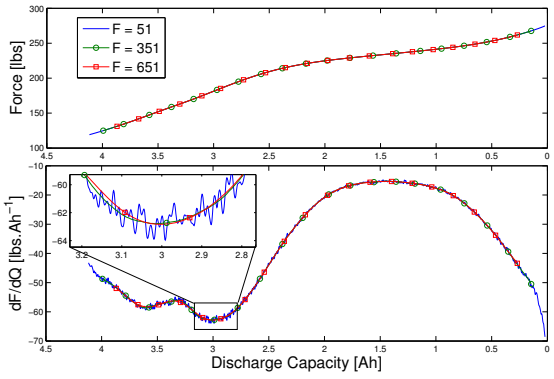

Figure C.1: Force and dF/dQ curve fits using SG filter during 1C discharge capacity test for fixture 1 after $N = 325$ cycles for polynomial order $n = 3$ and different frame lengths (F).

BIBLIOGRAPHY

[1] BP, "Statistical Review of World Energy," 2015, Retrieved on 03/11/2016 from http://www.bp.com/en/global/corporate/energy-economics/statistical-review-of-world-energy.html.

[2] Administration, U. E. I., "How much carbon dioxide is produced when different fuels are burned?" June 2015, Retrieved on 03/11/2016 from http://www.eia.gov/tools/faqs/faq.cfm?id=73&t=11.

[3] Administration, U. E. I., "International Energy Statistics," 2012, Retrieved on 03/11/2016 from http://www.eia.gov/cfapps/ipdbproject/IEDIndex3.cfm?tid=1&pid=1&aid=2.

[4] Administration, U. E. I., "Petroleum & Other Liquids - Refinery Yield," March 2016, Retrieved on 03/11/2016 from http://www.eia.gov/dnav/pet/pet_pnp_pct_dc_nus_pct_a.htm.

[5] Petit, J. R., Jouzel, J., Raynaud, D., Barkov, N. I., Barnola, J.-M., Basile, I., Bender, M., Chappellaz, J., Davis, M., Delaygue, G., Delmotte, M., Kotlyakov, V. M., Legrand, M., Lipenkov, V. Y., Lorius, C., PÉpin, L., Ritz, C., Saltzman, E., and Stievenard, M., "Climate and atmospheric history of the past 420,000 years from the Vostok ice core, Antarctica," *Nature*, Vol. 399, No. 6735, jun 1999, pp. 429–436.

[6] Griggs, D. J. and Noguer, M., "Climate change 2001: The scientific basis. Contribution of Working Group I to the Third Assessment Report of the Intergovernmental Panel on Climate Change," *Weather*, Vol. 57, No. 8, 2002, pp. 267–269.

[7] Center, N. C. D., "Glacial-Interglacial cycles," 2008, Retrieved on 03/11/2016 from http://www.ncdc.noaa.gov/paleo/abrupt/data2.html.

[8] Laboratory, L. L. N., "Estimated U.S. Energy Use in 2014," 2015, Retrieved on 03/11/2016 from https://flowcharts.llnl.gov/content/assets/images/energy/us/Energy_US_2014.png.

[9] fr Sonnenenergie-und Wasserstoff-Forschung Baden-Wrttemberg, Z., "Number of electric cars worldwide climbs to 1.3 million," February 2016, Retrieved on 03/11/2016 from http://www.zsw-bw.de/uploads/media/pr05-2016-ZSW-DataE-Mobility.pdf.

[10] of Concerned Scientists, U., "State of Charge (2012)," September 2014, Retrieved on 03/11/2016 from http://www.ucsusa.org/sites/default/files/legacy/assets/documents/clean_vehicles/electric-car-global-warming-emissions-exec-summary.pdf.

[11] Tesla, "Tesla Model S Achieves Best Safety Rating of Any Car Ever Tested," August 2013, Retrieved on 03/11/2016 from https://www.teslamotors.com/blog/tesla-model-s-achieves-best-safety-rating-any-car-ever-tested.

[12] Wakihara, M. and Yamamoto, O., *Lithium Ion Batteries: Fundamentals and Performance*, Wiley, 2008.

[13] Jiang, J. and Zhang, C., *Fundamentals and Applications of Lithium-ion Batteries in Electric Drive Vehicles*, Wiley-Blackwell, may 2015.

[14] Mandal, B. K., Padhi, A. K., Shi, Z., Chakraborty, S., and Filler, R., "Thermal runaway inhibitors for lithium battery electrolytes," *Journal of Power Sources*, Vol. 161, No. 2, 2006, pp. 1341 – 1345.

[15] Sarre, G., Blanchard, P., and Broussely, M., "Aging of lithium-ion batteries," *Journal of Power Sources*, Vol. 127, No. 12, 2004, pp. 65 – 71, Eighth Ulmer Electrochemische Tage.

[16] Vetter, J., Novk, P., Wagner, M., Veit, C., Mller, K.-C., Besenhard, J., Winter, M., Wohlfahrt-Mehrens, M., Vogler, C., and Hammouche, A., "Ageing mechanisms in lithium-ion batteries," *Journal of Power Sources*, Vol. 147, No. 12, 2005, pp. 269 – 281.

[17] Broussely, M., Biensan, P., Bonhomme, F., Blanchard, P., Herreyre, S., Nechev, K., and Staniewicz, R., "Main aging mechanisms in Li ion batteries," *Journal of Power Sources*, Vol. 146, No. 12, 2005, pp. 90 – 96.

[18] Chiang, Y.-H., Sean, W.-Y., and Ke, J.-C., "Online estimation of internal resistance and open-circuit voltage of lithium-ion batteries in electric vehicles," *Journal of Power Sources*, Vol. 196, No. 8, 2011, pp. 3921 – 3932.

[19] Eddahech, A., Briat, O., Bertrand, N., Deletage, J.-Y., and Vinassa, J.-M., "Behavior and state-of-health monitoring of Li-ion batteries using impedance spectroscopy and recurrent neural networks," *International Journal of Electrical Power & Energy Systems*, Vol. 42, No. 1, 2012, pp. 487 – 494.

[20] Han, X., Ouyang, M., Lu, L., and Li, J., "A comparative study of commercial lithium ion battery cycle life in electric vehicle: Capacity loss estimation," *Journal of Power Sources*, Vol. 268, 2014, pp. 658 – 669.

[21] Eddahech, A., Briat, O., and Vinassa, J.-M., "Determination of lithium-ion battery state-of-health based on constant-voltage charge phase," *Journal of Power Sources*, Vol. 258, 2014, pp. 218 – 227.

[22] Weng, C., Cui, Y., Sun, J., and Peng, H., "On-board state of health monitoring of lithium-ion batteries using incremental capacity analysis with support vector regression," *Journal of Power Sources*, Vol. 235, 2013, pp. 36 – 44.

[23] Group, S. E., *Instrumental Methods in Electrochemistry (Ellis Horwood series in physical chemistry)*, Ellis Horwood Ltd , Publisher, 1985.

[24] Feng, X., Li, J., Ouyang, M., Lu, L., Li, J., and He, X., "Using probability density function to evaluate the state of health of lithium-ion batteries," *Journal of Power Sources*, Vol. 232, 2013, pp. 209 – 218.

[25] Dunn, B., Kamath, H., and Tarascon, J.-M., "Electrical Energy Storage for the Grid: A Battery of Choices," *Science*, Vol. 334, No. 6058, nov 2011, pp. 928–935.

[26] Kim, C.-G., Seo, D.-H., You, J.-S., Park, J.-H., and Cho, B., "Design of a contactless battery charger for cellular phone," *Industrial Electronics, IEEE Transactions on*, Vol. 48, No. 6, Dec 2001, pp. 1238–1247.

[27] Lim, K. B., "Method for optimal actuator and sensor placement for large flexible structures," *Journal of Guidance, Control, and Dynamics*, Vol. 15, No. 1, Jan. 1992, pp. 49–57.

[28] Mohan, S., Kim, Y., Siegel, J. B., Samad, N. A., and Stefanopoulou, A. G., "A Phenomenological Model of Bulk Force in a Li-Ion Battery Pack and Its Application to State of Charge Estimation," *Journal of The Electrochemical Society*, Vol. 161, No. 14, 2014, pp. A2222–A2231.

[29] Mohan, S., Kim, Y., and Stefanopoulou, A. G., "On improving battery state of charge estimation using bulk force measurements," in ASME 2015 Dynamic Systems and Control Conference.

[30] Samad, N. A., Kim, Y., Siegel, J. B., and Stefanopoulou, A. G., "Battery Capacity Fading Estimation Using a Force-based Incremental Capacity Analysis," submitted to Journal of The Electrochemical Society, 2016.

[31] Samad, N. A., Siegel, J. B., and Stefanopoulou, A. G., "Parameterization and validation of a distributed coupled electro-thermal model for prismatic cells," *2014 ASME Dynamic Systems and Control Conference*, 2014.

[32] Samad, N. A., Wang, B., Siegel, J. B., and Stefanopoulou, A. G., "Scalable Dynamic Battery Electro-thermal Models: Cascading Parameterization In a Flexible Fidelity Software," submitted to the Journal of Dynamic Systems, Measurement and Control, 2016.

[33] Samad, N., Siegel, J., Stefanopoulou, A., and Knobloch, A., "Observability analysis for surface sensor location in encased battery cells," *American Control Conference (ACC), 2015*, July 2015, pp. 299–304.

[34] Samad, N., Kim, Y., Siegel, J., and Stefanopoulou, A., "Influence of Battery Downsizing and SOC Operating Window on Battery Pack Performance in a Hybrid Electric Vehicle," *Vehicle Power and Propulsion Conference (VPPC), 2015 IEEE*, Oct 2015, pp. 1–6.

[35] Samad, N. A., Kim, Y., Siegel, J. B., Yoo, S., and Stefanopoulou, A. G., "Power denials after downsizing a battery pack & shifting SOC range in a hybrid electric vehicle," submitted to IEEE Transactions on Vehicular Technology, 2016.

[36] Doyle, M., Fuller, T. F., and Newman, J., "Modeling of Galvanostatic Charge and Discharge of the Lithium/Polymer/Insertion Cell," *Journal of the Electrochemical Society*, Vol. 140, 1993.

[37] Fuller, T. F., Doyle, M., and Newman, J., "Simulation and Optimization of the Dual Lithium Ion Insertion Cell," *Journal of the Electrochemical Society*, Vol. 1, 1994.

[38] Safari, M., Morcrette, M., Teyssot, A., and Delacourta, C., "Multimodal Physics-Based Aging Model for Life Prediction of Li-Ion Batteries," *Journal of the Electrochemical Society*, Vol. 156, 2009.

[39] Lin, X., Perez, H. E., Siegel, J. B., Stefanopoulou, A. G., Li, Y., Anderson, R. D., Ding, Y., and Castanier, M. P., "Online Parameterization of Lumped Thermal Dynamics in Cylindrical Lithium Ion Batteries for Core Temperature Estimation and Health Monitoring," *IEEE Transactions on Control System Technology, Accepted pending minor revisions*, 2013.

[40] Murashko, K., Pyrhonen, J., and Laurila, L., "Three-Dimensional Thermal Model of a Lithium Ion Battery for Hybrid Mobile Working Machines: Determination of the Model Parameters in a Pouch Cell," *Energy Conversion, IEEE Transactions on*, Vol. 28, No. 2, 2013, pp. 335–343.

[41] Kim, Y., Mohan, S., Siegel, J. B., and Stefanopoulou, A. G., "Maximum Power Estimation of Lithium-ion Batteries Accounting for Thermal and Electrical Constraints," *Proceedings of ASME Dynamic Systems Control Conference*, Palo Alto, California, USA, Oct 22-24 2013, p. V002T23A003.

[42] Gao, L., Liu, S., and Dougal, R., "Dynamic lithium-ion battery model for system simulation," *Components and Packaging Technologies, IEEE Transactions on*, Vol. 25, No. 3, Sep 2002, pp. 495–505.

[43] Perez, H. E., Siegel, J. B., Lin, X., Ding, Y., and Castanier, M. P., "Parameterization and Validation of an Integrated Electro-Thermal LFP Battery Model," *2012 ASME Dynamic Systems Control Conference, Oct 2012*, 2012.

[44] Smith, K., Kim, G.-H., Darcy, E., and Pesaran, A., "Thermal/electrical modeling for abuse-tolerant design of lithium ion modules," *International Journal of Energy Research*, Vol. 34, 2010, pp. 204–215.

[45] Jung, S. and Kang, D., "Multi-dimensional modeling of large-scale lithium-ion batteries," *Journal of Power Sources*, Vol. 248, No. 0, 2014, pp. 498 – 509.

[46] Fleckenstein, M., Bohlen, O., Roscher, M. A., and Bker, B., "Current density and state of charge inhomogeneities in Li-ion battery cells with LiFePO4 as cathode material due to temperature gradients," *Journal of Power Sources*, Vol. 196, No. 10, 2011, pp. 4769 – 4778.

[47] Taheri, P. and Bahrami, M., "Temperature Rise in Prismatic Polymer Lithium-Ion Batteries: An Analytic Approach," *SAE International*, Vol. 5, 2012.

[48] Chen, S., Wan, C., and Wang, Y., "Thermal analysis of lithium-ion batteries," *Journal of Power Sources*, Vol. 140, No. 1, 2005, pp. 111 – 124.

[49] Inui, Y., Kobayashi, Y., Watanabe, Y., Watase, Y., and Kitamura, Y., "Simulation of temperature distribution in cylindrical and prismatic lithium ion secondary batteries," *Energy Conversion and Management*, Vol. 48, No. 7, 2007, pp. 2103 – 2109.

[50] Samba, A., Omar, N., Gualous, H., Firouz, Y., den Bossche, P. V., Mierlo, J. V., and Boubekeur, T. I., "Development of an Advanced Two-Dimensional Thermal Model for Large size Lithium-ion Pouch Cells," *Electrochimica Acta*, Vol. 117, No. 0, 2014, pp. 246 – 254.

[51] Gerver, R. E. and Meyers, J. P., "Three-Dimensional Modeling of Electrochemical Performance and Heat Generation of Lithium-Ion Batteries in Tabbed Planar Configurations," *Journal of The Electrochemical Society*, Vol. 158, 2011, pp. A835 – A843.

[52] Maleki, H., Hallaj, S. A., Selman, J. R., Dinwiddie, R. B., and Wang, H., "Thermal Properties of Lithium-Ion Battery and Components," *Journal of The Electrochemical Society*, Vol. 146, 1999, pp. 947–954.

[53] Lin, X., Perez, H. E., Mohan, S., Siegel, J. B., Stefanopoulou, A. G., Ding, Y., and Castanier, M. P., "A lumped-parameter electro-thermal model for cylindrical batteries," *Journal of Power Sources*, Vol. 257, 2014, pp. 1 – 11.

[54] Hallaj, S. A., Prakash, J., and Selman, J., "Characterization of commercial Li-ion batteries using electrochemical-calorimetric measurements," *Journal of Power Sources*, Vol. 87, 2000, pp. 186 – 194.

[55] Incropera, F., *Fundamentals of heat and mass transfer*, John Wiley, Hoboken, NJ, 2007.

[56] Ramadass, P., Haran, B., White, R., and Popov, B. N., "Capacity fade of Sony 18650 cells cycled at elevated temperatures: Part I. Cycling performance," *Journal of Power Sources*, Vol. 112, No. 2, 2002, pp. 606 – 613.

[57] Wright, R., Christophersen, J., Motloch, C., Belt, J., Ho, C., Battaglia, V., Barnes, J., Duong, T., and Sutula, R., "Power fade and capacity fade resulting from cycle-life testing of Advanced Technology Development Program lithium-ion batteries," *Journal of Power Sources*, Vol. 119121, No. 0, 2003, pp. 865 – 869.

[58] Shim, J., Kostecki, R., Richardson, T., Song, X., and Striebel, K., "Electrochemical analysis for cycle performance and capacity fading of a lithium-ion battery cycled at elevated temperature," *Journal of Power Sources*, Vol. 112, No. 1, 2002, pp. 222 – 230.

[59] Armaou, A. and Demetriou, M. A., "Optimal actuator/sensor placement for linear parabolic {PDEs} using spatial norm," *Chemical Engineering Science*, Vol. 61, No. 22, 2006, pp. 7351 – 7367.

[60] Demetriou, M., "Numerical investigation on optimal actuator/sensor location of parabolic PDEs," *American Control Conference, 1999. Proceedings of the 1999*, Vol. 3, 1999, pp. 1722–1726 vol.3.

[61] Georges, D., "The use of observability and controllability gramians or functions for optimal sensor and actuator location in finite-dimensional systems," *Decision and Control, 1995., Proceedings of the 34th IEEE Conference on*, Vol. 4, Dec 1995, pp. 3319–3324 vol.4.

[62] Ng, J., Dubljevic, S., and Aksikas, I., "Aspects of controllability and observability for time-varying PDE systems," *American Control Conference (ACC), 2012*, June 2012, pp. 2220–2225.

[63] Halim, D. and Moheimani, S. R., "An optimization approach to optimal placement of collocated piezoelectric actuators and sensors on a thin plate," *Mechatronics*, Vol. 13, No. 1, 2003, pp. 27 – 47.

[64] Wolf, P., Moura, S., and Krstic, M., "On optimizing sensor placement for spatio-temporal temperature estimation in large battery packs." *CDC*, 2012, pp. 973–978.

[65] Fang, H., Sharma, R., and Patil, R., "Optimal sensor and actuator deployment for HVAC control system design," *American Control Conference (ACC), 2014*, June 2014, pp. 2240–2246.

[66] Kang, W., Xu, L., and Giraldo, F. X., "Partial Observability and its Consistency for PDEs," *ArXiv e-prints*, Dec. 2014.

[67] Fazel, M., Hindi, H., and Boyd, S., "Rank minimization and applications in system theory," *American Control Conference, 2004. Proceedings of the 2004*, Vol. 4, June 2004, pp. 3273–3278 vol.4.

[68] Franklin, G. F., Workman, M. L., and Powell, D., *Digital Control of Dynamic Systems*, Addison-Wesley Longman Publishing Co., Inc., Boston, MA, USA, 3rd ed., 1997.

[69] Ebbesen, S., Elbert, P., and Guzzella, L., "Engine downsizing and electric hybridization under consideration of cost and drivability," *Oil & Gas Science and Technology–Revue dIFP Energies nouvelles*, Vol. 68, No. 1, 2013, pp. 109–116.

[70] Tian, F., Ren, G., Zhang, S., and Yang, L., *Proceedings of the FISITA 2012 World Automotive Congress: Volume 2: Advanced Internal Combustion Engines (II)*, chap. Analysis and Simulation of Hybrid Electric Turbocharger and Application on ICE and HEV, Springer Berlin Heidelberg, Berlin, Heidelberg, 2013, pp. 1193–1200.

[71] Brooker, A., Ward, J., and Wang, L., "Lightweighting Impacts on Fuel Economy, Cost, and Component Losses," *SAE Technical Paper 2013-01-0381*, 2013.

[72] Silvas, E., Bergshoeff, E., Hofman, T., and Steinbuch, M., "Comparison of Bi-Level Optimization Frameworks for Sizing and Control of a Hybrid Electric Vehicle," *Vehicle Power and Propulsion Conference (VPPC), 2014 IEEE*, Oct 2014, pp. 1–6.

[73] Simmons, R. A., Shaver, G. M., Tyner, W. E., and Garimella, S. V., "A benefit-cost assessment of new vehicle technologies and fuel economy in the U.S. market," *Applied Energy*, Vol. 157, 2015, pp. 940 – 952.

[74] Anderson, R. D., Zhao, Y., Wang, X., Yang, X. G., and Li, Y., "Real time battery power capability estimation," *Proceedings of the American Control Conference*, June 2012, pp. 592–597.

[75] Perez, H., Shahmohammadhamedani, N., and Moura, S., "Enhanced Performance of Li-Ion Batteries via Modified Reference Governors and Electrochemical Models," *Mechatronics, IEEE/ASME Transactions on*, Vol. PP, No. 99, 2015, pp. 1–10.

[76] Mohan, S., Kim, Y., and Stefanopoulou, A., "Estimating the Power Capability of Li-ion Batteries Using Informationally Partitioned Estimators," *Control Systems Technology, IEEE Transactions on*, Vol. PP, No. 99, 2015, pp. 1–12.

[77] Ohzuku, T. and Brodd, R. J., "An overview of positive-electrode materials for advanced lithium-ion batteries," *Journal of Power Sources*, Vol. 174, No. 2, 2007, pp. 449 – 456, 13th International Meeting on Lithium Batteries.

[78] Croy, J. R., Abouimrane, A., and Zhang, Z., "Next-generation lithium-ion batteries: The promise of near-term advancements," *MRS Bulletin*, Vol. 39, 5 2014, pp. 407–415.

[79] Sundstrm, O. and Stefanopoulou, A., "Optimum Battery Size for Fuel Cell Hybrid Electric Vehicle— Part I," *Journal of Fuel Cell Science and Technology*, Vol. 4, No. 2, 2007, pp. 167.

[80] Cordoba-Arenas, A., Onori, S., Guezennec, Y., and Rizzoni, G., "Capacity and power fade cycle-life model for plug-in hybrid electric vehicle lithium-ion battery cells containing blended spinel and layered-oxide positive electrodes," *Journal of Power Sources*, Vol. 278, No. 0, 2015, pp. 473 – 483.

[81] Nelson, P. A. G., *Modeling the performance and cost of lithium-ion batteries for electric-drive vehicles.*, Oct 2011.

[82] Nelson, P., Vijayagopal, R., Gallagher, K., and Rousseau, A., "Sizing the battery power for PHEVs based on battery efficiency, cost and operational cost savings," *Electric Vehicle Symposium and Exhibition (EVS27), 2013 World*, Nov 2013, pp. 1–9.

[83] Patry, G., Romagny, A., Martinet, S., and Froelich, D., "Cost modeling of lithium-ion battery cells for automotive applications," *Energy Science & Engineering*, Vol. 3, No. 1, 2015, pp. 71–82.

[84] Sakti, A., Michalek, J. J., Fuchs, E. R., and Whitacre, J. F., "A techno-economic analysis and optimization of Li-ion batteries for light-duty passenger vehicle electrification," *Journal of Power Sources*, Vol. 273, 2015, pp. 966–980.

[85] Fox, R., *Introduction to fluid mechanics*, Wiley, New York, 2004.

[86] Van Den Berg, F., Hoefsloot, H., Boelens, H., and Smilde, A., "Selection of optimal sensor position in a tubular reactor using robust degree of observability criteria," *Chemical Engineering Science*, Vol. 55, No. 4, 2000, pp. 827–837, cited By 40.

[87] Waldraff, W., Dochain, D., Bourrel, S., and Magnus, A., "On the use of observability measures for sensor location in tubular reactor," *Journal of Process Control*, Vol. 8, No. 5-6, 1998, pp. 497–505, cited By 60.

[88] Serpas, M., Hackebeil, G., Laird, C., and Hahn, J., "Sensor location for nonlinear dynamic systems via observability analysis and MAX-DET optimization," *Computers & Chemical Engineering*, Vol. 48, 2013, pp. 105 – 112.

[89] Summers, T. H. and Lygeros, J., "Optimal sensor and actuator placement in complex dynamical networks," *arXiv preprint arXiv:1306.2491*, 2013.

[90] Kalman, R., "On the general theory of control systems," *IRE Transactions on Automatic Control*, Vol. 4, No. 3, 1959, pp. 110–110.

[91] Aylor, J., Thieme, A., and Johnson, B., "A Battery State-of-Charge Indicator for Electric Wheelchairs," *IEEE Transactions on Industrial Electronics*, Vol. 39, No. 5, 1992, pp. 398–409, cited By 117.

[92] Liu, T.-H., Chen, D.-F., and Fang, C.-C., "Design and implementation of a battery charger with a state-of-charge estimator," *International Journal of Electronics*, Vol. 87, No. 2, 2000, pp. 211–226, cited By 21.

[93] Piller, S., Perrin, M., and Jossen, A., "Methods for state-of-charge determination and their applications," *Journal of Power Sources*, Vol. 96, No. 1, 2001, pp. 113 – 120, Proceedings of the 22nd International Power Sources Symposium.

[94] Bo, C., Zhifeng, B., and Binggang, C., "State of charge estimation based on evolutionary neural network," *Energy conversion and management*, Vol. 49, No. 10, 2008, pp. 2788–2794.

[95] Hu, X., Sun, F., and Zou, Y., "Estimation of state of charge of a lithium-ion battery pack for electric vehicles using an adaptive Luenberger observer," *Energies*, Vol. 3, No. 9, 2010, pp. 1586–1603.

[96] Plett, G. L., "Extended Kalman filtering for battery management systems of LiPB-based HEV battery packs: Part 3. State and parameter estimation," *Journal of Power sources*, Vol. 134, No. 2, 2004, pp. 277–292.

[97] Junping, W., Jingang, G., and Lei, D., "An adaptive Kalman filtering based State of Charge combined estimator for electric vehicle battery pack," *Energy Conversion and Management*, Vol. 50, No. 12, 2009, pp. 3182–3186.

[98] Chen, Z., Qiu, S., Masrur, M. A., and Murphey, Y. L., "Battery state of charge estimation based on a combined model of extended Kalman filter and neural networks," *Neural Networks (IJCNN), The 2011 International Joint Conference on*, IEEE, 2011, pp. 2156–2163.

[99] Wang, J., Liu, P., Hicks-Garner, J., Sherman, E., Soukiazian, S., Verbrugge, M., Tataria, H., Musser, J., and Finamore, P., "Cycle-life model for graphite-LiFePO4 cells," *Journal of Power Sources*, Vol. 196, No. 8, 2011, pp. 3942 – 3948.

[100] Wang, J., Purewal, J., Liu, P., Hicks-Garner, J., Soukazian, S., Sherman, E., Sorenson, A., Vu, L., Tataria, H., and Verbrugge, M. W., "Degradation of lithium ion batteries employing graphite negatives and nickel-cobalt-manganese oxide + spinel manganese oxide positives: Part 1, aging mechanisms and life estimation," *Journal of Power Sources*, Vol. 269, No. 0, 2014, pp. 937 – 948.

[101] Forman, J. C., Moura, S. J., Stein, J. L., and Fathy, H. K., "Optimal Experimental Design for Modeling Battery Degradation," *2012 ASME Dynamic Systems and Control Conference; Ft. Lauderdale, FL*, 2008.

[102] Lawder, M. T., Northrop, P. W. C., and Subramanian, V. R., "Model-Based SEI Layer Growth and Capacity Fade Analysis for EV and PHEV Batteries and Drive Cycles," *Journal of The Electrochemical Society*, Vol. 161, No. 14, 2014, pp. A2099–A2108.

[103] Kim, Y., Mohan, S., Samad, N., Siegel, J., and Stefanopoulou, A., "Optimal power management for a series hybrid electric vehicle cognizant of battery mechanical effects," *American Control Conference (ACC), 2014*, June 2014, pp. 3832–3837.

[104] Ahmed, R., Gazzarri, J., Onori, S., Habibi, S., Jackey, R., Rzemien, K., Tjong, J., and LeSage, J., "Model-Based Parameter Identification of Healthy and Aged Li-ion Batteries for Electric Vehicle Applications," *SAE International Journal of Alternative Powertrains*, Vol. 4, No. 2, apr 2015.

[105] Lin, X., Stefanopoulou, A., Perez, H., Siegel, J., Li, Y., and Anderson, R., "Quadruple adaptive observer of the core temperature in cylindrical Li-ion batteries and their health monitoring," *American Control Conference (ACC), 2012*, June 2012, pp. 578–583.

[106] Troltzsch, U., Kanoun, O., and Trankler, H.-R., "Characterizing aging effects of lithium ion batteries by impedance spectroscopy," *Electrochimica Acta*, Vol. 51, No. 89, 2006, pp. 1664 – 1672, Electrochemical Impedance SpectroscopySelection of papers from the 6th International Symposium (EIS 2004) 16-21 May 2004, Cocoa Beach, FL, {USA}.

[107] Remmlinger, J., Buchholz, M., Meiler, M., Bernreuter, P., and Dietmayer, K., "State-of-health monitoring of lithium-ion batteries in electric vehicles by on-board internal resistance estimation," *Journal of Power Sources*, Vol. 196, No. 12, 2011, pp. 5357 – 5363.

[108] Weng, C., Sun, J., and Peng, H., "A unified open-circuit-voltage model of lithium-ion batteries for state-of-charge estimation and state-of-health monitoring," *Journal of Power Sources*, Vol. 258, 2014, pp. 228 – 237.

[109] Han, X., Ouyang, M., Lu, L., Li, J., Zheng, Y., and Li, Z., "A comparative study of commercial lithium ion battery cycle life in electrical vehicle: Aging mechanism identification," *Journal of Power Sources*, Vol. 251, 2014, pp. 38 – 54.

[110] Deshpande, R., Verbrugge, M., Cheng, Y.-T., Wang, J., and Liu, P., "Battery Cycle Life Prediction with Coupled Chemical Degradation and Fatigue Mechanics," *Journal of The Electrochemical Society*, Vol. 159, No. 10, 2012, pp. A1730–A1738.

[111] Dubarry, M., Svoboda, V., Hwu, R., and Yann Liaw, B., "Incremental Capacity Analysis and Close-to-Equilibrium OCV Measurements to Quantify Capacity Fade in Commercial Rechargeable Lithium Batteries," *Electrochemical and Solid-State Letters*, Vol. 9, No. 10, 2006, pp. A454–A457.

[112] Schiffer, Z. J., Cannarella, J., and Arnold, C. B., "Strain Derivatives for Practical Charge Rate Characterization of Lithium Ion Electrodes," *Journal of The Electrochemical Society*, Vol. 163, No. 3, 2016, pp. A427–A433.

[113] Oh, K.-Y., Siegel, J. B., Secondo, L., Kim, S. U., Samad, N. A., Qin, J., Anderson, D., Garikipati, K., Knobloch, A., Epureanu, B. I., Monroe, C. W., and Stefanopoulou, A., "Rate dependence of swelling in lithium-ion cells," *Journal of Power Sources*, Vol. 267, 2014, pp. 197 – 202.

[114] Oh, K.-Y. and Epureanu, B. I., "A novel thermal swelling model for a rechargeable lithium-ion battery cell," *Journal of Power Sources*, Vol. 303, 2016, pp. 86 – 96.

[115] Zhang, J., Lu, B., Song, Y., and Ji, X., "Diffusion induced stress in layered Li-ion battery electrode plates," *Journal of Power Sources*, Vol. 209, 2012, pp. 220 – 227.

[116] Forman, J. C., Moura, S. J., Stein, J. L., and Fathy, H. K., "Optimal Experimental Design for Modeling Battery Degradation," ASME International, oct 2012.

[117] Cannarella, J. and Arnold, C. B., "Stress evolution and capacity fade in constrained lithium-ion pouch cells," *Journal of Power Sources*, Vol. 245, 2014, pp. 745 – 751.

[118] Dubarry, M., Liaw, B. Y., Chen, M.-S., Chyan, S.-S., Han, K.-C., Sie, W.-T., and Wu, S.-H., "Identifying battery aging mechanisms in large format Li ion cells," *Journal of Power Sources*, Vol. 196, No. 7, 2011, pp. 3420 – 3425.

[119] Savitzky, A. and Golay, M. J. E., "Smoothing and Differentiation of Data by Simplified Least Squares Procedures." *Analytical Chemistry*, Vol. 36, No. 8, 1964, pp. 1627–1639.

[120] Lin, X., Stefanopoulou, A. G., Siegel, J. B., and Mohan, S., "Temperature Estimation in a Battery String Under Frugal Sensor Allocation," ASME International, oct 2014.

[121] Oh, K.-Y., Epureanu, B. I., Siegel, J. B., and Stefanopoulou, A. G., "Phenomenological force and swelling models for rechargeable lithium-ion battery cells," *Journal of Power Sources*, Vol. 310, 2016, pp. 118 – 129.

[122] Oh, K.-Y., Samad, N. A., Kim, Y., Siegel, J. B., Stefanopoulou, A. G., and Epureanu, B. I., "A Novel Phenomenological Multi-physics Model of Li-ion Battery Cells," to be submitted to Journal of Power Sources, 2016.